Air Force Institute of Technology
AFIT Scholar

Theses and Dissertations

Student Graduate Works

3-14-2014

Optimization of Graphene Sensors to Detect Biological Warfare Agents

Matthew J. Quinton

Follow this and additional works at: https://scholar.afit.edu/etd

Recommended Citation

Quinton, Matthew J., "Optimization of Graphene Sensors to Detect Biological Warfare Agents" (2014). *Theses and Dissertations*. 656.
https://scholar.afit.edu/etd/656

OPTIMIZATION OF GRAPHENE BIOSENSORS TO DETECT BIOLOGICAL WARFARE AGENTS

THESIS
MARCH 2014

Matthew J. Quinton, Major, USAF

AFIT-ENP-14-M-42

DEPARTMENT OF THE AIR FORCE
AIR UNIVERSITY

AIR FORCE INSTITUTE OF TECHNOLOGY

Wright-Patterson Air Force Base, Ohio

AFIT-ENP-14-M-42

OPTIMIZATION OF GRAPHENE BIOSENSORS TO DETECT BIOLOGICAL
WARFARE AGENTS

THESIS

Presented to the Faculty

Department of Engineering Physics

Graduate School of Engineering and Management

Air Force Institute of Technology

Air University

Air Education and Training Command

In Partial Fulfillment of the Requirements for the

Degree of Master of Science

Matthew J. Quinton, BS

Major, USAF

March 2014

OPTIMIZATION OF GRAPHENE BIOSENSORS TO DETECT BIOLOGICAL WARFARE AGENTS

Matthew J. Quinton, BS, MS

Major, USAF

Approved:

//Signed//_____   3/14/2014
Douglas Lewis, LTC, U.S. Army, (Chairman)   Date

//Signed//_____   3/14/2014
Larry Burggraf, PhD (Member)   Date

//Signed//_____   3/14/2014
Yun Xing, PhD (Member)   Date

//Signed//_____   3/14/2014
Rajesh Naik, PhD (Member)   Date

//Signed//_____   3/14/2014
Steve Kim, PhD (Member)   Date

AFIT-ENP-14-M-42

Abstract

The Defense Threat Reduction Agency and the Air Force Office of Scientific Research require sensors to detect biological agents better, faster, and cheaper. This research explores the use of graphene functionalized with single strand deoxyribonucleic acid (ssDNA) aptamers as a detection method for the Sterne strain of *Bacillus anthracis*. This research is interesting because of the unique electrical and chemical binding properties of graphene and its interaction with ssDNA and DNA. The interactions of graphene functionalized with ssDNA in response to *B. anthracis* spores, non-complimentary and complimentary DNA were explored in static and dynamic aqueous environments with indirect complimentary binding confirmation via Raman spectroscopy and atomic force microscopy. The results suggest aptamer functionalized graphene can be used to detect *B. anthracis* spores, non-complimentary and complimentary DNA sequences.

Acknowledgements

I am extremely grateful for the patience and persistence afforded to me by Lt Col Douglas Lewis, Dr. Larry Burggraf and Dr. Yun Xing. They possess a truly incredible mastery of the subject material, and their guidance was integral to the completion of this initially overwhelming project. They excel as scientists, mentors, and warriors and I am truly humbled by their diligence and work ethic.

I am also deeply indebted to Dr. Rajesh Naik, Dr. Steven Kim, Ms. Yen Ngo, Mr. Gerry Landis, Dr. Christina Harsch, Dr. Carrie Bartsch, Dr. Kristi Singh, Dr. Daylond Hooper, Dr. Larry Brott, Ms. Sharon Jones, Dr. Megan Pike and the AFRL Materials Nanotechnology Branch. The depth and breadth of their practical knowledge on this subject matter is incredible, and their support and contributions to this project were substantial. They shoulder an incredible load as the Air Force moves into the 22nd century, and I am very thankful they were willing to let me be a part of their brilliance during these interesting times.

I must also express my appreciation to Major Zens, Lt Col Radsick, Dr. Palazatto and all the people who support the Material Science program within ENP and ENY.

I would also like to thank the Chosen One, you know who you are.

<div align="right">Matthew J. Quinton</div>

Table of Contents

List of Figures

List of Tables

OPTIMIZATION OF GRAPHENE BIOSENSORS TO DETECT BIOLOGICAL

WARFARE AGENTS

I.   Introduction

1.1   Motivation

The Biowatch system, the premiere U.S. biodefense system, needs 12 to 36 hours

to determine if a pathogen is present. This delay coupled with a total system cost

estimate of $5.8 billion dollars has many in government seeking other ways to detect

biological agents [1]. The Defense Threat Reduction Agency recently put out a call to

industry to determine other ways to develop biosensors that can detect biological

weapons cheaper, faster and more accurately than the current systems [2]. Recent

advances in nanotechnology, micro-electromechanical systems, and the proliferation of

genetic data and laboratory techniques and equipment via the internet has moved

biological research and development projects from large, secure government institutions

to anyone willing to pursue biological weapons development. As a dated example, the

terrorist organization Aum Shinrikyo used *Bacillus anthracis (B. anthracis)* spores

against their Japanese countrymen in 1993 [3]. Their organization consisted of academic

research scientists, wealthy industrialists, and government members that helped the group

gain access to *B. anthracis* stockpiles. This knowledge and access to previously

unavailable materials allowed them to grow and use *B. anthracis* on an innocent

population. Their leaders may have picked a different path had they known the agent was

a vaccinated strain [4].

This event occurred before the Internet was available to the average person. Anyone with internet access can find sections of the *B. anthracis* genome on the National Institutes of Health website [5], low cost polymerase chain reaction units needed to isolate and amplify genetic code for $599.00 [6] and the online resources to develop and purchase primers to isolate genetic code for $50.00 [7].

This turn of events has many U.S. Government officials worried, especially after the anthrax attacks in 2001. The Center for Disease Control estimates the anthrax cleanup cost at more than $320M [8]. Robinson, Heden and Schreeb calculated and compared the cost of civilian casualties per square kilometer at $2000.00/$km^2$ with conventional weapons, $800.00/$km^2$ with nuclear weapons, $600.00/$km^2$ with nerve gas and $1.00/$km^2$ with biological weapons[9]. This estimate shows how much capital is required to damage a populated area. The obvious conclusion is that a low cost, limited investment in bioweapons could do massive amounts of economic damage.

People affected by a biological attack usually are unaware until they express symptoms associated with the biological agent. For example, *B. anthracis* causes anthrax in humans and it takes three to seven days to express symptoms after agent exposure. The initial symptoms mimic the early stages of influenza and could confuse medical personnel. This delay puts the exposed victim at risk and gives the perpetrators time to escape and time to decide whether to claim responsibility for the attack. The Stimson Center for International Progress has studied globalization and terrorism and note that bioweapons could be developed in a Pakistani hut just as easily as in a fully equipped

2

Western laboratory [10]. The previously mentioned tools make it much easier to design new biological weapons for use against civilians and government personnel.

To counter a biological attack, it is necessary to identify the biological agent as quickly and as accurately as possible and send out a warning signal once positive identification is available. There are a number of biological detectors available to identify agents but they all suffer from a number of issues to varying degrees. The first issue is the time required to detect the agent in question and the second issue is the inability to discriminate between non-pathogenic and pathogenic organisms in the field [11]. Ivnitski, Morrison, and O'Neil are in agreement with DTRA and DARPA as they note shortcomings in demonstrated sensor sensitivity in the laboratory versus the field, transportation/weight related issues, specialized operator training, and the increase in sensor operations costs and maintenance costs. Total program discussions illustrate the reality that new technologies come with additional costs and issues that are not considered in the laboratory. Sensor sensitivity, weight, and operator training were considered during the literature review and were applied to the choice of sensor research.

To address some of these issues, a novel graphene biosensor approach was constructed and tested. This unit was label-free aptamer biosensors with single stranded DeoxyriboNucleic Acid (ssDNA) as the aptamer attached to a graphene base. The aptamer (ssDNA) and graphene act as the sensor element. The ssDNA recognizes and binds to complimentary DNA (cDNA) strands or spores based on their structural configuration and that conformational binding event would be detected by a change in the

3

graphene resistance. This approach attempts to address the DTRA requirements for

quick, accurate, and low-cost sensors.

1.2   Research Topic

Manoor showed it is possible to detect Gram-positive and Gram-negative bacteria

via antimicrobial peptides bound to a graphene-gold circuit in approximately 200 seconds

[12], while Mohanty and Berry showed it is possible to detect single microorganisms

using chemically modified graphene [13]. The time limit and protocols used to detect the

separate strains of bacteria inspired the study and development of a label-free graphene

biosensor functionalized with ssDNA specific capture elements. It has been

experimentally shown that ssDNA attaches to graphene due to π-π bonds and detaches

from graphene in the presence of cDNA[14]. We hypothesized that this property could

be modified with a chemical linker to secure it to the sensor base to create a reusable

sensor unit. Our unique approach uses 1-PyreneButanoic Acid, Succinimydal Ester

(PBASE) molecules [15] to chemically link modified ssDNA capture elements [16] to a

graphene base and use it as a sensor. The ssDNA was selected because it was designed to

detect the DNA of spores from the *B. anthracis* Sterne strain [16]. The chemical linker,

PBASE, was selected due to its room temperature (303K ~ 70F) graphene binding ability.

It provides a succinimidyl ester as an anchor point for amine modified ssDNA. Graphene

was picked due to its high electrical conductivity (100,00cm/Vs) and functionalization

properties [17]. Figure 1 conceptually represents a graphene-field effect transistor

(GFET). Where the graphene-PBASE-ssDNA sensor is built on top of a silicon wafer in

a small rectangular area bordered on two sides by gold metallized probe pads sputtered in

a T base to base configuration with the graphene functionalized rectangular area

completing the circuit.
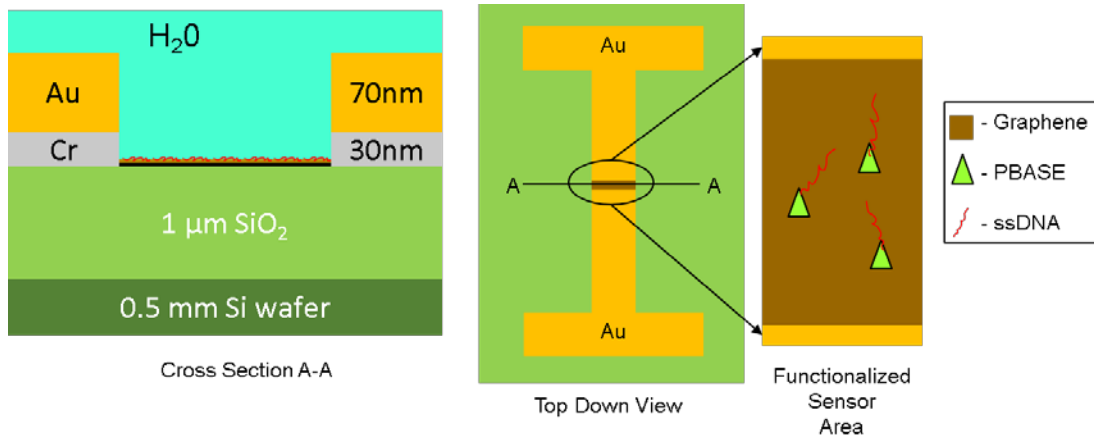
Figure 1: Biosensor overview. Cross section shows the graphene-PBASE-ssDNA sensor area with gold and chromium contacts on the sides. The top down view shows the overall sensor with dimensions 29mm by 22.5mm. The functionalized sensor area is on average 0.6 mm by 0.5mm. The number of PBASE molecules and ssDNA molecules has been reduced for conceptual clarity.

The graphene is isolated from the circuit via thermally grown silicon dioxide. This

setup helps prevent stray charges from interfering with the electrical current across the

graphene. The design allows for easy measurements for static tests and dynamic

microfluidic tests as target DNA sequences bind to the functionalized ssDNA. This setup

produces a useful field effect transistor that makes it possible to detect changes in the

conductivity of graphene via the conformational binding events between ssDNA and

cDNA and mimics a similar configurations used in some hybrid graphene sensors [18]

and other GFET sensors [19], [20].

1.3 Research Objective

This study seeks to characterize detected changes in resistance of a GFET due to conformational binding events between a *B. anthracis* derived aptamer and its complimentary sequence.

This is accomplished with a graphene surface that has been functionalized with different aptamer sequences. The first sensor uses a 22 base pair aptamer functionalized on the graphene surface to show initial proof of concept. The second sensor uses a 77 base pair *B. anthracis* capture aptamer functionalized on the graphene surface to demonstrate spore capture capability[16]. The sensor response and sensitivity was checked via exposure to the following targets in deionized water: a 22 base pair complimentary sequence, a 39 base pair complimentary sequence, a 77 base pair complimentary sequence, a 18 base pair degenerate sequence, and *B. anthracis* spores. The targets were introduced to the sensor under dynamic flow and static fluid conditions to determine the effect on signal detection and elucidate that knowledge.

1.4 Document Structure

This document is organized as follows: Chapter II reviews biological detection and label free bio-FET graphene sensor systems, followed by the structural properties of *B. anthracis*, ssDNA and cDNA aptamers, the PBASE attachment molecule, attachment fluorophores, graphene, the silicon (Si) substrate, biosensor design, construction and usage. Chapter III explores the methodology used to analyze the aptamers and understand the sensor response. Chapter IV presents the results and analysis of the data. Chapter V provides a summary of conclusions and future research opportunities.

Supplemental materials include Appendix A (Equipment and Settings), Appendix B (Circuit Recipes) and the references section.

II. Literature Review

This chapter contains seven sections that provide background and theoretical information relevant to this study. The first section explores biological detection and focuses on label-free graphene based DNA biosensors with single strand and double strand DNA detection elements. The second section introduces the *B. anthracis* lifecycle and its cellular structure. The third section focuses on ssDNA aptamers, PBASE and the Texas-Red fluorophore used to detect cDNA with attention given to their structures and chemical binding capabilities. The fourth section introduces the structure, electrical and chemical properties of graphene. The fifth section introduces the structure and electrical properties of the silicon oxide (SiO_2) wafer platform used to attach and test the graphene-PBASE-ssDNA sensor. The sixth section introduces the biosensor design used in this research.

2.1   Biological Detection

Biological detection in the United States military has been treated like chemical detection for the last 100 years. This is unfortunate, because biological weapons have different characteristics that affect detection. Chemical weapons have definite signatures and are relatively stable while deployed to the target. The ability of chemical weapons to effect targets decreases after the initial deployment due to factors such as sun and rain exposure [21].

Biological weapons are living organisms with the ability to reproduce and adapt to new situations. Single celled organisms, like *B. anthracis*, reproduce anywhere from 8 minutes to 40 minutes per generation. The pathogenic variants, Vollum and Pasteur, reproduce 2 to 3 times as fast as nonpathogenic variants such as the Sterne strain under pH conditions from 5.5 to 6.5 [22]. The reproduction rate allows for polymorphisms (changes) in the population that result in genetic variations that could make them difficult to track. As an example, *B. anthracis* and *B. cereus* are considered homologous organisms, in that they share a common ancestor and common genes. This makes distinguishing them difficult as strains of *B. cereus* have been found in the Congo that have the same pXO1 and pXO2 plasmid strains found in *B. anthracis*. *B. cereus* isn't normally considered lethal but these particular strains have managed to infect and kill members of the great ape population in Cameroon [23]. To make matters even more interesting, there have been over 1200 identified *B. anthracis* strains to date [24].

Once biological agents are released into the environment the chance of genetic mutation increases based on the regular bacterial exchange of genetic material via pili (tubular growths that allow bacteria to exchange genetic material). This exchange has the potential to modify the infectivity, virulence, and pathogenicity of the microorganisms involved (see the *B. cereus* discussion above). These mutation events are based on multiple probabilities whose elucidation is well beyond the scope of this paper. The important point is that it could happen and the question is how to detect it. This leads to the types of detection schemes that are recognized by the defense and medical communities.

There are two types of recognized detection categories, "detect to protect" and "detect to treat". The "detect to protect" category means a warning is given in time for personnel to don the appropriate protective gear. The main purpose of the "detect to treat" sensor is to identify the agent for medical personnel to provide countermeasures prior to the development of symptoms. The biological detectors that have been developed to "detect to treat" and "detect to protect" against biological agents have a number of shortcomings due to technological immaturity and a mischaracterization of behavior associated with living organisms versus non-living chemicals. Unfortunately, biological agents have a number of attributes that make biological detection difficult.

The first attribute is the large number of environmental biological signals (bio-noise) from local microorganisms that confuse detector readings. The inability to discern the signal from the noise either, masks the agent signature and causes the sensor to report a false negative for the event in question or causes the sensor to transduce and send a false positive signal [25]. Both situations are bad and can task emergency management personnel needlessly.

The second attribute deals with the inability to distinguish between pathogenic and nonpathogenic microorganisms [26]. The regular exchange and incorporation of foreign genetic material by bacteria for food, genetic repair, and genetic diversity further confound the distinguishability problem [27].

The third attribute is the infection time, which depends on the strength of the host immune system and the type of organism. If the host has a weak immune system due to age or poor health, the infection may become apparent very quickly. If the infection

succeeds, the symptoms usually show up three to seven days for most biological agents. Most initial human symptoms mimic the flu and become more pronounced and deadly as time passes [28]. The misunderstanding of these three attributes has caused the US Government to spend over $3 billion dollars in an attempt to address the prevention of a biological attack.

To address detection issues, several notable studies have been conducted: Defense Advanced Research Projects Agency (DARPA) funded the 2010 Chemical and Biological Sensor Standards Study. Its purpose was to review the available biological and chemical sensors and determine quantifiable standards and figures of merit that could be used to measure and compare those systems[25]. This effort also helped the US Government by filling a critical hole in the design and evaluation of sensors. The study identified sensitivity, probability of detection, false positive rate, and response time as figures of merit that need to be reported at all stages of sensor development to reduce the ambiguity associated with the evaluation of biosensors.

The 2011 Chemical, Biological, Radiological Technology Survey, sponsored by the Joint Program Executive Office, Chemical Biological Medical Systems and DTRA, evaluated 282 and selected the top 60 biological weapon detectors available for purchase by the Department of Defense (DoD). The systems were scored against four scenarios: field use; mobile or field laboratory; diagnostic laboratory or point of care use; and high sensitivity, high throughput analytical laboratory. They were scored at sublevels focused on biological agent specific systems; radiological agent specific systems; chemical agent specific systems; and multifunctional systems [29].

Biological detection has drawn the notice of laboratory clinicians concerned about their laboratory capabilities to determine a biothreat and the comparability of biosensor results. Justino, Rocha-Santos and Duarte explored sensor system figures of merit and identified calibration sensitivity, selectivity, limits of detection, repeatability and reproducibility as critical figures of merit that need to be reported for clinical biosensors developed in laboratory or field settings. They noted that there were no comparable results between sensor systems that were developed in different laboratories [30].

2.1.1 Technology Review

There are a number of technologies and techniques designed to detect and characterize single celled organisms. Speigelman, Whissell and Greer review PCR units, biochemical methods, DNA microarrays, and oligonucleotide probes [31].

PCR units are the gold standard of microbiological identification and can generate millions of DNA strands for analysis from a single strand of subject DNA. PCR units can give false representations of the microbial environment via amplification of the wrong DNA through contamination of the sample or through cross reactivity with environmental unknowns [32].

DNA re-association kinetics and %G&C fractionation are biochemical methods that provide information on large bacteria populations. Unfortunately, DNA re-association kinetics depend on the size of the population and can take weeks to complete. Whereas %G&C fractionation cannot discriminate below the genus level as it relies on the percent composition of G&C and does not provide definitive identification of the genus involved.

DNA microarrays are large oligonucleotide arrays hybridized with fluorophores. The operational principles are deceptively simple. A low powered laser is emitted in their direction. The fluorophores excite and emit a detectable wavelength. This method can help determine which bacterial samples respond to the oligonucleotide. The technology may be susceptible to oligonucleotide array cross functionalization which could indicate a higher population characteristic than are present. Oligonucleotide probes can be designed to specifically attach to a particular bacteria taxonomic group. The specificity allows researchers to target and determine the frequency of particular bacteria within the bacterial community. The specificity can be blessing as well as a curse because it may miss certain bacteria that are part of the taxonomic group but do not have those particular proteins expressed on their surface [31].

Oligonucleotide probes can be used in a label or label-free fashion. A "label" oligonucleotide is designed to attach itself to the bacteria of interest. It usually has a signaling mechanism (radioactive phosphorus, fluorophore, quantum dot) integrated into it and that requires electromagnetic interrogation/detection from a macroscopic device or person. For example, labeled oligonucleotides are used in enzyme-linked immunoassays, which require some sort of interrogator and detector. A "label-free" oligonucleotide is one that does not need to be interrogated by an outside source but is usually monitored for a configuration change as the bacteria of interest are captured due to the complimentary binding of the oligonucleotide to the bacterial surface.

2.1.2   Graphene Sensor Review

Graphene sensors are only limited by the imagination of the designer. Saltzgaber et al., used graphene grown on Cu foil via the chemical vapor deposition (CVD) method. They then spun a polymethyl methacrylate (PMMA) onto the graphene/Cu square to get a PMMA/graphene/Cu transfer unit. This unit was placed into copper etchant to dissolve the copper and leave a PMMA/graphene layer for transfer to a 500nm SiO_2 layer on a circuit. The PMMA/graphene/SiO_2/Si circuit was dried for 4 hours at 30 C and then open air heated for 4 hours at 350 °C to remove the PMMA. The graphene was patterned in 3.0 µm by 10.0 µm sections using photolithography and a dedicated plasma etcher [19]. The next step fabricated 1.5nm Cr and 30nm Au electrodes onto the circuit leaving a 3.0 µm by 3.0 µm graphene area exposed. This section was cleaned in an Ar/H_2 environment to ensure a clean surface. Then the graphene surface was functionalized with PBASE and a thrombin specific DNA aptamer (15 base pairs) to detect thrombin in real time [19]. The analyte was delivered at 25 µL/min in a 5.0 mM MES buffer They demonstrated binding reversibility and reported device stability over the course of one week [19]. Ohno et al, had a similar setup that used kish graphite exfoliated onto a 280 nm thick SiO_2 layer on top of a p+-Si substrate with PBASE functionalization and aptamers to detect immunoglobin E[33].

According to Kuila, there are at least 18 different graphene based sensor variations that use detection elements such as glucose, cholesterol, NADH, hydrogen peroxide, nitrites, nitrous oxide and aptamers (such as ssDNA). Six of these units use graphene, epitaxial graphene and graphite oxide as bases to detect DNA via changes in

fluorescence intensity or electrical current [34]. The sensor materials and detection limits

listed in Table 1 illustrate the types of processed graphene that can be used to inform the

detector elements and the limits of detection. The majority of the sensors are based on

fluorescent detection, which requires an illumination source, a foreknowledge of the

ssDNA sequence and a fluorescent molecule attached to the ssDNA. The size and

position of the fluorophore on the ssDNA can be an issue and should be taken into

account as the addition of extra bond sites brought by the fluorophore can cause

unanticipated attachments with cDNA and the environment.

The other graphene sensors rely on drain current and gate voltage changes to

detect changes on the graphene via conformational binding events between the aptamer

and target of choice. This is accomplished by the functionalization of the graphene

surface with different molecules such as EDTA, amines, PBASE, etc.

Table 1: Graphene Sensor Characteristics.

Sensor Material	Sensor Response	Detected Element	Limit of Detection	Source
Graphene Oxide	Fluorescence	DNA	103 pf μm	Kuila [34]
Exfoliated Graphene	Electrical Current	DNA	1 μM	Kuila [34]
Graphene Oxide	Fluorescence	DNA	200 nM	Kuila [34]
Graphene Oxide	Fluorescence	DNA	2 nM	Kuila [34]
Chemical Vapor Deposition Graphene	Current/Gate Voltage	ssDNA	10 nM	Pumera [35]
Reduced Graphene Oxide	Current/Gate Voltage	ssDNA	10 nM	Pumera [35]
Aminated Graphene Oxide	Current/Gate Voltage	ssDNA	1 *B. Cereus*	Mohanty and Berry [13]

The table shows the detection limit for CVD graphene 10 nM using a ssDNA

aptamer. This detection limit serves as a reference point for sensor development as

discussed in Chapter 2.6. Chen, et al. reported label-free sensing with a 12 mer (12 base

pair) DNA sequence at pico-molarity concentrations using gated field effect CVD

graphene transistor [36].

2.2   Bacillus Anthracis

B. anthracis is a bacterial species that has infected humans since man

domesticated herbivores with one of the earliest known infections being the Fifth Plague

in Egypt [37]. Its presence on every continent [38], its spore-forming ability for survival

in harsh environments and its lethality, once introduced into the mammalian host and left

untreated, make it one of the most feared potential biological agents on Earth. The CDC

classifies it as a Category A agent due to the potential to become a national security

risk[39].

2.2.1 Lifecycle

B. anthracis is a zoonotic organism found in sheep, cows, goats, pigs and other

domestic herbivores throughout the world. When exposed to oxygen or adverse

conditions it forms a hard shell and becomes dormant. The shell, called an endosporium

or endospore, allows it to lie dormant until ingestion by domestic livestock, or inhalation

by humans. Once in the anaerobic environment of a mammalian body (humans, cows,

etc), *B. anthracis* propagates and releases protective antigens, lethal and edema factor

toxins that cause anthrax [40]. Moayeri provides a detailed review of lethal and edema

toxins [41]. The toxins destroy the cell walls and leak into the blood stream causing

15

system wide septicemia (blood poisoning) that kills the host. *B. anthracis* generates an endospore when it detects high levels of oxygen in the decomposed body [21]. The endosporium is a hard shell that protects *B. anthracis* DNA via a dehydration mechanism that reduces the DNA volume by up to 20% [42], [43]. This chemical change allows the endospore to remain inactive for more than 40 years [44]. The hardiness of this agent makes it the choice bioweapon for poor countries and terrorist organizations.

B. anthracis invades the human body via three routes; cutaneous, gastrointestinal and inhalation[45]. Cutaneous anthrax results when *B. anthracis* enters through a cut and festers until it destroys enough tissue to get into the blood stream. This form can cause septicemia with a 20% mortality rate for those untreated and a 1% mortality rate for those treated[28]. Gastrointestinal anthrax results when *B. anthracis* enters the body by eating infected meat and has a mortality rate as high as 50%[28]. Inhalation anthrax occurs when spores smaller than 3.0 µm in diameter are inhaled. It has a 45% mortality rate when treated with antibiotics. Untreated, it has a mortality rate between 80% and 100%. The 1979 Sverdlovsk Incident in Russia resulted in civilians infected via inhalation that resulted in 85% casualties[28]. The onset of inhalation anthrax is between one and six days. The initial symptoms mimic influenza and may cause medical staff to misdiagnose the patient. Two to four days later more severe signs occur with general malaise, exhaustion, tachycardia, cyanosis, and lethal shock followed by death[28].

2.2.2 Structure

B. anthracis is a Gram-positive, rod-shaped bacterium, approximately 1 µm in diameter and 3-5 µm in length. It has a 25-50 nm thick peptidoglycan shell composed of

16

murein, teichoic and lipoteichoic acid that surround the plasma membrane [46]. The surface sites on *B. anthracis* spores have unique molecular signatures that can be exploited and provide a way to capture it via an aptamer [16].

2.3   Aptamers, Chemical Linkers, and Fluorophores

Aptamers are sequences of oligonucleotides, usually less than 50 base pairs in length, that have high affinity and selectivity toward complimentary DNA sequences or proteins based on their structural composition [47]. The aptamer sequence can target complimentary DNA. Capture aptamers can be used to identify bacteria by binding to surface proteins or carbohydrates on the cell membrane. They can be built via the systematic evolution of ligands by exponential enrichment (SELEX) process one nucleotide sequence at a time [48]. Basic aptamer sequences can be generated with special modifications, such as aminated nucleobase sequences and fluorophores, for the construction of biosensors.

Aptamers can be thought of as lock and key or hand in glove mechanisms that make them ideal biological sensors. If a surface molecule associated with the agent matches the aptamer structure, hydrogen, van der Waals, and Coulombic forces take over and cause the aptamer to bind to it. This binding event changes the aptamer structure and can serve as a basis for detection.

2.3.1   Aptamers

Aptamers were discovered as a form of ribonucleic acid (RNA) by the Szostak and Goldman Laboratories in the early 1990s [49]. RNA is similar to DNA in base pair construction except that the uracil nucleobase is switched out for the thymine nucleobase.

Aptamers have many different definitions in academia. The term aptamer in this paper refers to single strand DNA.

A single nucleotide unit of DNA is composed of a phosphate, a deoxyribose (pentose sugar) and a nucleoside base. The phosphate backbone has covalent bonds and consists of phosphodiester units attached to the 5' and 3' (read 5 prime and 3 prime) carbon hydroxyl groups of the deoxyribose sugar unit. The nucleoside base consists of one of four units, adenine (A), thymine (T), cytosine (C) or guanine (G) attached by a nitrogen molecule to the 1' carbon on the deoxyribose sugar. The nucleoside base, the dexyribose sugar, and the phosphodiester backbone result in a nucleotide unit that interacts with other complimentary nucleotide units via hydrogen bonds. Complimentary interactions occur between the double-ring pyramidine nucleoside bases (A and G) and the single ring pyrimidine nucleoside bases (T and C). These interactions are present in Watson-Crick pairs and that compose the structural basis for the physical properties of DNA in the majority of single cell and multicellular organisms.

Watson-Crick pairs form when the two hydrogen bonds on adenine and thymine (A-T) are opposite each other and three hydrogen bonds on cytosine and guanine (C-G) are opposite each other[50]. The bond pairs form naturally in a 5' to 3' direction to allow enzymes easier access to the ATP used in replication. DNA can be considered a negatively charged molecule due to the oxygen molecules attached to the phosphate backbone. The structural differences between the pyramidine-purine (AT/CG) interactions and the hydrogen bonds can generate secondary, tertiary, and quaternary

18

DNA structures [51] that form A, B and Z DNA whose structural characteristics are in

Table 2.

Table 2: DNA Forms. Data from [47].

	A-Form	B-Form	Z-Form
Helical Sense	Right Handed	Right Handed	Left Handed
Diameter $(x10^{-10}$ m)	26	20	18
Base pairs per helical turn	11	10.5	12
Helix rise per base pair $(x10^{-10}$ m)	2.6	3.4	3.7
Base tilt to normal to the helix axis (°)	20	6	7

Small molecule DNA recognition has been used to exploit the minor and major

grooves of A, B and Z DNA structures via intercalation (the ability of a small molecule

or protein to fit into the major groove of the DNA) [47]. Extensive research has shown

ssDNA can recognize double stranded DNA to form a triplex DNA structure at room

temperatures at various pH levels [50]. Triplex stability increases as a function of base

pair length and sequence repeats [50] .

Wu reported ssDNA binds to graphene surfaces via π-π bonds and unbinds from

the graphene surface when a complimentary DNA sequence is recognized [52]. This is

important because an electrical signal can be used to interrogate the ssDNA aptamer

while it is bound to the graphene surface. Contact with a cDNA aptamer will cause the

ssDNA aptamer to bind to the cDNA and change the surface electrical properties of the

graphene resulting in a trigger event [19], [20].

The electrical conductivity of DNA has been a contentious issue within the

scientific community. A review by Endres shows the conflicting nature of DNA

conducting abilities as it can act as an insulator, a wide-bandgap semiconductor, an

ohmic conductor and a metal at room temperature [53] and in some cases, it acts like a p-type semiconductor [54].

The knowledge of the conductivity state of the ssDNA aptamer on graphene can be measured before the sensor interacts with target DNA aptamers. This can form the basis for a sensor element. The interaction with complimentary target DNA and noncomplimentary target DNA can help determine how the ssDNA sensor element should react when it interfaces with biological agents.

The *B. anthracis* aptamer used in this research was derived from Fan's work on DNA capture elements used to detect *Bacillus anthracis* and *Francisella tularensis* [16]. The original 80 base pair sequence was shortened by 3 base pairs and modified on the 5' and 3' ends to support fluorophore and amine additions for test and attachment purposes. The *B. anthracis* aptamer, control aptamer and target aptamer sequences are listed in Table 3. The red, italicized letters indicate the aptamer recognition sequence associated with the Sterne strain of *B. anthracis.* The black letters indicate capture sequence elements added to the original aptamer recognition sequences to help bind to cDNA in a fluid medium. The aminated adenine on the 5' end of the ssDNA 22bp and the aminated guanine on the 3' end of the ssDNA 77bp represent amine modifications on the 6' carbon hydroxyl of the adenine nucleobase and the 3' carbon hydroxyl of the guanine nucleobase respectively. These modifications allow the ssDNA to attach to the NHS (succinmidyl ester) on the end of the PBASE molecule at room temperature (303 K). The PBASE attachment binds the aminated portion of the aptamer to the graphene. The ssDNA binds to the graphene based on the π- π bonds as discussed earlier and waits until a cDNA

molecule is in range. When the ssDNA recognizes cDNA, the portion *that is not attached to the graphene via the PBASE molecule* unbinds from the graphene and binds to the cDNA. *If the ssDNA was not attached to the graphene, it would bind onto the cDNA and float off the sensor.* This event forces a conduction change on the graphene surface that produces a measureable electrical signal. The aptamers in Table 3 have unique characteristics that can influence the measureable electrical signal.

The cDNA 77bp and 39bp have Texas-Red fluorophores attached to the 5' carbon hydroxyl that allows for the detection of a conformational binding event. The fluorophores are of the same length order of magnitude as the DNA strands they functionalize.

The ssDNA22bp represents the control aptamer and was used to test the original concept. Part of the ssDNA22bp strand consists of a 10 base pair adenine sequence that may be able to form triple helix when brought in contact with enough other thymine nucleobases.

The cDNA22bp is one of the target aptamers to determine how well the ssDNA77bp and ssDNA22bp aptamers respond. The thiol modification on the 3' end of the cDNA22bp represent a sulfur modification on the 3' carbon of the thymine nucleobase that allows for the attachment of either gold or metal particle attachment. A thiol compound has an R-S-H structure, where the R is any group except H, S is sulfur and H is hydrogen [55]. Thiolates derive from thiol compounds in such a way that a metal atom replaces the hydrogen attached to the sulfur.

The 18bp degenerate DNA sequence is a random sequence used to determine the 22bp and 77bp aptamer response to random DNA chains.

Table 3: Aptamer Sequences.

Aptamer Sequences	
DNA Identifiers	Sequences with modifications (shown 5' to 3')
ssDNA (77bp)	ACCCCTGCATCCTTTGCTGGAGAGGAATGTATAAGGATGTTCCGGGCGTGTGGGTAAGTCAGTCTAGAGGGCCCCAG-NH$_2$
cDNA (77bp)	(Texas-Red)-TGGGGACGTAGGAAACGACCTCTCCTTACATATTCCTACAAGGCCCGCACACCCATTCAGTCAGATCTCCCGGGGTC
cDNA (39bp)	(Texas-Red)-TGGGGACGTAGGAAACGACCTCTCCTTACATATTCCTAC
ssDNA (22bp)	(5AmMC6)-AAAAAAAAAAGAGGGATTGTTA
cDNA (22bp)	TAACAATAATCCCTCAAAAAAAAAA-(3ThioMC3-D)
Dg_ssDNA(18bp)*	VAWRTCCATYTGCCARTT
* V = (A, C, or G); W = (A or T); R= (A or G); Y= (C or T) [47]	

The ssDNA77bp and cDNA77bp are the most likely to form secondary structures based on the manufacturer's statements and the OligoAnalyzer 3.1Toolkit at IDTDNA.com[56]. The OligoAnalyzer was used to notionally determine the binding characteristics that could be expected for the 77bp aptamer sequence. It is important to note that this sequence has been modeled using a 1.1nM concentration with a 1 mM Mg^{2+} (magnesium ion) salt concentration. Positive ions in solution tend to bond to the oxygen in the phosphodiester backbone and cause the DNA to "open" up or stay "open" at the right temperature.

The most probable 77bp aptamer molecular configuration had a Gibbs free energy of -6.4 kcal/mole whereas the next most likely configuration had a Gibbs free energy of -6.0 kcal/mole. Remember a negative Gibbs free energy indicates a spontaneous reaction,

while a positive Gibbs free energy indicates a non-spontaneous reaction. This means first structure was more likely to form under ambient conditions than the second structure. This is unfortunate because the second structure had larger linear recognition region between the 20 to 60 base pair sequence.

The ssDNA 22bp aptamer was put through a similar analysis with the OligoAnalyzer Toolkit. The most likely configuration for the 22bp aptamer would be a straight chain due to the melting or denaturing temperature of $T_m = -330$ °C and the Gibbs free energy being positive which requires energy to be put into the system to hold it at that particular configuration. The ssDNA22bp aptamer is likely to be in a chain-like configuration approximately 7 nm maximum length.

2.3.2   Chemical Linker - PBASE

The 1-{[4-(1-Pyrenyl)butanoyl]oxy}-2,5-pyrrolidinedione, or 1-pyrenebutanoic acid, succinimidyl ester (PBASE) serves as a noncovalent bridge between the graphene and the ssDNA. The aminated ssDNA attaches to the succinimidyl ester group (NC_4O_2) via an amine reaction at ambient temperature (303K) and pressure (0.987 atmosphere). The succinimidyl ester on the "tail" serves as the attachment point for aminated ssDNA ends, while the four benzene ring structures on the "bottom" of the PBASE molecule anchor to the CVD graphene. The PBASE chemical linker is added to the graphene in a N,N-dimethylformamide (DMF) solution to promote bonding characteristics associated with the π-π bonds. The PBASE disperses randomly on the graphene surface and orients itself appropriately. Visual representations of PBASE and DMF can be found at Chemspider.com under ID numbers: 115656 and 5993, respectively [57],[58].

23

2.3.3   Fluorophores

Fluorophores are molecular structures with special electronic orbital properties that absorb in ultraviolet light and emit visible light approximately 10^{-8} seconds after the absorption event [59]. Fluorophores can be attached to just about any aptamer that can be designed. However, the attachment chemistry and overall function of the fluorophore must be taken into account to determine the optimum functional environment for the fluorophore [60]. The DMF protocol used to attach the PBASE to the graphene was incompatible with many of the available fluorophores. Texas-Red was the only fluorophore that was soluble in DMF and was recommended for use with the PBASE modification to graphene due to the limited protrusions of sulfur and oxygen from the base [60]. Fluorophores can be matched with materials that quench emission until specific conditions are met. Graphene is a natural fluorophore quencher with the ability to quench 70% of a fluorescent signal within 10 nm of the graphene surface and 50% of a fluorescent signal within 24 nanometers of the graphene surface of a 6-carboxylfluorescein probe [61]. This evidence, while compelling for the 6-carboxylfluorescein, does not necessarily mean that the CVD graphene will quench the Texas-Red fluorophore. The fluorophore was a secondary check to determine if the 77bp target aptamers would bind to the ssDNA 77bp aptamer on the sensor surface. The 6-carboxylfluorescein excites at 492nm and emits at 517nm (greenish light) whereas Texas-Red excites at 583nm and emits at 603nm (red-orange). A visual representation of Texas-Red can be found at Chemspider.com under ID number: 398742 [62].

2.4   Graphene

Graphene per Kochman is "Exactly one layer of polycyclic aromatic, hydrocarbon network with all carbon atoms hexagonally arranged in a planar condensed ring system. It has a metallic character and consists solely of carbon and hydrogen" [63]. The definition of graphene is important as there are at least 21 different acronyms in the current literature that describe the same material [63]. Single-layer, clean, suspended graphene has a reported electron carrier mobility of 200,000 cm^2 $V^{-1}s^{-1}$ whereas kinked graphene has demonstrated an electron carrier mobility between 2000 to 15000 cm^2 $V^{-1}s^{-1}$ [64]. Compared to Au, Ag, and Cu, this makes graphene potentially one of the fastest, if not lightest conductors on Earth. Graphene also has a tendency to bond with other organic compounds due to the pericyclic bonds emanating perpendicularly from the hexagonal plane. The affinity for other organic molecules makes graphene a good point to start in the exploration of biological and biologically related systems.

2.4.1   Graphene Structure

Graphene consists of one layer of carbon bonded to carbon in a flat hexagonal arrangement with an accepted height of 0.34 nm [65]. The hexagonal carbon arrangement forces the carbon π bonds to equilibrate above and below the plane and create a pseudo-bandgap structure that allows the electrons to move at near relativistic speeds through the six distinct points where the k-space vectors touch. Kittel provides a good explanation of the solid state physics background needed to generate and really understand k-space vectors[66]. Suffice to say all the semiconductors used today have well defined band gaps that allow photons (light vibrations) and phonons (elastic

25

vibrations) to jump from the valence band to the conduction band. The conduction and valence bands are the result of the crystal structure and are usually well defined and smooth for three dimensional structures. Graphene's two dimensional in nature puts a different twist on the energy band structure forcing the valence and conduction bands down to 6 distinct points with the energy described by Equation 1 [65].

$$W_{2D}(k_x, k_y) = \pm\gamma_0 \left[1 + 4\cos\left(\frac{\sqrt{3}k_x a}{2}\right)\cos\left(\frac{\sqrt{3}k_y a}{2}\right) + 4\cos^2\left(\frac{\sqrt{3}k_y a}{2}\right) \right]^{\frac{1}{2}} \quad \text{(Eq. 1)}$$

Where: W = Energy (J)

γ_0 = the nearest neighbor overlap

a = the in plane lattice constant (nm)

k_x = wave vector x-direction (m^{-1})

k_y = wave vector y-direction (m^{-1})

The plus and minus signs represent the carbon-carbon double bonds, more commonly known as π bonds, in this case π and π*. The π bond represents the lowest unoccupied molecular orbital (LUMO) whereas the π* represents the highest unoccupied molecular orbital (HOMO). The LUMOs are where most of the bonding takes place as is a lower energy state. The HOMOs are where limited bonding takes place as it is a higher energy state and requires substantial energy to sustain. The HOMOs and LUMOs result in the corners of the two dimensional Brillioun zone that touch each other at T = 0 K and contribute to graphene functioning as a gapless semiconductor [65]. There are multiple books written on graphene properties and models for very tight tolerance GFETs [65],[67],[68]. For this research purpose, the interest in graphene is constrained to its

electron transport properties, ssDNA binding properties, and simple production. The CVD copper growth method was used to grow the graphene for transfer via the thermal tape method as outlined in Appendix B.1. The thermal tape allowed the placement of graphene on the sensor in an expeditious fashion.

2.4.2 Bonds

Graphene coated surfaces have been shown to interact with ssDNA, DNA and fluorophores [61]. This is due to the orientation of the p-orbitals above and below the hexagonal plane of the carbon atoms. Figure 2 represents the two dimensional energy band gap perpendicular to the graphene plane and shows the directions in the Brillouin zone.
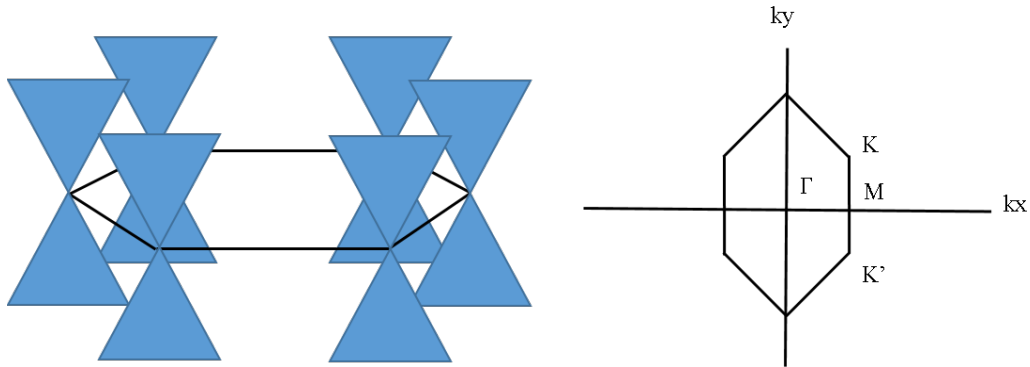
Figure 2: Energy bands for graphene structure in blue represented in k-space. The hexagonal shape represents the lattice structure for graphene. Data from Figure 1.1 in [67].

The lowest unoccupied molecular orbital π bonds noncovalently anchor PBASE, ssDNA and cDNA to graphene. This model is useful because it shows how ssDNA aptamers form π- π bonds on graphene and releases upon recognition of cDNA. Sanchez posits the binding occurs due to van der Waals like forces between ssDNA and graphene

oxide [69]. This assumption is elucidated by Song, Cuniberti, Sanvito and Fang that show the mechanical and electrical interactions between graphene nanoribbons versus adenine, thymine, cytosine and guanine nucleobases. They note that a single adenine nucleobase is undetectable on graphene due to a lack of oxygen atoms whereas the oxygen on the thymine, guanine and cytosine nucleobases contributes to electrically distinguishable absorption characteristic above 0.6V[70].

2.5   Sensor Base/Substrate

A substrate is something that the graphene attaches to for structural stability. The substrate can be any material that will allow graphene to stay structurally sound. This research explored silicon carbide and arsenic doped silicon wafer with thermal oxide on one side to determine the best surface layer that would keep graphene stable.

2.5.1   Structure

Silicon carbide (SiC) wafers and silicon (Si) wafers with thermal oxide layers were explored as potential substrates for the biosensor base. The SiC substrate was initially selected as the sensor base due to the ability to be chemically polished to a surface roughness of less than 0.5 nm [71], access to surface carbon bonds [72] and ease of functionalization via surface carbon bonds[73]. The thought being a smooth surface would allow for better current flow due to less interference. The SiC crystal structure expresses multiple atomic lattice arrangements (or polytypes) that can be used as bases to construct surfaces with minimal variations across a plane. Out of the 215 identified polytypes [73], the 4H and 6H were considered for exploration as the 4H and 6H π-π bond structures were seen as the most optimal for PBASE bond stabilization. The 6H

variant was expected to be superior due to the hexagonal crystal structures ability to near lattice match the hexagonal base of PBASE. Unfortunately, only 4H SiC wafers were available. The untreated 4H SiC sample had a resistance of 8.9 GΩ. The resistance of the sample reduced to 19.7 kΩ after the graphene transfer from thermal tape. While it was an impressive resistance reduction, the average price of a single 4H-SiC, 2-inch diameter wafer was between \$300.00 and \$1000.00. The 6H variants were even more expensive [71]. The use of the SiC sensor substrate base was shelved until more funds and a better understanding of the aptamer functionalized graphene layer interaction was available.

Silicon wafers with thermal oxide coats were explored as a next step. The available silicon wafers had a 100 mm diameter, were n-doped with arsenic, had a (100) orientation, a resistivity of 0.002-0.005 Ω-cm, a thickness of 500-550 µm and a 1 µm thermal oxide on top. These properties and the ability to generate 6 circuits per wafer, at \$100.00 for 25 wafers, was much more useful on a limited budget. The thermal oxide layer provided sufficient insulation from Si and allowed for easy placement and quick functionalization of the graphene surface. This resulted in the Au-Cr probe configuration used in multiple biosensors designs [19], [20], [74], [75].

2.5.2   Chemical Bonds

The 1 µm thermal oxide layer on the silicon wafer provides insulation for the circuit. Thermal oxide layers form smooth surfaces that allow graphene to be exfoliated in a relatively flat manner and help PBASE functionalization once it is introduced onto the sensor surface. Figure 3 shows a side view of the functionalized area that constrains

29

the sensor. The first metallic layer consists of chromium 30 nm high. Chromium serves

to anchor gold to oxide layers. The second metallic layer consisted of gold 70 nm high.
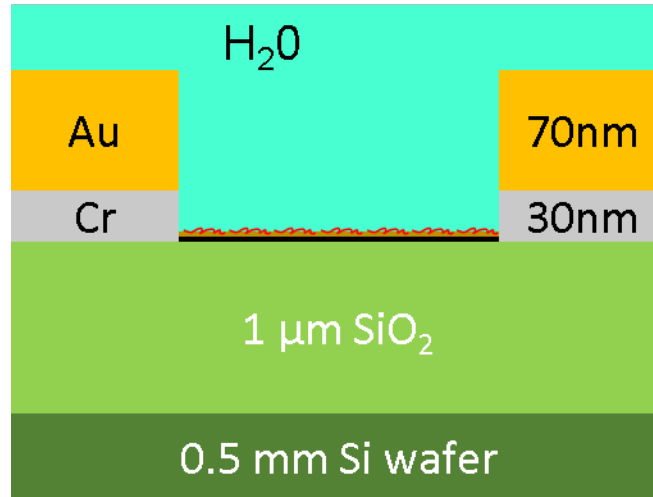
Figure 3: Circuit cross section. The graphene layer
denoted in black is approximately 0.34nm to 10nm high.
The ssDNA22bp aptamer is approximately 7nm long
when attached to the PBASE. The ssDNA77bp aptamer
is approximately 10 to 27 nm long depending on the
configuration it is in when it attaches to the PBASE.

2.6   Sensor Design

Sensors have three elements: an input, a transducer and an output. This particular

sensor is a label-free DNA biosensor that could be analyzed with metal-oxide

semiconductor field effect transistor (MOSFET) equations once the design becomes more

standardized.

2.6.1   GFET Sensing Principles

The graphene FET biosensor physical sensing principles are analogous to the

sensing principles associated with metal-oxide semiconductor field effect transistors

(MOSFET). A simple view of a MOSFET consists of a source voltage, drain voltage and

gate voltage. Figure 4 shows the input source voltage (V_S), the output drain voltage (V_D) and the graphene-PBASE-ssDNA sensor gate voltage (V_G). Note that the gate voltage is considered in an "off" setting when the aptamer is not interacting with the target DNA and in an "on" setting when aptamer is interacting with the target DNA.
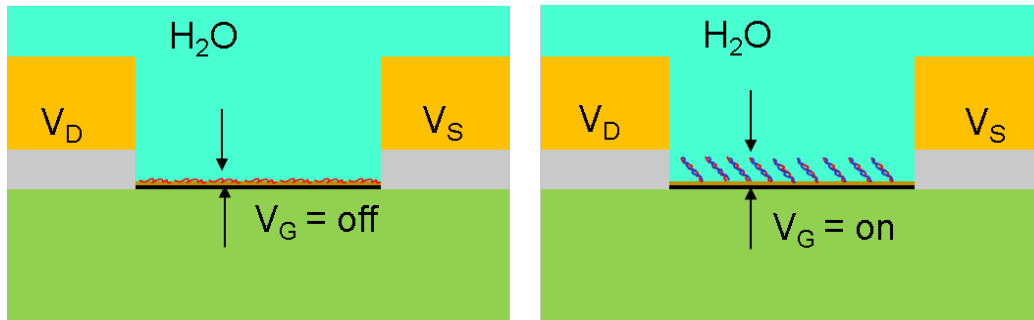
Figure 4: MOSFET Representation of GFET circuit with ssDNA aptamer.

If an agent with the correct target DNA sequence gets close enough to the ssDNA aptamer, the hydrogen bonds and van der Waals forces recognize each other via structural differences and attach the ssDNA aptamer to the cDNA. This binding event changes the state of the aptamer which interacts with the graphene and ultimately changes the sensor response [76]. Detection events are due to aptamers binding to their complimentary sequences and interfacing with the graphene surface. The detection event can be measured in two ways. The first way is to monitor a change in current across the aptamer functionalized graphene surface. The second way is to attach fluorophores to the end of a complimentary sequence and interrogate them after the binding is finished.

The challenge of detecting agents with aptamers requires an electrochemical understanding of the aptamer, the interaction of the aptamer and target analyte, the

reaction environment, and the optimal aptamer density needed to detect an agent in order to send a positive, unambiguous capture signal. These challenges are not unique to any particular biological sensor system, they have been stated here to give the reader an appreciation for the little things that go into a sensor system.

The biosensor is constructed from graphene, a 1-pyrrolidinedione succinimidyl ester and a single strand DNA (ssDNA). Detection is accomplished by a change in current due to the coupling of the ssDNA to its complimentary DNA (cDNA) sequence. The current change is detected via a 4200 SCS Keithley oscilloscope and the data is post processed through MATLAB to normalize the data to percent resistance.

This particular sensor uses conductivity changes from conformational binding events interfering with the graphene surface. These principles serve as the foundation of the sensors and derive from first principles of physics. Resistance can be determined from the resistivity multiplied by the length of the path the current "flow" divided by the area the current flows through and is given by:

$$R = \rho * \frac{l}{A} \quad \text{(Eq. 2)}$$

Where: R = resistance (Ω)

l = length of material (m)

A = area of resistance (m^2)

ρ = resistivity (Ωm)

Resistance can also be experimentally determined and derived from Kirchoff's voltage law, given by:

$$R = \frac{V}{I} \qquad \text{(Eq. 3)}$$

Where: R = resistance (Ω)

V = voltage (V)

I = current (A)

The conductance is just the inverse of the resistance or the rise of the current over the run of the voltage as given by:

$$G = \frac{1}{R} = \frac{I}{V} \qquad \text{(Eq. 4)}$$

Where: G = conductance (S or Ω^{-1} or mhos)

R = resistance (Ω)

Conductance measurements are very useful as the change in slope of the I-V curve is directly proportional to the conductance of the material under study. The knowledge of the properties of deionized water ($\rho = 18.18$ MΩ-cm, pH = 7.0 at T = 25 °C) [77] can help determine acceptable values for circuit resistance.

2.6.2   Mathematical Models and Biosensor Standards

First principle models, previous sensor detection limits, and stated DARPA requirements were used estimate the amount of graphene, PBASE, and ssDNA needed to detect an average of 0.3 to 10^5 *B. anthracis* particles per liter of solution [25]. The spread of PBASE over the graphene, and the ssDNA and cDNA concentrations on the sensor platform were random and no attempt was made to characterize the actual pattern. The silicon wafers used for the sensor substrate were cut from standard wafers down to rectangles of size 29mm by 22.5mm. These dimensions allow the sensor base to be

33

inserted into the microfluidics test chamber. The silicon dioxide on the silicon wafer is 1 µm in height. It can be assumed that the surface oxide is relatively flat.

The number of PBASE molecules that attach to the graphene substrate can be estimated with an approximate PBASE model and knowledge of the graphene area. The area per PBASE molecule can be calculated under the assumption that the four benzene rings on the base are stiff, the average carbon-carbon bond length is 141 pm [78] and that succinimidyl ester tail is approximately the same length as the PBASE as shown in Figure 5.
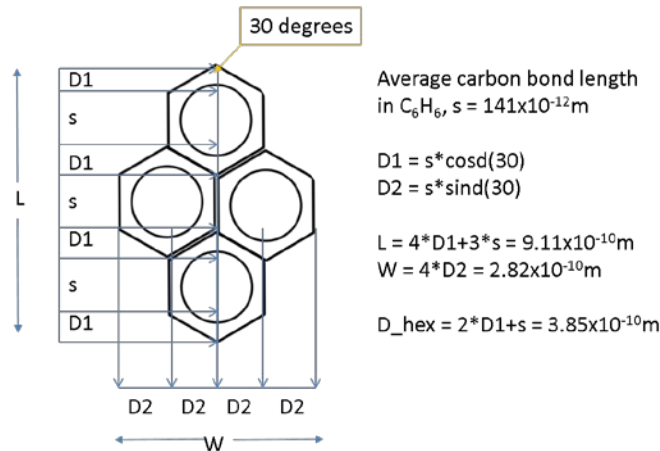
Figure 5: Estimated PBASE dimensions.

The length of the tail and one-half the length of the base can be used as the radius for an area estimate for a PBASE molecule. The rough estimate of a PBASE molecular area is approximately $5.866 \times 10^{-18}\,m^2$. Given a graphene area of $3.0 \times 10^{-7}\,m^2$ (0.6mm by 0.5mm) divided by the PBASE molecular area estimate of $5.866 \times 10^{-18}\,m^2$ gives 5.11×10^{10} available PBASE sites. A 5 µL volume of 10mM PBASE concentration gives approximately 3.011×10^{16} PBASE molecules. These calculations indicate PBASE would

cover an atomically flat graphene surface. However, in reality, the surface oxide will be much rougher and cause graphene to take on shapes that undulate and kink in certain regions. These surface features increase the number of PBASE sites and PBASE molecules needed to coat the graphene surface.

A single rod shaped *B. anthracis* can be approximated as a cylinder 3.0 µm long with a 1.0 µm diameter. Since the bacterium shape shrinks by 20% when it undergoes sporulation, the spores are estimated to be spherical and 2.0 µm in diameter. The estimated detection concentration values for *B. anthracis* are stated between 0.3 and 10×10^5 particles per Liter[25]. These values are more practical stated as 1 particle per 3 Liters to 11,112 particles per Liter.

The key DARPA sensor metrics [25] of sensitivity, probability of detection, false positive rate and response time are discussed below. Additional attributes are unit cost, operation cost, maintenance (mean time between maintenance), reliability (mean time between failure), size, weight and power consumption. Sensitivity per DARPA, is defined as:

$$m_{DARPA} = \frac{n}{V} \quad \text{(Eq. 5)}$$

Where: m = sensitivity (particles/liter or mg/m^3)

n = number of particles or mass (particles or mg)

V = unit air volume (liters or cubic meters)

Notice the volume definition in sensitivity is measured in units of air volume. This is slightly different than the standard chemistry concentration of molarity that deals in moles per liter of liquid solution.

The probability of detection was defined by the following equation:

$$P_{C>T} = \frac{2}{\sigma * \sqrt{\pi}} * \int_{T}^{\infty} e^{-\frac{(x-\mu)^2}{\sigma^2}} dx \quad \text{(Eq. 6)}$$

Where: $P_{C>T}$ = probability of agent concentration

exceeding sensor threshold

T = detection threshold to detect

x = random variable

μ = mean sensor detection

σ = standard deviation sensor detection

Ivnitski also states that biological sensors should be able to detect the agent at threshold concentrations between 5 and 10 minutes [11].

The false positive rate in DARPA's study is classified but a break-even false positive rate was defined as a linear function with the break-even false positive rate per operation versus the probability of attack. The y and x axis ranging from 0 to high.

The response time shown in Figure 6 is a function of the agent release time coupled with the agent arrival at sensor. The sensor response time is defined as the time it takes the sensor to detect the agent after it arrived at the sensor. Once the sensor detects the agent there is the protection response time before the agent arrives at the troops. The sensor response is highly situation and mission dependent [25].

36
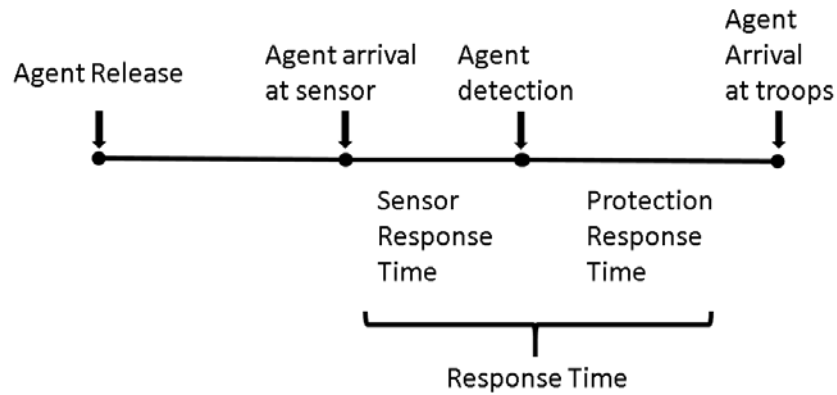
Figure 6: Biological Warning Response Time. This is a linear representation of the timeline associated with agent release to agent arrival at the troops. Data from [25].

There was one important point to note in the DARPA recommendations, "Sensitivity should always be stated with the probability of detection, the false positive rate and the response time." The figures of merit that clinicians and chemists regularly identify with are sensitivity, selectivity and limit of detection from [79] and [80] in equations 7, 8 and 9:

$$m = \frac{\Delta R}{\Delta c} \qquad \text{(Eq. 7)}$$

Where: m = calibration sensitivity

R = response (output)

c = concentration (input)

This particular measure can be useful as the response of the electrical signal is based on the concentration of the analyte (target aptamer in this case) as it flows over and interacts with the sensor. This measurement still does not bridge the gap between the

stated DARPA sensitivity simply because it measures concentration as a function of aqueous fluid medium and not air. The selectivity is given by:

$$S = \frac{m_{analyte}}{m_{reference}} \quad \text{(Eq. 8)}$$

Where: S = selectivity

$m_{analyte}$ = slope of the analyte concentration

$m_{reference}$ = slope of reference concentration

This measure could be useful because the slope of the analyte and the slope of the reference concentrations could be determined from the response data. The limit of detection is given by:

$$DL = \frac{k * s_b}{m} \quad \text{(Eq. 9)}$$

Where: DL = detection limit

k = confidence factor (k=2, 92.8%; k=3, 98.3%)

s_b = standard deviation of the blank

m = calibration sensitivity

Repeatability measures the ability to obtain similar answers under similar analytical conditions, whereas reproducibility measures the ability to obtain similar results under varying analytical conditions [80]. These differences may seem minor but

they are important because they determine sensor capabilities outside of a laboratory environment.

The differences between these sets of measurements outlines the terminology used between academia and the defense industry are potentially at odds, confusing and may have helped undermine the ability for the biodefense industry to take hold or accurately tell its customers what they purchased. The mathematical description of agent concentration to agent dosage consists of eight independent variables that need further refinement before use in a laboratory or field environment.

III. Methodology

This chapter describes the methods used to acquire the signals from the DNA used in this study. The water was filtered via a Millipore system with two 0.22 µm filters to make it ultrapure deionized water (DI). The laboratory temperature was 303K. The general outline is given below with each section devoted to the necessary setup issues. The first section focuses on the microfluidic chamber setup and the process used to test target DNA in a dynamic aqueous environment. The second section discusses the Raman laser spectrometer setup and the process used to determine the indirect fluorescent detection indicative of target DNA binding to the functionalized surface ssDNA. The third section discusses the static drop test setup and the processes used on target DNA and spores for the static drop test. The fourth section explores atomic force microscopy to show the target DNA and surface immobilized DNA and spores binding on the surface.

3.1   Sensor Development and Construction

Two circuit designs were constructed to test ssDNA to cDNA conformational binding in dynamic and static aqueous environments at specific concentrations via changes in I-V curve slope and magnitude. The first sensor type was a two terminal variant. The second sensor type was a three terminal variant. Both sensor types were tested as two terminal variants due to equipment issues. The sensor base, an n-type silicon wafer with a 100 µm thermally grown oxide finish, was used as a cheap, flat surface to test the sensor on. Graphene was grown via the method outlined in Appendix B.1. The transfer to the silicon dioxide wafer was accomplished by placing the thermal tape on the silicon wafer and putting the wafer onto a hot plate heated to 125 °C. The thermal tape turned whitish and peeled off the silicon wafer surface after 10 to 20 seconds. Tweezers were used to carefully pull the tape off the silicon wafer. The graphene left behind a purple tinge on the surface of the silicon oxide wafer that can be very hard to see if viewed straight on. The Manchester group determined a way to optically estimate the thickness of graphene on a silicon substrate [81], [82]. Fresnel equations can be used to determine the thickness of the graphene layers by equating the graphene thickness $d = k*0.34$, where: d is the graphene thickness in meters and k is the individual graphene layer. Alternatively, the observed contrast can be quantified by extracting the green component of the RGB colors from digital photographs. The difference between the green contrast of the graphene and the green contrast of the substrate takes discrete values corresponding to $k = 1$, $k = 2$, $k = 3$ layers of graphene[68].

The graphene transfer can be detected with a digital camera and software with an inverse filter see Figure 7. This method was an easier way to determine if the thermal tape had transferred its contents to the graphene surface.
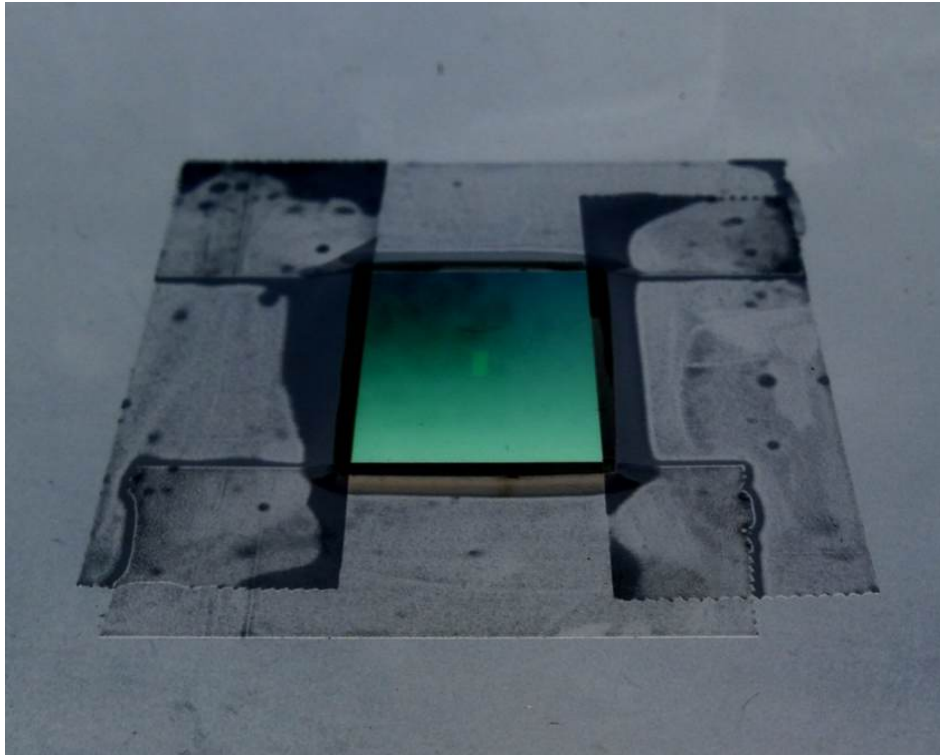
Figure 7: Graphene (light white rectangle in the middle of the sensor)
transferred from thermal tape in center of silicon wafer before masking.
Taken with iPad Retina, 5 Megapixel camera, inverse filter applied from
PicLab HD.

After the graphene is placed on the silicon wafer, the resistance across the graphene sheet is checked with a digital multi-meter to ensure it is in place and can conduct. The usefulness of the measure stems from the ability to tell if the graphene is in place. The next step is to mask the circuit with a Scotch tape outline of the two or three terminal device. The blank areas are where Au-Cr will be deposited on the thermal oxide surface (outlined in Appendix B). After metallization the circuit is stripped of Scotch

tape and annealed in a furnace at 300 °C for 4.5 hours. This allows the Au-Cr-SiO$_2$

layers and the Si wafer to relax system dislocations brought about by the initial

construction process and burn off the adhesives associated with the thermal tape transfer

of graphene and the Scotch tape patterning. Once annealing is finished, the circuit is

ready for functionalization by pyrene and ssDNA (see Appendix B.3 for recipe). The

finished circuit layout is shown in Figure 8.
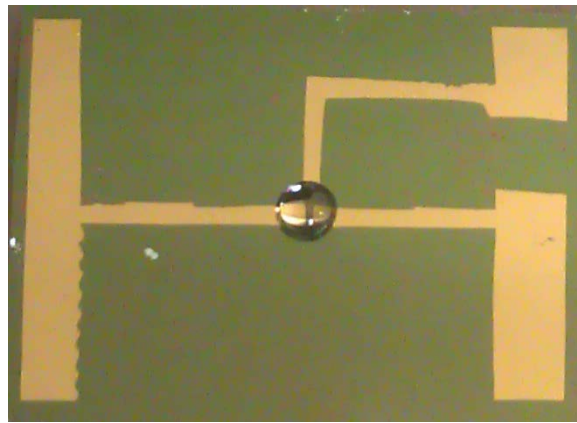
Figure 8: Si-SiO$_2$ base with Cr-Au patterned leads in a three terminal configuration with the graphene-ssDNA functionalized surface highlighted by the deionized H$_2$O clinging to the surface. The functionalized area measures 0.5mm by 0.61mm.

This process takes approximately one hour, after which time the graphene-

PBASE surface can be functionalized with an aminated ssDNA. The aminated ssDNA

attaches to the PBASE via the succinimidyl ester at standard temperature and pressure

(303K, 0.987 atm) in a deionized H$_2$O solution. The reaction takes 18 hours to complete.

The remaining polar amino acid groups on the ssDNA bind into the graphene and create a

surface that can be used as a sensor platform. This circuit is similar to a field effect

transistor circuit where a gate voltage is applied between a source and drain voltage in order to force an electric field deformation to allow the conduction of electrons. This setup differs such that the gate field can be thought of as controlled by cDNA conformational binding to the ssDNA on the surface modified graphene. A change in the overall circuit resistance occurs due to the molecular binding event of ssDNA and cDNA.

Raman spectroscopy was used to verify each new surface layer. There are a number of good references that explain Raman spectroscopic theory in detail[55]. It is a technique used to illuminate molecules at a specific coherent wavelength and detect the inelastic scatter of light waves from the illuminated molecules. The inelastic scatter of light waves represents as a set of vibrational frequencies that allows for the compositional determination of sample elements over a wide range of frequencies. The vibrational frequencies are a function of molecular mass and the bond strength of monoatomic or diatomic species. Second order equations of motion give the following equation:

$$ v = \sqrt{\frac{B(m_1 + m_2)}{m_1 * m_2}} \qquad \text{(Eq. 10)} $$

Where: v = frequency (Hz)

B = Bond strength (N/m)

m_1 = atom 1 with mass (kg)

m_2 = atom 2 with mass (kg)

The vibrational frequency depends on the addition of mass to the sample and decreases as the sample mass increases. This frequency-mass relationship conceptually describes the addition of PBASE, ssDNA and cDNA layers to the graphene base on the thermal oxide substrate. This relationship extends to the energy-wavenumber relationship used by spectroscopic technologists to report their findings. The frequency is inversely proportional to wavelength $\nu = c/\lambda$, and when substituted into the energy-frequency relationship gives:

$$E = h * c * \tilde{\nu} * (100 cm / 1m) \qquad \text{(Eq. 11)}$$

Where: h = Planck constant (6.626×10^{-34} J*s)

c = speed of light (2.998×10^{8} m/s)

λ = wavelength (m)

$\tilde{\nu}$ = wavenumber (cm^{-1})

The wavenumber is directly proportional to the energy of the system. This particular method illustrated the compositional changes to the circuit surface as each additional layer was added to the sensor. Table 2 lists the Raman wavenumbers that are expected to be present each time a new layer is added.

Table 2: Raman wavenumbers for circuit functionalization. Data from 600 cm⁻¹ to 4000cm⁻¹ from [83].

Chemical Bonds	Region of vibrational frequency/(cm⁻¹)
O – H	3730 – 3500
O – H (association)	3520 – 3100
N – H	3550 – 3420
N – H (association)	3500 – 3100
C_6H_6	1625 – 1575, 1520 – 1480
C=O (esters)	1760 – 1720
C=O (aldehydes)	1725 – 1715
CC (aromatics)	1600, 1580, 1500, 1450, 1000
n-alkanes	950-1000
Si	520

The graphene G (1590 cm-1) and 2D (2690 cm-1) peak are clearly illustrated in Figure 9. The silicon peak was not included due to its ability to saturate the Raman spectrometer and drowned out the rest of the spectra.
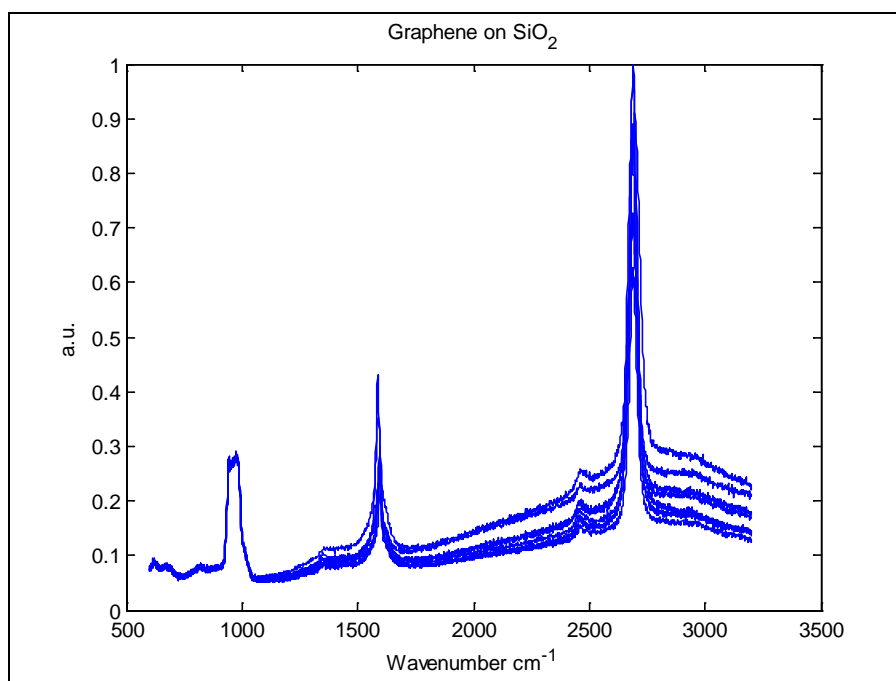
Figure 9: Raman spectrum from 600cm⁻¹ to 3200cm⁻¹ for graphene on SiO_2.

45

The initial Raman spectroscopy circuit tests were with the ssDNA 22bp that showed an increase in the overall peaks of the as layers were added to the circuit. Figure 10 shows the buildup of the graphene functionalized section of the circuit. The laser spectrometer was checked with a silicon calibration unit that generated a standard peak at a 521 cm^{-1}. The spectrometer was calibrated each time to ensure proper elemental identification and to reduce the erroneous identification of specious elements.
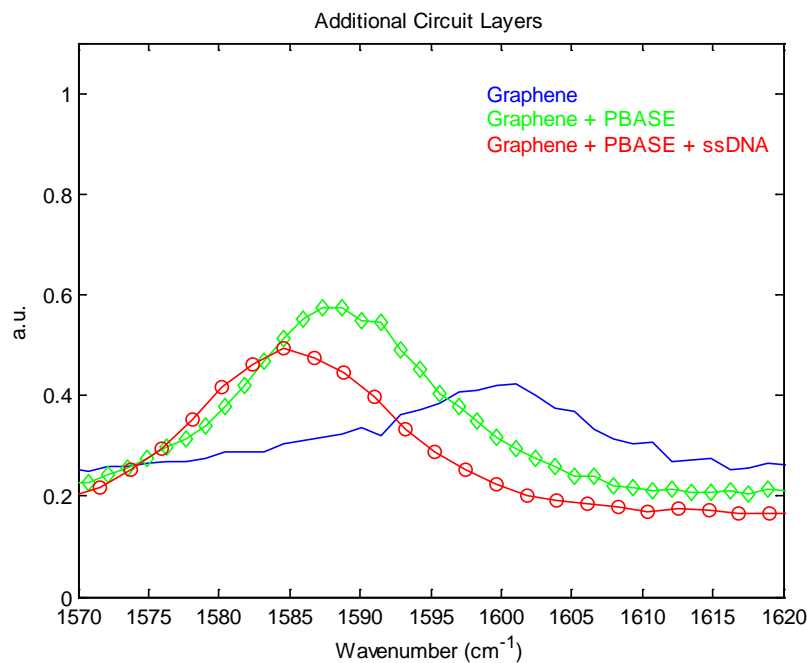
Figure 10: Graphene peak shift with added layers. Raman spectroscopy used to show graphene peak shift for additional circuit layers. Blue line indicates the vibrational spectra of graphene on the SiO$_2$ layer. Green line indicates a shift from 5 µL of PBASE at a 10.0 mM concentration to the graphene layer. Red line represents a shift due to the addition of 10 µL of 50.0 µM ssDNA 22bp bound to the PBASE. Note the wavenumber shifts left as more molecular layers are added to the graphene surface.

Figure 11 shows the differences between a 22bp and 77bp functionalized circuit from a Raman standpoint. The inVia was set to 100% laser intensity (200mW) with an exposure time of 10 seconds from 600 cm^{-1} to 3500 cm^{-1}. This was to ensure a clear

spectrum. The differences between the curves from 1700 cm^{-1} to 3500 cm^{-1} show peak broadening and shifts to the left of the baseline. These are indicators of heavier ssDNA chains attached to the graphene surface.
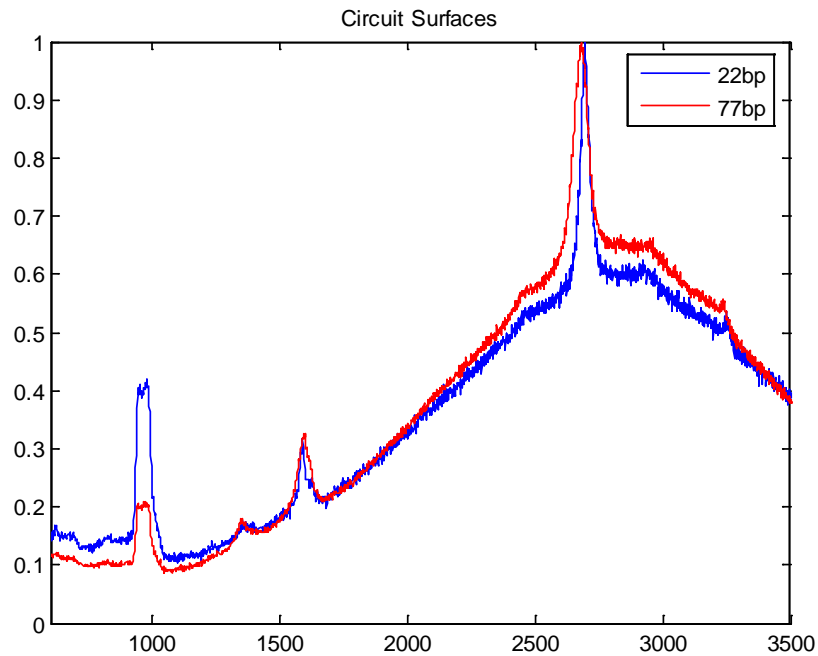
Figure 11: Raman spectrum of 22bp and 77bp circuit comparison. The ssDNA77bp in red shows a more intensity from the ssDNA fluorescence and broader peaks indicating more mass than the ssDNA22bp peaks shown in blue.

Each time a new layer was added to a circuit, seven measurements were taken with the Kiethley 4200 SCS and Student-t distribution was used to determine a reasonable estimate for the circuit resistance. Figure 12 below shows the resistance change as new layers were added to the circuit. This test served as an initial check but did not help determine the resistance of the circuits when they were immersed in dynamic or static fluids as the introduction of fluids provided a surface path that changed the overall circuit resistance.

47
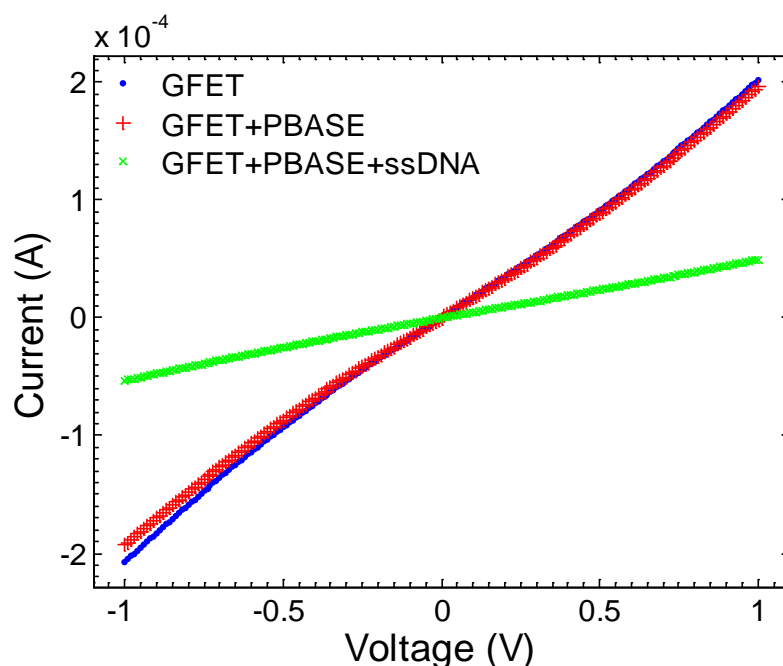
Figure 12: I-V curve for added circuit layers. Current versus voltage curve shows capacitance decrease with the addition graphene, PBASE, and ssDNA. The PBASE had a 10mM concentration and a volume of 5 μL. The blue line denotes naked graphene between Au-Cr contacts. The red line denotes graphene plus PBASE between Au-Cr contacts. The conductance changes between red and blue line are minimal due to π-π bonding between graphene and PBASE. The green line denotes addition of aminated ssDNA to PBASE on the graphene surface.

The current-voltage curve in Figure 12 shows that the conductivity decreases after each functionalization step. This makes sense because each new layer consists of chemical entities that obstruct the original graphene electric field. The PBASE addition to the decreases the circuit conductivity very little which makes sense because the PBASE molecules form π- π bonds with the graphene plane layers in a hexagonal fashion. This setup should minimally interfere with the electron transport across the graphene surface. However, the introduction of ssDNA to the GFET+PBASE surface decreases the conductivity substantially. It has been experimentally shown that ssDNA binds to graphene via the benzene π-π bonds that protrude from the graphene surface[61].

The binding of negatively charged DNA molecules to its surface bound complement increases the impedance on n-type silicon samples and decreases the impedance on p-type samples [84].

Another method was used to regenerate the circuits after they failed from overuse. This method involved transferring graphene on thermal tape to the originally functionalized area between the Au-Cr contacts. The transfer method worked and is verified with a multimeter. The annealing process attached it firmly to the Au-Cr electrodes and the SiO2 surface. However, this transfer process comes at a reduced sensitivity. The sensors that underwent this process could previously detect tens of nM concentrations. This process pushes the detection limit into the hundreds of nM range.

3.2   Electrical Measurements via Microfluidics Chamber

The Dolomite microfluidics chamber has high a pressure transparent polymer that allows researchers to view the sample while eight electrical probes collect data as the working fluid passes over it. The electrical probes connect to the Keithley 4200 Semiconductor Characterization System while the fluid tubes connect to the Flowmeter Syringe Pump and the Eppendorf vial see Figure 13 below.
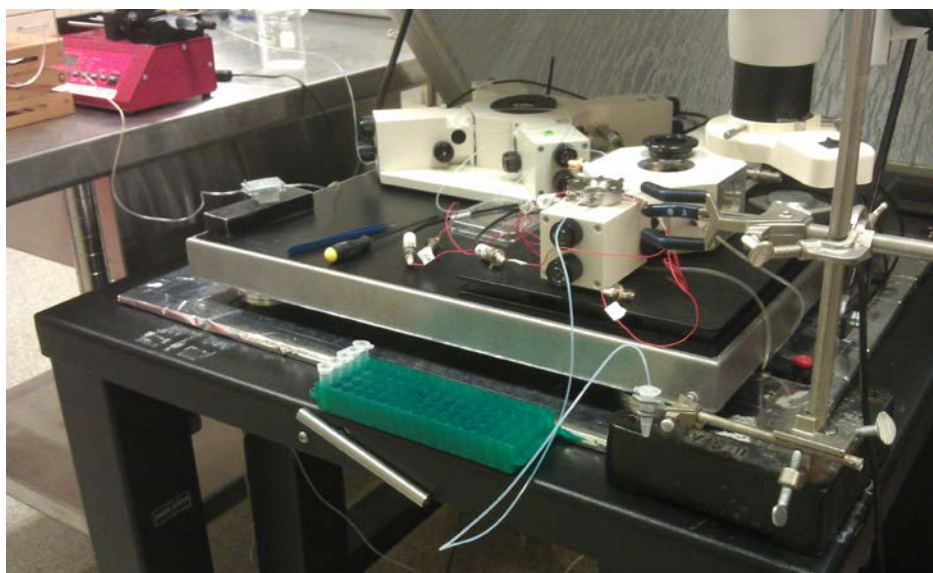
Figure 13: Equipment setup. Dolomite sitting on probe station with the Eppendorf vial on the right hand side and the syringe pump on the table on the far left. The Keithley 4200-SCS is not in the picture.

3.2.1   Electrical Measurements

After the Keithley 4200 Semiconductor Characterization System was powered on the sensor was put into the Dolomite Resealable Unit (DRU) and contact between the electrical probes and sensor leads was verified. This is accomplished visually and by the two terminal resistor function in the KiTE software. The two terminal resistance function displays a two terminal device with the ability to modify the input and outputs for the circuit. The input was set as a linear voltage sweep from -0.2V to 0.2V with a step size of 0.01V. Once the sensor was secure in the Dolomite, tests were run to check the current-voltage (I-V) plot to determine if the circuit had good electrical connections. Suspicious connections were detected by electrical currents less than 10^{-12} A, circuit resistances more than 1.0M Ohms or real time I-V plot showed erratic jumping behavior by 3 magnitudes or more. The circuit was adjusted until the I-V curve is linear. Once the

I-V curve was straight, six more measurements were collected to determine if a statistically valid Student T mean distribution of the circuit resistance was needed to help characterize the circuit.

After the connections were verified, the Dolomite inflow tube was inserted into a 1.5mL Eppendorf vial and the Dolomite outflow tube was hooked up to the Flowmaster Syringe. The Flowmaster Syringe had a maximum 12 mL fluid volume and was set to pump a fluid velocity of 20 uL/min. A pipette of 1000uL DI was injected into the Eppendorf vial to provide an initial solution for the sensor to equilibrate. After this was completed, the syringe pump was turned on to flow water through the tubes and across the microfluidics cell at a constant 20 uL/min. Care was taken to minimize bubble introduction and formation within the inflow and outflow tubes.

To verify laminar flow, the Reynolds Number was calculated using [85] equation 12 which indicates laminar flow for Re < 10000 or turbulent flow for Re > 10000.

$$\mathrm{Re} = \frac{V * D * \rho}{\mu} \qquad \text{(Eq. 12)}$$

Where: Re = Reynolds number

V = fluid velocity (m/s)

D = pipe diameter (m)

ρ = mass density (kg/m^3)

μ = dynamic viscosity (N*s/m^2)

The assumptions of pure Millipore strained deionized water at 25 °C coupled with the information in Appendix A gives an approximate Reynolds number of 6 which is laminar. This information helps characterize flow conditions under which complimentary binding occurs. Nyugen identified and suggested $L_{liquid} = 10$ nm as an appropriate length scale at which to perform molecular simulations on a fluid [86]. This study assumed the flow was continuous and laminar based on the characteristic tube diameter and microfluidics chamber measurements in excess of the length scale recommendations. A computational fluid dynamics simulation would be beneficial to characterize the events in the flow chamber.

Once the DI was flowing through the microfluidics system in a smooth manner, the four terminal function was selected on the Keithley 4200-SCS with the drain voltage and source voltage set to SMU 2 and SMU3 respectively. The driving input for the sensor was the source voltage set at 0.2V with a 0.1A compliance. The sample size was set to 4000 and the sample rate was set to 1 sample per second. The graphing function was opened to monitor sensor progress and the start button at the top was clicked to set the Keithley to start recording. The sensor drain current reading took anywhere from 100 to 1000 seconds to come to equilibrium. If the sensor response was within a 2% envelope for 100 seconds, it was appropriate to inject the target DNA into the Eppendorf vial. This vial served as a fluid injection point where the sample of interest would be dripped down the wall to minimize fluid mixing and prevent air bubbles from forming in the tube.

The target DNA injections were between 100 and 300 µL in volume. Each sample took 120 seconds to traverse the inlet tube at 20 µL/min and another 30 seconds to flow over the functionalized sensor due to the geometry of the microfluidics chamber. The injection actions overlapped the DI water exiting the Eppendorf vial. There was usually a 10 µL mixing of the target DNA concentration with the DI water remaining in the Eppendorf vial. Each target DNA injection was tracked carefully as DI water had to be injected once the target DNA was within 10uL of the bottom of the vial to ensure air bubbles would not get into the tube and interfere with the microfluidics measurement.

After 150 seconds passed from the injection point, the current was monitored to determine if the sensor detected the target DNA within the microfluidics chamber. The area of the chamber is $22.3mm^2$ with a depth of 100um. This volume was adequate to hold 300uL of target fluid at one time. If the measured drain current did not climb above 1% of the mean drain current response, it was deemed a failure and the next target DNA sequence was added. The target DNA sequences and injection times are shown below. They match with the injection times associated with the responses in the results and analysis section. Once the run finished, the KiTE analysis software was stopped to prevent damaging the Keithley 4200 SCS and the Syringe pump was stopped.

After each experiment, the microfluidics chamber was opened and the circuit was removed and washed with DI water heated to 30 °C. This wash step removed any bound DNA and reset the sensor for another test.

The current versus time plots were captured with a Keithley 4200-Semiconductor Characterization System via SMU units attached to triaxial BNC connectors wired into a

Dolomite printed circuit board (PCB) on a resealable microfluidic chamber. The Keithley 4200-SCS was set to the drain-gate-source mode to allow drain current versus time to be collected. The sample buffer was set to 4000 and the sample rate was set for 2 seconds.

The Keithley 4200-SCS was set to the vgs-id mode that can determine the drain current given a particular source and gate voltage. It records current as a function of time which is inevitably a function of the solution concentration flowed across the sensor. The syringe pump in the picture generates a vacuum pressure on the solution and pulls it through the tubes attached to the Dolomite sensor. The Dolomite PCB had eight electrical probes (four on each side) perpendicular to the fluid flow that allowed for the multichannel information capture. The ssDNA and cDNA solutions were channeled from a 2mL cuvette in an 808.4 mm long, 0.8 mm inner diameter tube to a resealable sensor platform with a volume of 16.73mm^3 (11.00 mm wide and 20.4 mm long with triangular inlet and outlet regions). The target DNA solutions flowed through the chamber and interfaced with the functionalized sensor for approximately 100 to 300 seconds. Afterwards the solutions were flowed out of the chamber via a syringe pump at a constant flow rate of 20 uL/min. Approximately 1mL of dH2O water was drawn across the sensor before exposing the sensor to three separate cDNA concentrations in 3 mL water. This data provided a point to compare this system to other sensors. The initial data for the two terminal circuit shows a minimal decrease in current over time. Preliminary results show the current at 10.8 µA going to 10.63 µA in dH$_2$O and from 10.63 µA to 10.49 µA under a range of concentrations of cDNA from 10^{-12} to 10^{-7} M. The cDNA

sequence should force the ssDNA to unbind from the graphene surface and orient itself away from the graphene plane. To test this theory, ssDNA sequences 22bp were aminated and used to functionalize the graphene surface on specific circuits to provide a baseline and help interpret the methods used and data collected. The second ssDNA 77bp with the Texas-Red fluorophore on the 5' carbon serves as a test to see if the transduction element recognizes and attempts to bind it to the graphene surface. The third DNA sequence was the cDNA 77bp with a 5' Texas-Red fluorophore modification. The cDNA is the full complimentary sequence to the transduction element. The fourth DNA sequence was a half complimentary sequence used to determine if and how the functionalized area would response to a "half" input. The fifth DNA sequence, ssDNA 22bp, was a test sequence used to evaluate sensor construction. The sixth DNA sequence was the cDNA 22bp used to help test the ssDNA 22bp sequence and also was used against the ssDNA 77bp to attempt confuse the sensor.

3.3   Raman Spectroscopy

Raman spectroscopy was picked due to its ability to determine composition of thin film layers and the minimal setup required to gain data on the sample under test.

3.3.1   Raman Procedure

The Raman vibrational frequency measurements were taken with the Renishaw inVia Raman Microscope with a Diode-Pumped Solid State (Nd:YVO$_4$), 532 nm Laser, Class IV operated at 200mW (100%). The inVia uses the WIRE3 software package to control the laser beam, aperture, sample plate XYZ motion, lights, laser exposure, etc., in the sample illumination container. Operation of this unit requires OD+6 goggles

specifically designed to block the 532 nm laser light. The Wire3 software package was started and checked to ensure the laser aperture was closed before opening the illumination chamber. System calibration was accomplished by focusing the smallest coherent laser onto the standard Renishaw silicon block and monitoring the vibrational frequencies for the expected 521 cm^{-1}. The calibration was repeated if the system was off by more than 2cm^{-1}. The calibration was performed each time a test sample was put into the chamber to ensure a reliable analysis.

Once the in-Via was calibrated, the sample circuit was placed in the illumination chamber on a small conductive block. The optics were set to 50X and adjusted to focus on the functionalized circuit area to ensure the laser was pointed at the right area. The laser was checked again to make sure the beam was collimated for the best possible picture. This involved turning the illumination chamber light and camera off while opening the laser aperture with a reduced power setting of 0.0001%. The beam was focused to the smallest circular size recognizable on the monitor.

Two types of measurement modes were performed for every circuit layer addition. The spectral acquisition mode illuminated a section of the sample within the functionalized area. The optical camera was used to ensure the laser was pointed at the correct region. The spectral acquisition setup Range tab grating scan type was set to the extended option which allowed for a user definition of the spectrum range which was set from 600 to 4000 Raman shift/cm^{-1} for each measurement to block the Si signal and capture the rest of the frequencies of interest. The confocality was set to standard. The configuration laser name was set to 532 nm Edge in the Laser Name field. The grating

name was set to 1800 l/mm (vis) and the detector name was set to the Master: Renishaw

CCD camera. The Acquisition tab exposure time was set to 10/s, with the Accumulations

set to 1, the Objective set to 50 and the Laser power % set to 100. The range ($600cm^{-1}$ to

$4000cm^{-1}$) excluded the detection of the Si vibrations due to their ability to saturate the

detector and reduce the detectability of signals of interest from graphene, PBASE,

ssDNA and ssDNA-cDNA binding. Each spectral measurement was taken within the

section between the Au-Cr electrodes see Figure 14. The functionalized area on average

was approximately $7.92x10^{-7} m^2$.
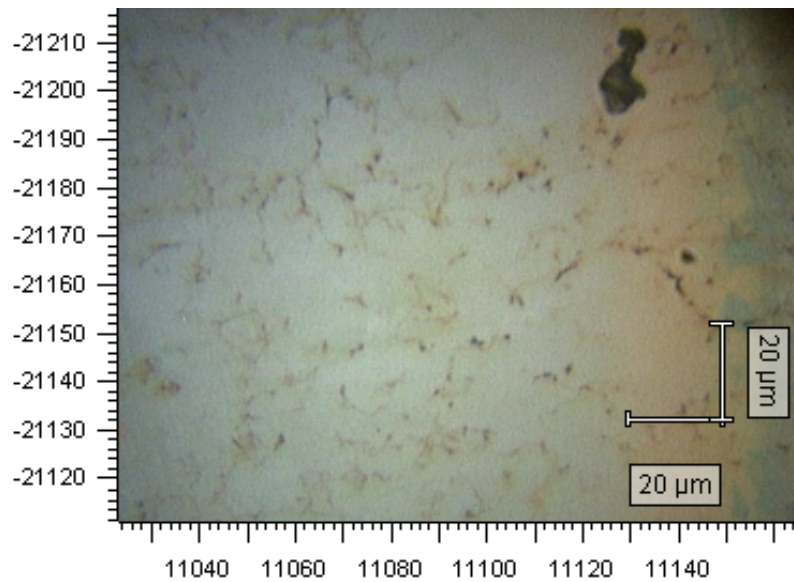

Figure 14: Graphene functionalized with ssDNA 77bp. Optical shot taken at 50X between Au-Cr circuit connects in in-Via Renishaw laser spectrometer.

Figure 15 shows the typical atomic composition of silicon, oxygen, and graphene

in the functionalized area of the circuit. The baseline generates the departure point for

confirmation of the addition of PBASE, ssDNA and cDNA circuit layers. The

wavenumbers from 925 cm^{-1} to 998 cm^{-1} are trigonal ring breathing modes from mono and meta-substituted benzenes, the peak at 1350 cm^{-1} is the graphene D peak. The peak at 1590 cm^{-1} is the graphene G peak. The peak at 2690 cm^{-1} is the 2D peak from graphene. The peak at 2900-2950 cm^{-1} is identified with n-alkanes (CH$_2$ stretch). The peaks at 3200-3300 cm^{-1} are primary amines (bonded antisymmetric stretch NH$_2$) [87]. The variation is due to experimental nature of the circuit construction.
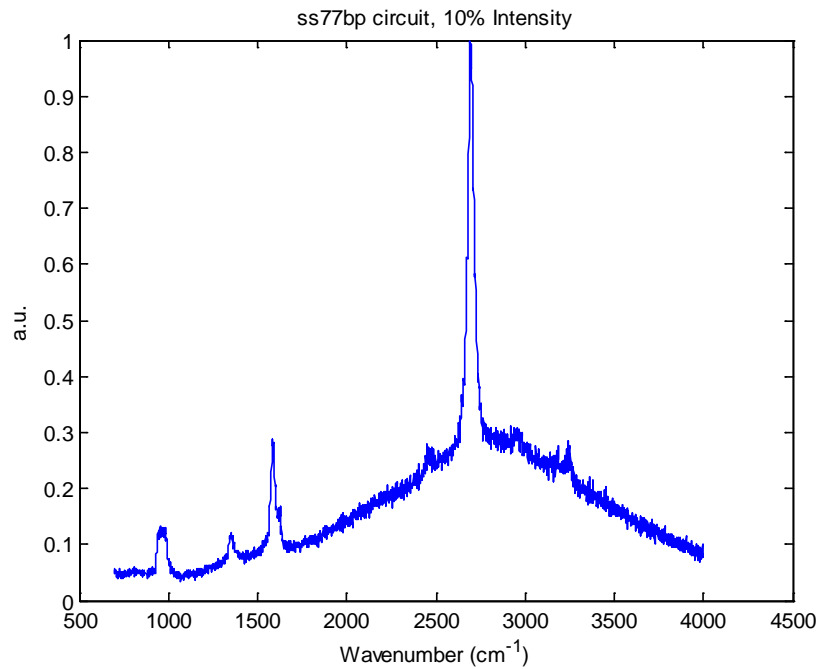
Figure 15: Graphene functionalized with PBASE [10µM] and ssDNA 77bp [50 µM] on SiO$_2$ layer.

The second measurement function used was the map acquisition mode that takes sample data from a user-defined area. The range and exposure times were kept the same as the spectral acquisition mode to provide equivalent data comparisons if necessary. The map acquisition mode on average collected 20 samples in a boxed region over a 20-

58

30 minute period. The region was selected at random within the functionalized area. The data was saved to a text file for reconstruction and review in MATLAB.

3.3.2   Raman Spectroscopy Measurements

The data shows a relatively smooth surface based on the CVD grown and mechanically exfoliated graphene on the surface based on the ID/IG ratio of 1.8. The Au and Cr portions do not show up on the Raman measurements because the laser illuminator was specifically aimed in the graphene functionalized regions of the circuit. The wavenumber values were in good agreement with other papers on the subject of Raman spectroscopy and graphene [88]. Ferrari and Basko[89] noted that the full width half maximum (FWHM) of the graphene G peak always increases with disorder. This was noted a number of times and helped indirectly confirm certain molecules were on the functionalized circuit area. Raman spectroscopy can also indirectly detect the fluorescence from DNA showing that the ssDNA and cDNA underwent complimentary binding see Figure 45, section 4.2.5.

3.4   Static Fluid Test

The electrical probe chamber was used to explore drop-by-drop aptamer solution analysis on a circuit with its electrodes and sensor area exposed to open air. This method simulated an open air environment that one could expect if the sensor was out in the field. The functionalized area supported this assessment by having a unique hydrophilic property that allowed droplets of from 1 µL to 10 µL to stick to the circuit surface.

59

3.3.1 Static Fluid Test

The static fluid test was accomplished by putting the functionalized circuit into

the probe chamber and lowering the electronic probe tips onto the surface electrodes as

shown in Figure 16.
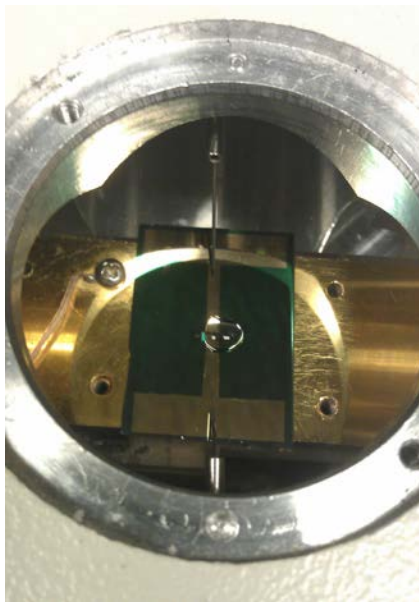
Figure 16: Static test setup.
Performed on ssDNA 77bp
functionalized chip. The solution on
the chip is 10uL, 50 nM of target
DNA. The probes are set to record
current changes for a fixed 0.2 volts.

The target DNA was added to the sensor in 1uL, 5uL and 10uL increments via

pipette to determine the overall change in current as a function of time. That information

was recorded via the Keithley 4200 SCS with the four terminal function set to the same

parameters as the microfluidics test.

3.5   Atomic Force Microscopy

Atomic force microscopy (AFM) was developed by Binning at IBM developed it in 1982 [90]. AFM tapping modes work by detecting the deflections of a cantilever beam as it passes over the sample surface. Simple beam equations can help determine the resonant frequency of the beam. The AFM used in this research has a coherent laser beam focused on the top of the beam. As the beam vibrates from surface interactions, photodetectors pick up the diffracted laser light and use sophisticated equations to determine the amplitude and the resonant frequency of the cantilever beam. This information is converted into a coherent signal that is displayed as magnitude or phase information to the operator [91].

Using the tap mode AFMs can determine the surface roughness of the graphene on the SiO_2. Since ssDNA and cDNA are bound to graphene the general binding is occurring on the surface of graphene. It can be used to determine the roughness of the graphene surface, the attachment and distribution of the PBASE and DNA over the surface. AFM can detect surface changes on the order of 1 nm. This is important as the helical DNA used in the experiment has a 2.0 nm diameter and form structures roughly 6.0 nm to 30.0 nm in size.

3.6   Fluorescent Spectroscopy

Fluorescent spectroscopy can used as a qualitative measure to determine if complimentary binding is occurring between ssDNA and cDNA. Fluorescent probes have helped decrease DNA labeling dangers by providing alternatives to radioactive phosphorus probes that were attached to the 5' DNA phosphate backbone [92].

3.6.1 Fluorescent Theory

Fluorescence occurs when electrons are imbued with enough energy to jump from the singlet state S0 to the singlet state S1 in a molecule and relax from S1 back to S0 and emit a photon [59]. Phosphorescence is different from fluorescence due to an intermediate triplet state T1 that prevents the electron from relaxing from S1 to S0 [59]. Photon emissions under $1.0x10^{-8}$ seconds are considered fluorescent, while photon emissions over $1.0x10^{-8}$ seconds are considered phosphorescent [91].

3.6.2 Fluorescent Measurements

The design of the circuit and the generation of microfluidic data did not allow for a direct fluorescent analysis to take place. However, the 77bp target aptamers were functionalized with Texas-Red fluorophores and their fluorescence was indirectly detected with Raman spectroscopy. The setup used for this particular set of measurements is the same as previously discussed under Raman Spectroscopy with the exception that circuits with cDNA 77bp targets were used to indirectly show fluorescence.

IV.   Results and Analysis

This section is divided into two major sections which address the 22 base pair functionalized circuit and the 77 base pair functionalized circuit for easier comparison. To standardize results and allow for comparison of circuits, the microfluidics drain current data and the static drop test data were converted to percent resistance standardized to the initial resistance of the circuit under test.

The equation used is:

$$R_{Percent} = \frac{(R(t) - R_0)}{R_0} * 100\% \quad \text{(Eq. 13)}$$

Where: $R_{Percent}$ = percent change in resistance

R_0 = initial resistance (Ω)

$R(t)$ = resistance at time t (Ω)

t = time (s)

Preliminary results suggest the reactions are second order kinetic reactions. Further tests are needed to characterize the second order kinetic effects due to substrate and functionalization variances. Most of the data taken below was at one aptamer concentration for each test. The 22bp aptamer was functionalized using 5uL of 10mM concentration diluted to 10uL on the circuit surface whereas the 77bp aptamer was functionalized using 5uL of 50uM concentration diluted to 10uL on the circuit surface. The amount used to functionalize each circuit was due to economic considerations.

The working solution for this process was deionized water filtered by Millipore in 0.22 µm filters. A test was done to determine the conductivity of the deionized water without a graphene interconnect. Figure 17 shows the current over 7000 seconds. There are a few spikes in the data that were due to personnel bumping into the setup apparatus. The causes of the other disturbances is unknown but could represent tiny bubbles in the microfluidics chamber interfereing with the sensor results. The mean current that could travel through the water was approximately 2.4025×10^{-11} A, which was 5 magnitudes

63

smaller than the electrical current the sensors regularly recorded under test. Taken as a

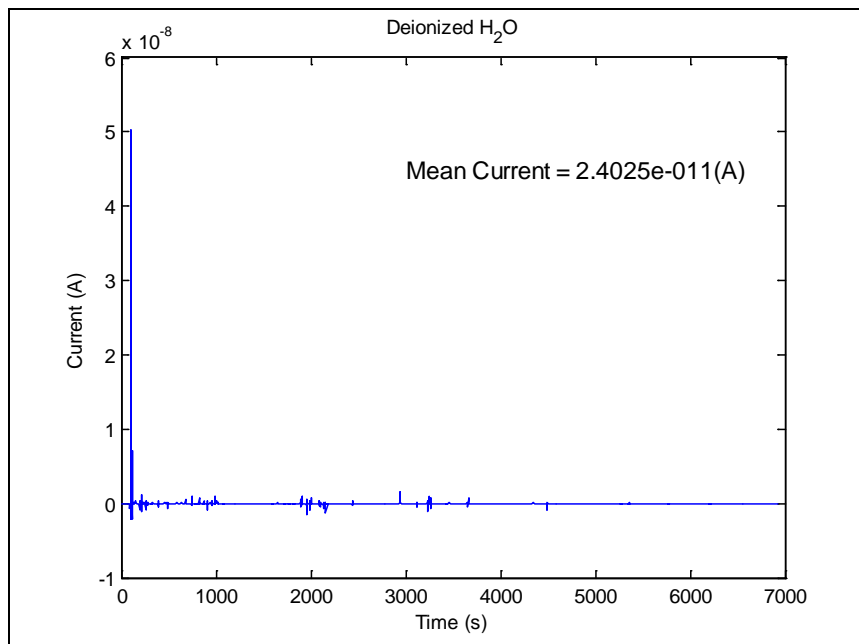whole, the conduction of deionized (DI) water was minimal at best.

Figure 17: Deionized water double filtered through a 0.22 um Millipore dispenser.

The test was performed with a graphene free circuit to demonstrate minimal electrical

current travel within the fluid medium. The voltage for this test was set to 0.2V, which

gives a resistance of 8.325 MΩ.

4.1   Results and Analysis for ssDNA 22bp functionalized circuit

The results and analysis for the ssDNA 22bp functionalized circuit are captured

below using the DRU microfluidics test chamber and the static test unit with follow on

Raman spectroscopy in certain cases to show complimentary binding.

The tests done in the DRU microfluidics test chamber are called out. The

important parameters are the injection time, reaction time and expected reaction window.

The injection time was represented by a red downward pointing arrow and was triggered

when the sensor equilibrates to a 2% response envelope over the course of 100 or more seconds during the real time evaluation of the experiment. The injections and setup attempted to minimize disturbances from electrical and atmospheric influences. The reaction time was represented with an upward pointing red arrow and usually occurs between 120 and 150 seconds after the injection time due to the flow rate, length of tube and DRU chamber size. The reaction window was represented by a change in the sensor response. Note that it does not always return to a near original percent resistance value as sensor drift occurred in a number of tests. The drift can be attributed to the two terminal probe setup. The target DNA used in the microfluidic tests are considered negatively charged entities due to the oxygen on the phosphate backbone.

The *B. anthracis* spore tests were carried out on the functionalized circuits in the open air test units. They are expected to be similar in conductivity to *B. cereus* and 0.02 Mho/m based on work done by Marquis and Carstensen [93].

Table 3 summarizes the input concentrations, slopes and percent change responses for the 22bp sensor versus different aptamers. The figures are broken out in each section according to the target aptamer and ordered from lowest to highest concentration. The slopes are calculated from the starting reaction time and concentration for the first response peak only. Most of the reaction slopes seem to have inversion points in the rise response that would qualify them as second order chemical reactions. However, no attempt was made to characterize these reactions as second order due to the amount of noise in the responses and limited data availability.

Table 3: 22bp circuit versus multiple target DNA aptamers.

ssDNA 22bp sensor response					
Target	Conc. (nM)	Signal Start $(\Delta R/R_0)$%	Slope $((\Delta R/R_0)$%$)$/s	Signal Max $(\Delta R/R_0)$%	Signal Difference
c22bp	1.1	2.332	-0.003700	1.523	-0.809
c22bp	1000	-1.794	-0.015745	-2.09	-0.296
c22bp	1000	-2.254	-0.011300	-2.548	-0.294
c22bp	377	0.52	0.005300	1.473	0.953
c22bp	377	5.543	0.000588	6.373	0.83
39bp	55	0.961	0.014800	7.327	6.366
39bp	167	2.469	0.012400	7.829	5.36
77bp	16	0	0.005650	1	1
77bp	50	-1.024	0.009200	3.042	4.066
77bp	167	3.577	0.036700	18.68	15.103

Table 4 is a summary of the 22bp sensor exposure to *B. anthracis* Sterne strain spores. The tests were static tests as previously discussed.

Table 4: 22bp circuit versus B. anthracis Sterne strain spores.

ssDNA22bp aptamer sensor exposed to *B. anthracis* Sterne strain spores					
Target	Conc. (Spores/L)	Estimated Spores	Start (s)	Stop (s)	Signal Max $(\Delta R/R_0)$%	Slope $(\Delta R/R_0)$%)/s
Spores 1A	735	735	182.5	325.4	0.847	0.0061
Spores 2A	3750	4485	329.7	529.3	1.847	0.0093
Spores 3A	3750	8235	530.1	661.3	4.903	0.0371

4.1.1   ssDNA 22bp versus DI water

The 22bp sensor was tested against double filtered deionized water at the beginning of every run. The response was random up until the point that the response envelope was within 2% of the signal over the course of 100 seconds.

4.1.2 ssDNA 22bp versus complimentary DNA 22bp

Figure 18 shows the ssDNA 22bp sensor exposed to a 300uL of 1.1nM, 22bp complimentary DNA. The reaction occurs at 873 seconds and results in a decrease from 2.332% to 1.523% over the course of 200 seconds. The decrease in resistance suggests that the ssDNA22bp aptamer interacts with the cDNA 22bp in such a way that reduces the overall resistance in the graphene sheet.
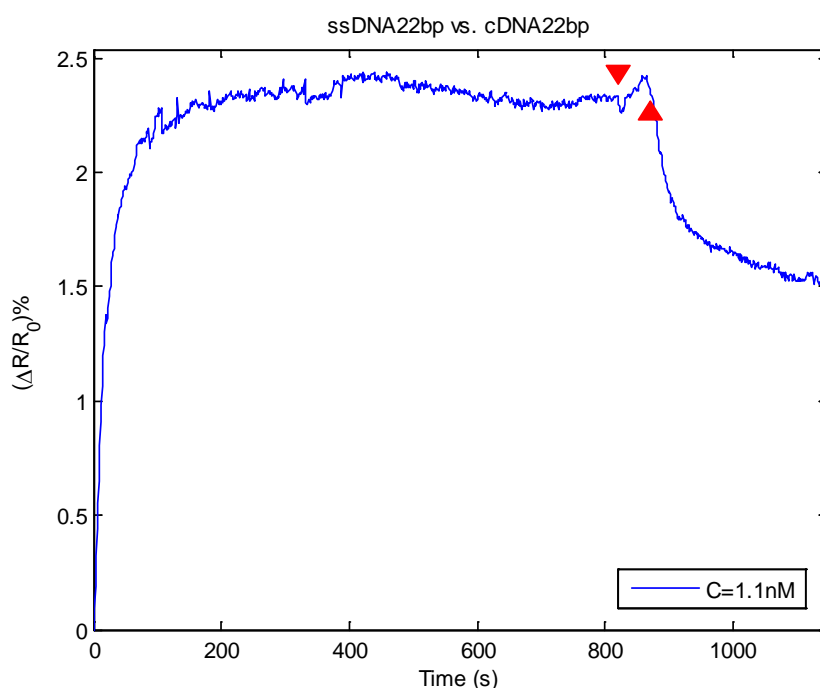

Figure 18: 22bp circuit versus 1.1nM, 22bp target aptamer solution.

Figure 19 shows ssDNA 22bp sensor exposed to 300uL of 377nM, 22bp aptamer of complimentary DNA. The resistance increased by 0.953 % over the course of 178 seconds and then stopped. This event is shown by the half-concave response from 373 seconds to 551 seconds time range. The spikes in the signal between 1000 and 2000 seconds are attributed to people bumping into the setup. The continuing upward trend is

either sensor drift or an ongoing reaction with the ssDNA 22bp on the surface of the sensor. The sensor response increase may be attributed to the cDNA22bp aptamers competing for space on the functionalized surface.
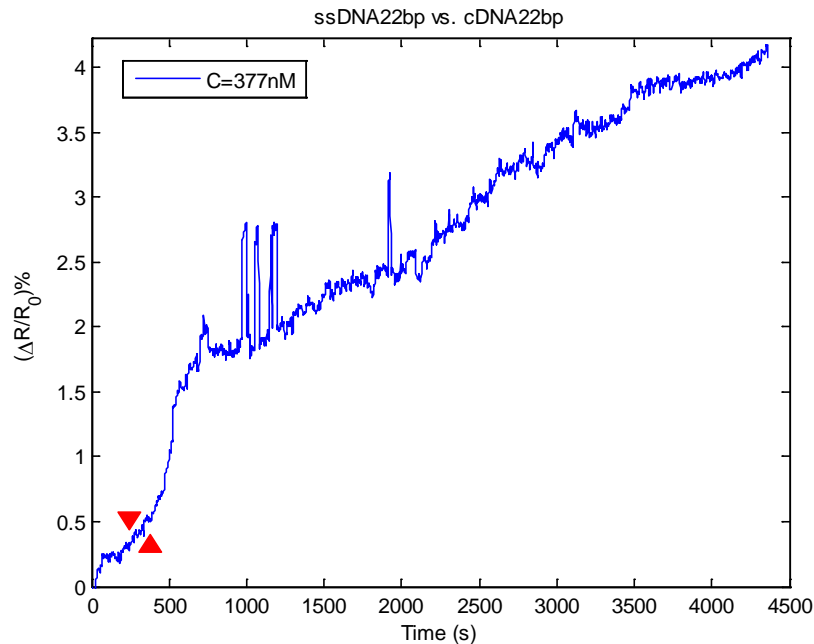

Figure 19: 22bp circuit versus 377nM, 22bp target aptamer solution.

Figure 20 is a continuation of the reaction in Figure 20 to determine if it was possible to overload the sensor. The injection at 5213 seconds is a 300 uL, 377nM concentration of 22bp complimentary DNA. The sensor rises from 5.543% to 6.373% and then drops off abruptly back to the original resistance value. This response may be attributed to either a buildup of cDNA22bp with a subsequent collapse of the electrical resistance as the target concentration of cDNA22bp became too large for the bound 22bp aptamer to handle. Or it could be a triple helix binding state that is possible with this particular target DNA.
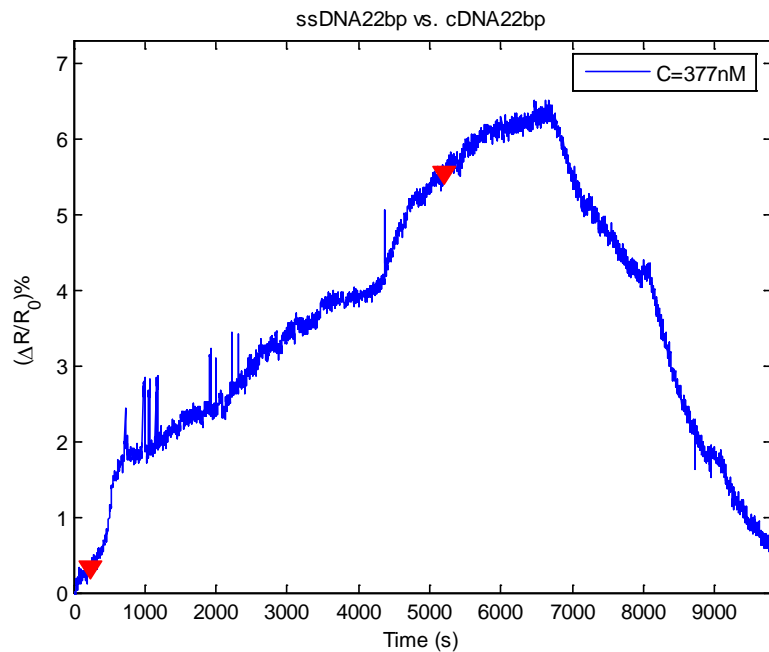
Figure 20: 22bp circuit versus 2X 377nM 22bp target aptamer solutions.

Assuming the ssDNA22bp and cDNA22bp could form a triple helix, the question becomes how this happen? As the concentration of target aptamers increase, they continue to bind with the ssDNA22bp functionalized aptamers on the graphene surface. The system continues to build eventually reach a tipping point where the cDNA continues to recognize its compliment and binds into the already formed ssDNA 22bp-cDNA 22bp and decreases the overall current by driving the double stranded DNA 22bp from an upright position back into the graphene. This makes sense because the additional cDNA 22bp even while bound into the double helix does not have fully shielded hydrogen bonds. There are relative stabilities for base triplets that match the available configurations with the ssDNA 22bp and the cDNA22bp. Figure 21 shows the strongest and most likely base triplets are T*AT with 13 of 22 base pairs forming at the base of the

69

ssDNA22bp-cDNA22bp double helix. The T*AT bonds 13 of 22 base pairs and

respresented with given by blue crosses in Figure 21. The standard Watson-Crick
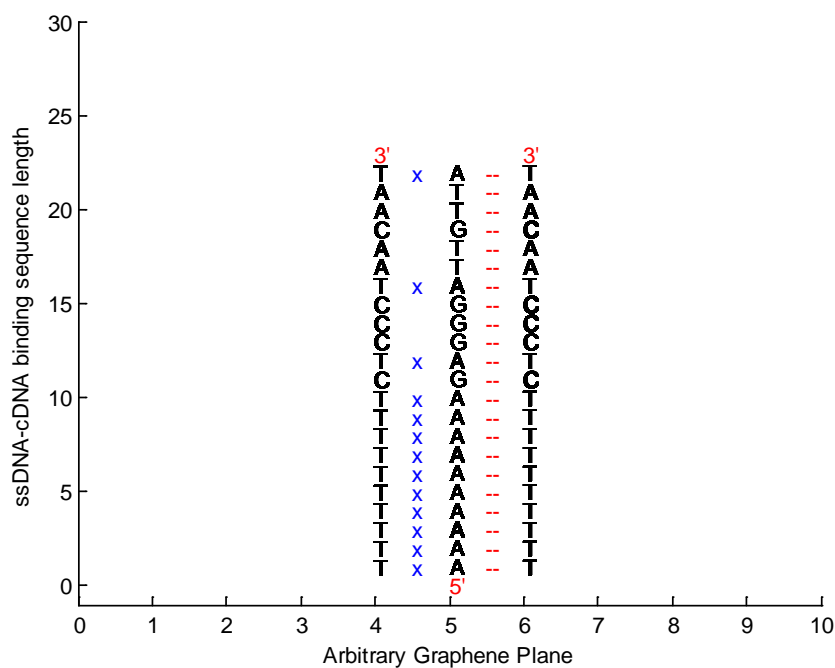
AT/CG bonds given by red dashes[50].

Figure 21: Stable triple helix bond .

Figure 22 shows the second strongest base triplet sequence T*GC with 5 of 22 base pairs

forming at the 11 base pair and continuing up with 3 of 22 base pairs rebinding into

T*AT configuration. The T*GC binding is represented by the green circles between the

cDNA 22bp sequence and the ssDNA 22bp-cDNA22bp sequence. The red dashes

indicate hydrogen bonding for B-DNA Watson-Crick complimentary binding. The blue

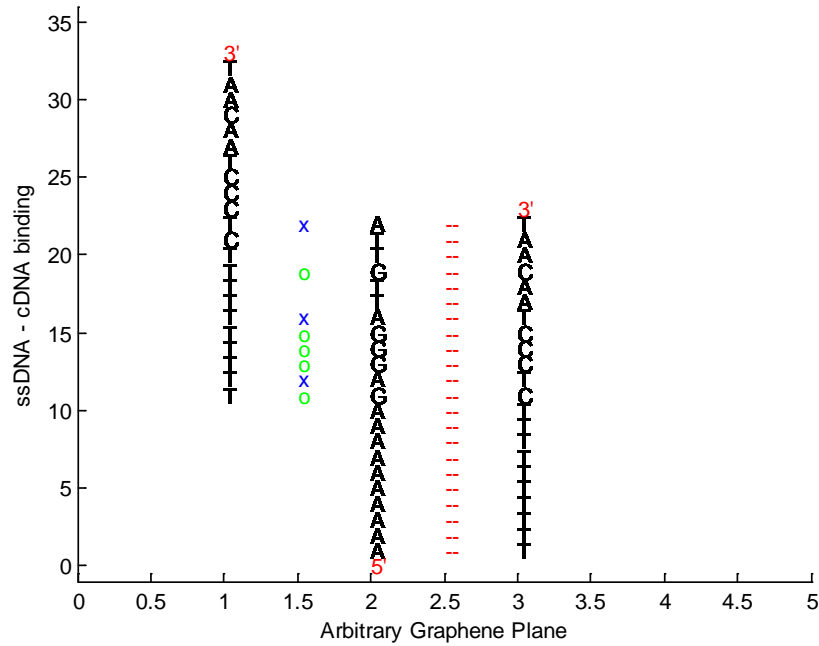crosses indicate the stronger T*AT bond [50].

Figure 22: Second Stable triple helix binding for 22bp aptamers.

Figure 23 shows the introduction of two cDNA injections as the sensor was equlibriating with the DI water in the microfluidics chamber. The injections were 100uL of 1000nM, 22bp cDNA. The injection spacing was over the course of 100 seconds. This test was done to see how the system would react to smaller volumetric dose at a higher concentration. Reviewing the data, one cannot be sure if the small response was due to an inability of the 22bp aptamer on the circuit to bind properly because of the 22bp target aptamer competing for one another or if the number of 22bp target aptamers saturated the circuit. The low response to 1.1 nM, higher response to 377 nM and low response to 1000 nM may indicate a preferential binding concentration. The spikes in the system were from personnel bumping into the side of the setup apparatus.
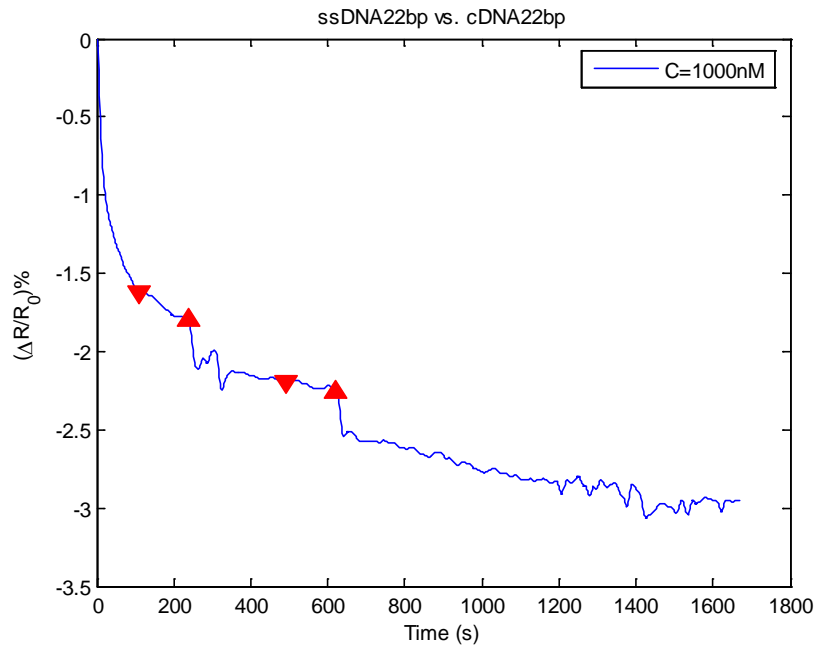
Figure 23: 22bp circuit versus 1000nM, 22bp target aptamer solution.

The response of the 22bp sensor aptamer to the complimentary 22bp target aptamer suggests the complimentary binding occurred in a way that reduced the amount of interfering bonds in the graphene conduction path. This is interesting because it may indicate straight chain behavior based on the length of the DNA chain and the interactions of the ssDNA bp aptamers in response to the cDNA 22bp target aptamer.

4.1.3   ssDNA 22bp versus DNA 39bp

Figure 24 shows the 22bp aptamer sensor exposed to 300uL of 55nM, non-complimentary 39bp target aptamer. The reaction starts at 1754 seconds and rises for 429 seconds. The percent change in resistance is 6.36%.
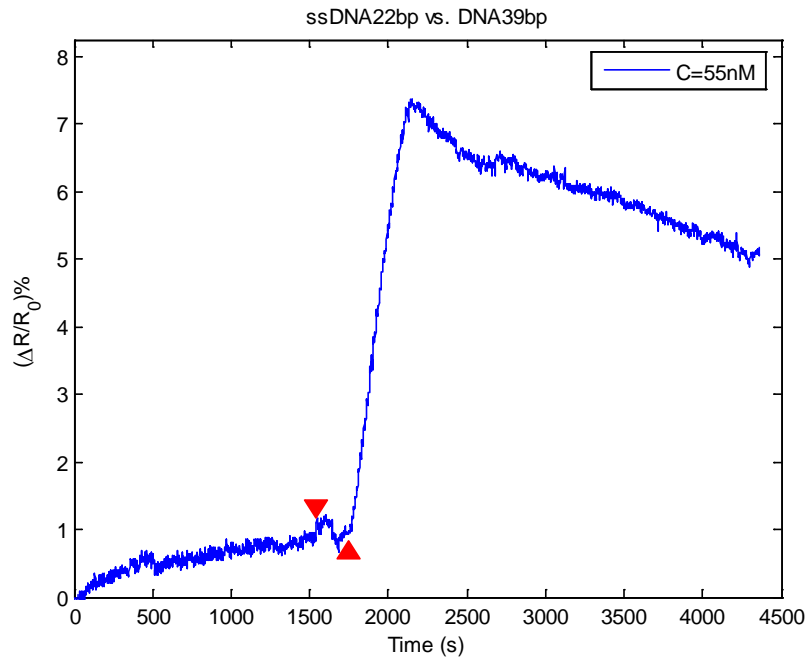
Figure 24: 22bp circuit versus 55nM, 39bp target aptamer solution.

This change in resistance is assumed to be due to the number of available sites that the ssDNA22bp can interact with on the 39bp sequence. There is an analysis performed for the 77bp sequence that was exposed to the 22bp aptamer in section 4.1.4 that provides a potential answer to the question of why the 22bp aptamer responds so well to the 39 bp target aptamer.

Figure 25 shows the 22bp aptamer sensor exposed to 300uL of 167nM, non-complimentary 39bp target aptamer. The reaction starts at 1101 seconds and rises for 434 seconds. The percent change in resistance is 5.36%. This change in resistance is assumed to be due to the number of available sites that the ssDNA22bp can interact with on the 39bp sequence.
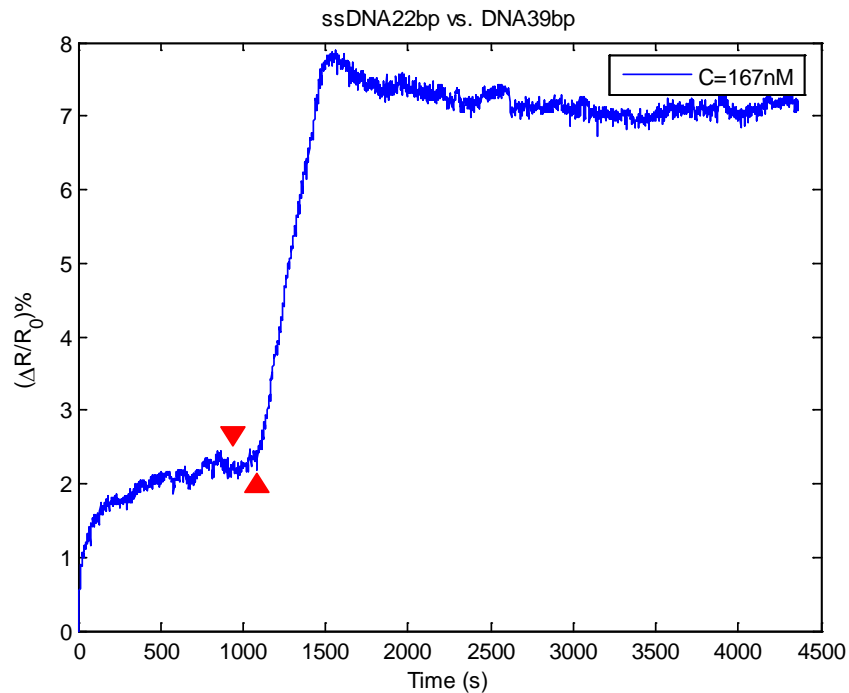
Figure 25: 22bp circuit versus 167nM, 39bp target aptamer solution.

4.1.4 ssDNA 22bp versus DNA 77bp

Figure 26 shows the 22bp aptamer sensor exposed to 300uL of 16.7nM, noncomplimentary 77bp target aptamer. The reaction starts at 2830 seconds and rises for 1000 seconds. The percent change in resistance of the rise is approximately 1.0% and it excludes the information above the 1% response. Even though the data above the 1% is useful, there was concern the remaining information would be incorrect due to the remaining spikes from personnel bumping into the setup.

Figure 26: 22bp circuit versus 16.7nM, 77bp target aptamer solution.
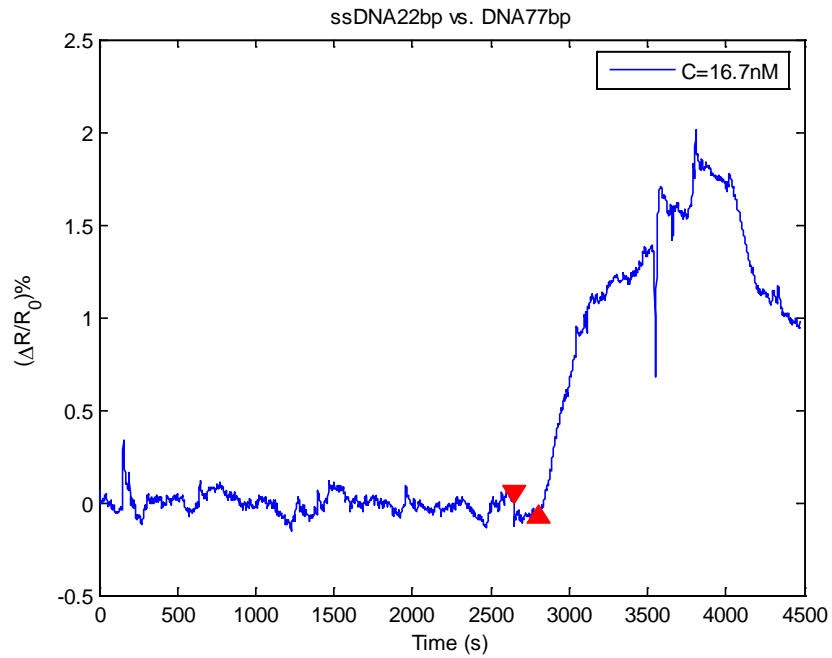
The response was assumed to be due to the low concentration of the 77bp target

aptamer.

Figure 27 shows the 22bp aptamer sensor exposed to 300uL of 50nM, non-

complimentary 77bp target aptamer. The reaction starts at 570 seconds and rises for 445

seconds. The percent change in resistance is approximately 4.0%.

Figure 27: 22bp circuit versus 50nM, 77bp target aptamer solution.

The 22bp sensor response to the 50nM concentration is approximately 2X larger than the response to 16.7nM concentration. This may be due to the increase in available interaction sites based on the overall concentration of the 77bp aptamer.

Figure 28 shows the 22bp aptamer sensor exposed to 300uL of 167nM, non-complimentary 77bp target aptamer. The reaction starts at 1283 seconds and rises for 411 seconds. The percent change in resistance is approximately 15%.
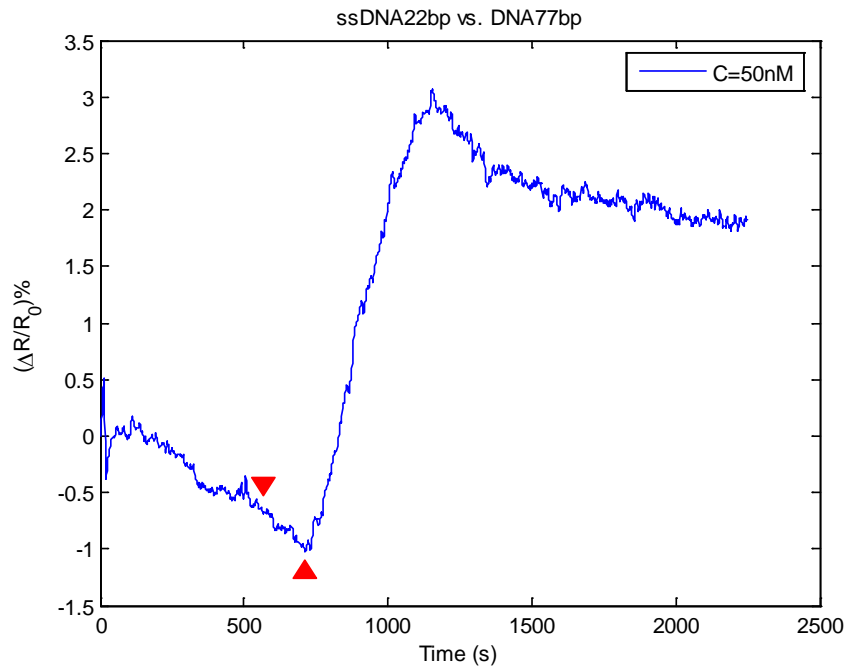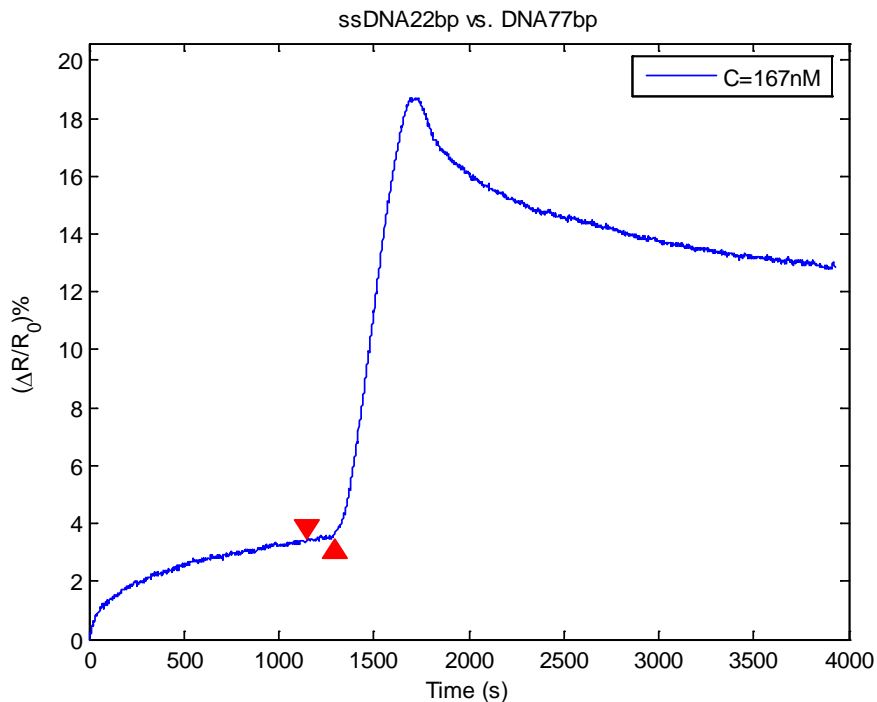
Figure 28: 22bp circuit versus 167nM 77bp target aptamer solution.

The response of the 22bp aptamer sensor was approximately 10X the response to the 1.67nM concentration and may be solely due to the concentration increase.

The response of the 22bp aptamer sensor to the cDNA 22bp aptamer seems odd since complimentary binding is expected to produce a much larger response than the 39 bp and 77bp aptamers. This issue was explored with the help of the OligoAnalyzer 3.1 toolkit[56]. The 22bp aptamer was entered into the system at a 1.1nM concentration and matched against the heterodimer configuration for the 22bp target aptamer, and the 77bp target aptamer at 0.01 Mg^{2+} salt concentration with the temperature set to T = 25 °C. The idea was to determine where the 22bp aptamer and 77bp aptamer had the capability to form heterodimers.

The theoretical results showed the 22bp functionalized aptamer versus the 77bp target aptamer had a higher Gibbs free energy (-7.3kcal/mole for a 5bp match) than the 22bp functionalized aptamer with the cDNA22bp target aptamer sequence (-39.61kcal/mole for a full 22bp match). Figure 29 shows the Gibbs Free energy plotted against the available base pairs. It seems reasonable that the 22bp functionalized aptamer would have a very strong attraction to the cDNA 22bp aptamer. Unfortunately, the 22bp functionalized aptamer is secured on the 5' end which excludes many of the available sites for most of the cDNA22bp target aptamer binding configurations. This particular analysis was carried out only for the 22bp functionalized aptamer because of the odd result when the sensor was exposed to the 77bp target aptamer. The analysis can be extended to the 39bp sequence due to the fact that it consists of the last half of the 77bp sequence.
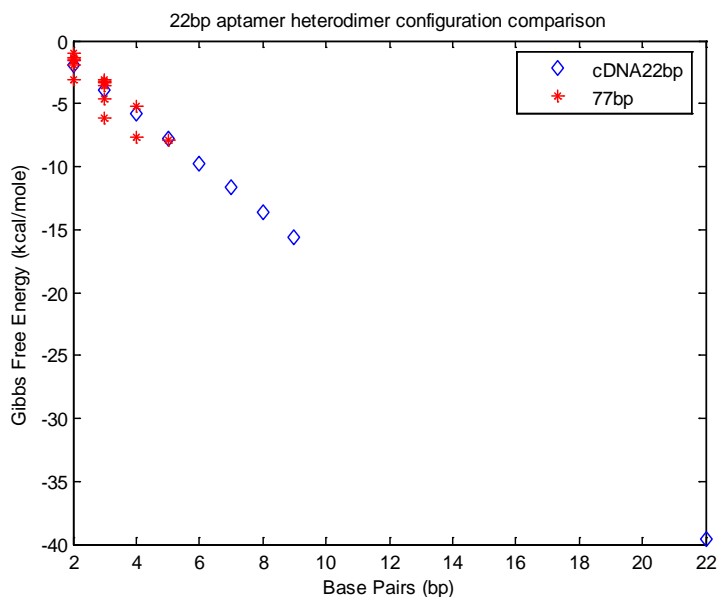

Figure 29: Gibbs Free Energy availability for heterodimer binding on the 22bp functionalized aptamer.

4.1.5 ssDNA22bp versus DNA summary

The 22bp aptamer functionalized sensor performed as expected against the complimentary 22bp target aptamer. It did not perform as expected against the 39bp or 77bp aptamer due to what is thought to be conformal binding capabilities of the 39bp and 77bp sequences to the linear 22bp aptamer. Further study should be performed to verify if this is really the case.

4.1.6 ssDNA 22bp versus *B. anthracis* Sterne strain spores

The ssDNA22bp sensor was exposed to *B. anthracis* Sterne strain spores in DI water in a static test configuration as shown in Figure 30. The ssDNA22bp showed a change in response after introducing 1uL of a 7.35×10^{8} spores/L concentration. This equates to approximately 735 *B. anthracis* spores in 1 µL of DI water. The next two injections were 5 µL drops at 3750 spores/L. The percent change in resistance increased 0.847% for the first injection, 1.847% for the second injection and 4.903% for the third injection.
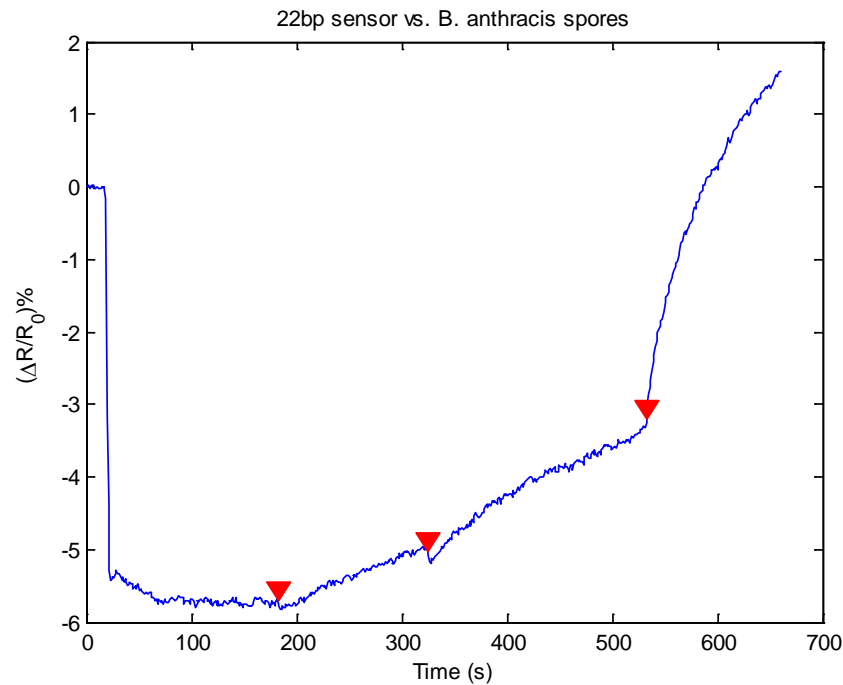
Figure 30: 22bp circuit versus multiple exposures of *B. anthracis* spores.

This response is useful because it shows that something happens almost right away. The 22bp aptamer should only be detecting the *B. anthracis* spores because the circuit already adjusted to the introduction of water. Note that the sensor resistance should increase as spores interact with the 22bp aptamer and interfere with the 22bp aptamer-graphene electrical path. This trend increases with the addition of a 5 µL concentration of approximately 3750 spores at 315 seconds and the addition of a 5 µL concentration of approximately 3750 spores at 520 seconds.

Figure 31 shows the increase in percent resistance change versus spore concentration instead of time. Keep in mind, the spore concentration is associated with the concentrated drop that hit the surface, the 22bp aptamer may not have detected all 735

spores, it may have only interacted with a handful, meaning the sensor sensitivity might be better than previously thought.
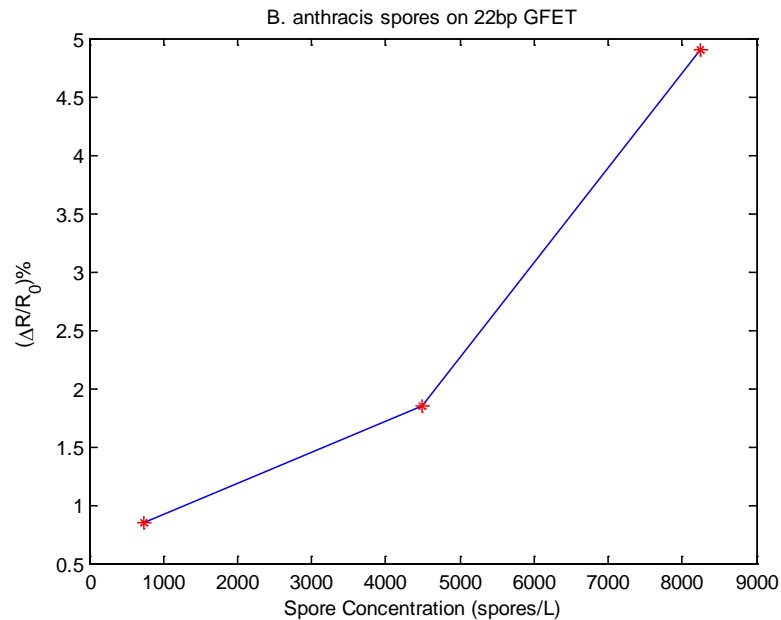
Figure 31: 22bp circuit versus *B. anthracis* spores.

The electrical current-time plot curves obtained with the Dolomite microfluidics chamber were similar to research that has been published by Mohanty and Berry [13]. They used a graphene oxide coated with an aminated ssDNA and then sealed the surface with an ethanolamine in a nitrogen environment. Mohanty and Berry's setup detected live and dead single cell gram negative Geobacter and gram positive Bacillus cereus.

The ssDNA22bp aptamer sensor that was exposed to *B. anthracis* spores was transferred to the AFM lab for binding verification. The face of the circuit was stuck to the bottom surface of the top lid of the Petri dish when it arrived. The circuit was pried

off the petri dish and sonicated for 5 minutes and placed into the AFM. Figure 32 indicates the regions that were imaged with the blue dashed lines around the area. The AFM data showed a relatively flat surface with 500 nm structures that resemble smashed *B. anthracis* spores. Remember *B. anthracis* spores are approximately 2.0 µm in diameter and the graphene functionalized circuit area is hedged on two sides by 100 nm (30 nm Cr/70 nm Au) electrodes.
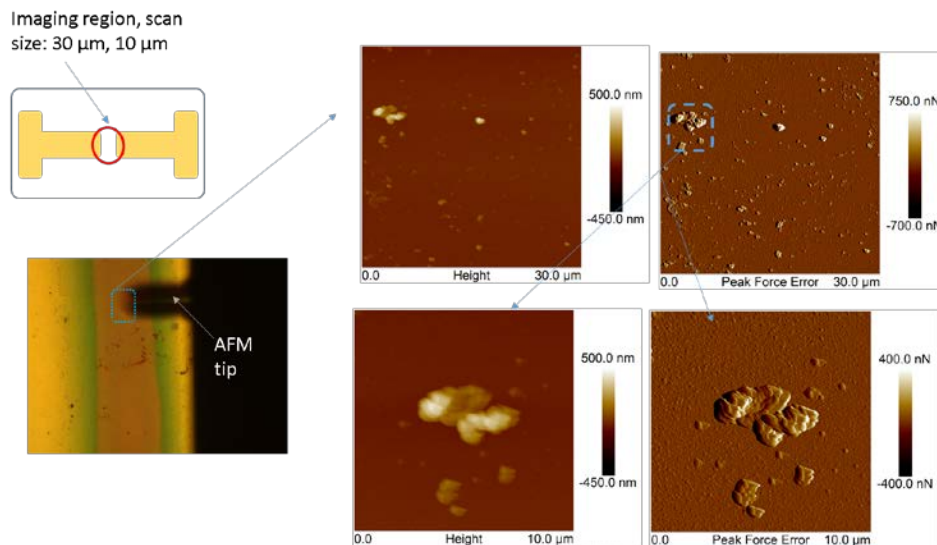
Figure 32: AFM image of 22bp aptamer functionalized circuit. The 500 nm structures are most likely damaged B. athracis spores.

The AFM tip was moved to spot #1 in Figure 33 to and a separate section of the functionalized area was explored. This time spot #1 had flakes on the surface of the Au probe. These flakes are probably due to the refunctionalization of the graphene circuit by thermally transferring a new layer of graphene onto the circuit and annealing it after the original circuit failed from use.
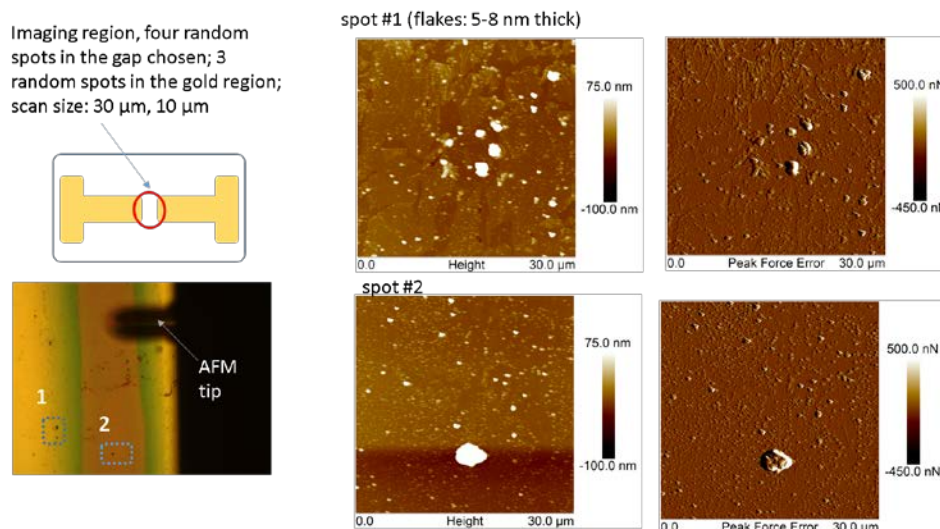
Figure 33: AFM picture shows minimal surface features for ssDNA 22bp aptamer exposed to B. anthracis spores.

The second spot area in Figure 33, resembles the thrombin aptamer (3 nm long) modified graphene channel shown in Ohno [33]. The direct verification of 22bp aptamers on the surface cannot be confirmed with the current AFM data due to the reported heights.

4.2   Results and Analysis for ssDNA 77bp functionalized circuit

The results and analysis for the ssDNA 77bp functionalized circuit are similar to the ssDNA22bp circuit above with the exception that the 77bp aptamer was also tested in a static configuration to mimic a real sensor. The injection time, reaction time and expected reaction windows are triggered with respect to the 2% signal envelope over the course of 100 or more seconds during the real time evaluation of the experiment. The injections and setup were done as carefully as possible to minimize extraneous influences. The target DNA used in the microfluidic tests are considered negatively charged entities due to the oxygen on the phosphate backbone. The spores are expected

to be similar to *B. cereus* and have an expected conductivity of 0.02 Mho/m based on work done by Marquis and Carstensen [91].

The 77bp sensor responses versus the target aptamers are shown in Table 5. The information contained focuses on the first response peak only. The slopes are calculated from the starting reaction time and concentration for the first response peak. Most of the reaction slopes seem to have inversion points in the rise response that would qualify them as second order chemical reactions. However, no attempt was made to characterize these reactions as second order due to the amount of noise in the responses and limited data availability.

Table 5: 77bp circuit versus multiple target aptamers.

ssDNA 77bp sensor response					
Target	Conc. (nM)	Signal Start $(\Delta R/R_0)\%$	Slope $((\Delta R/R_0)\%)/s$	Signal Max $(\Delta R/R_0)\%$	Signal Difference
18bp	1.85	-0.03123	-0.00036	-0.07229	-0.04106
18bp	56	0.02	0.0000498	0.12	0.1
18bp	167	2.564	-0.0023	2.299	-0.265
22bp	1.1	1.179	0.006	1.508	0.329
22bp	55	-11.2	-0.0052	-13.4	-2.2
22bp	111	0.0185	0.0075	0.4851	0.4666
22bp	337	-12.67	-0.0108	-14.95	-2.28
22bp	452	3.551	-0.0015	3.282	-0.269
c39bp	167	-0.6279	0.0018	-0.4922	0.1357
c39bp	167	6.773	0.007	7.234	0.461
c39bp	55	5.58	0.0012	5.859	0.279
c77bp	5	0	0	0	0
c77bp	50	1.19	0.0113	6.576	5.386
c77bp	50	2.633	0.0135	9.016	6.383

Table 6 is a summarization of the 77bp aptamer response to the *B. anthracis* exposure.

Table 6: 77bp circuit versus *B. anthracis* Sterne strain spores

ssDNA77bp sensor versus *B. anthracis* Sterne strain spores						
Target	Conc. (Spores/L)	Estimated Spores	Start (s)	Stop (s)	Signal Max $(\Delta R/R_0)\%$	Slope $((\Delta R/R_0)\%)/s$
Spores A	7350	7350	100	520	0.75	
Spores B	7350	14700	522	1000	0.7	
Spores 1A	735	735	355.9	359.2	2.89	0.8455
Spores 2A	3750	4485	663.4	675.4	7.03	-0.58
Spores 3A	3750	8235	1000	1015	12.67	-0.8447

4.2.1   ssDNA 77bp versus DI water

The 77bp sensor was tested against double filtered deionized water at the beginning of every run. The response was random up until the point that the response envelope was within 2% of the signal over the course of 100 seconds. Once this point was reached the test was executed.

4.2.2   ssDNA 77bp versus degenerate DNA 18bp

Figure 34 shows the 77bp sensor exposed to 300 uL, 1.85nM degenerate 18bp target aptamer. The reaction time started at 1030 seconds. The percent resistance decrease is approximately 0.03%. The small concentration size and the random sequence variation associated with the degenerate 18bp DNA are considered factors as to why there was minimal response by the ssDNA77bp.

Figure 34: 77bp circuit versus 1.85nM, 18bp target aptamer solution.

The 77bp aptamer sensor response to the degenerate 18bp target probe concentration was
not significant enough to produce a useable response.

Figure 35 shows the ssDNA77bp aptamer response upon introduction of 300 μL,
55.6 nM, non-complimentary 18bp degenerate DNA. The response envelope did not
exceed 2% during the reaction window. The signal did however deviate slightly from the
mean resistance resulting in a resistance increase. It is assumed the resulting change
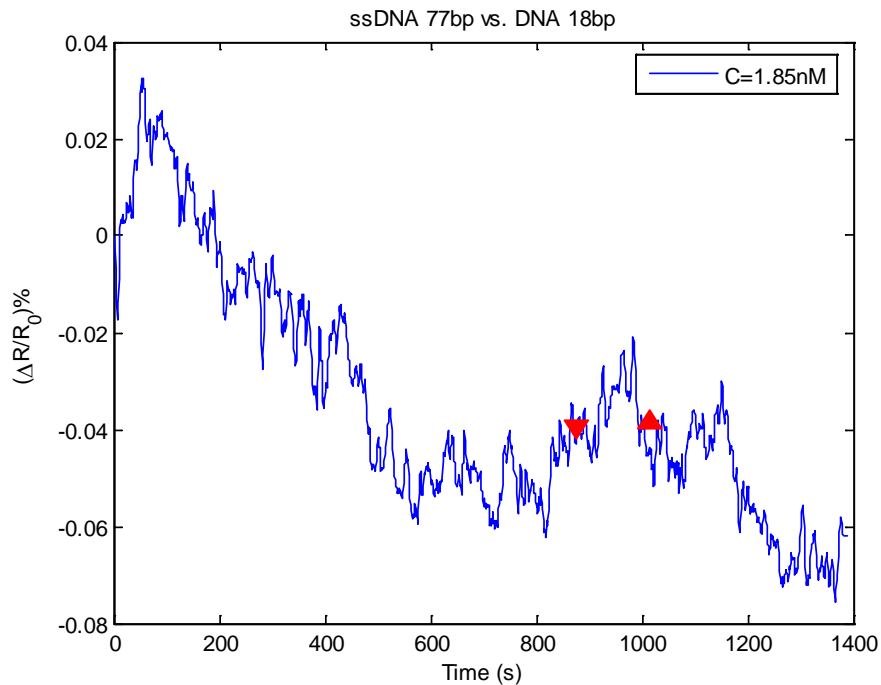signal was due to sensor drift from the continued introduction of DI water.

Figure 35: 77bp circuit versus 56nM 18bp target aptamer solution.

The 77bp aptamer sensor response to the degenerate 18bp target probe concentration was not significant enough to produce a useable response.

Figure 36 shows the ssDNA77bp aptamer sensor exposed to 300 µL of 167 nM, non-complimentary 18bp degenerate DNA. The reaction starts at 1150 seconds and decreases for 107 seconds. The percent change in resistance is approximately -0.265%.
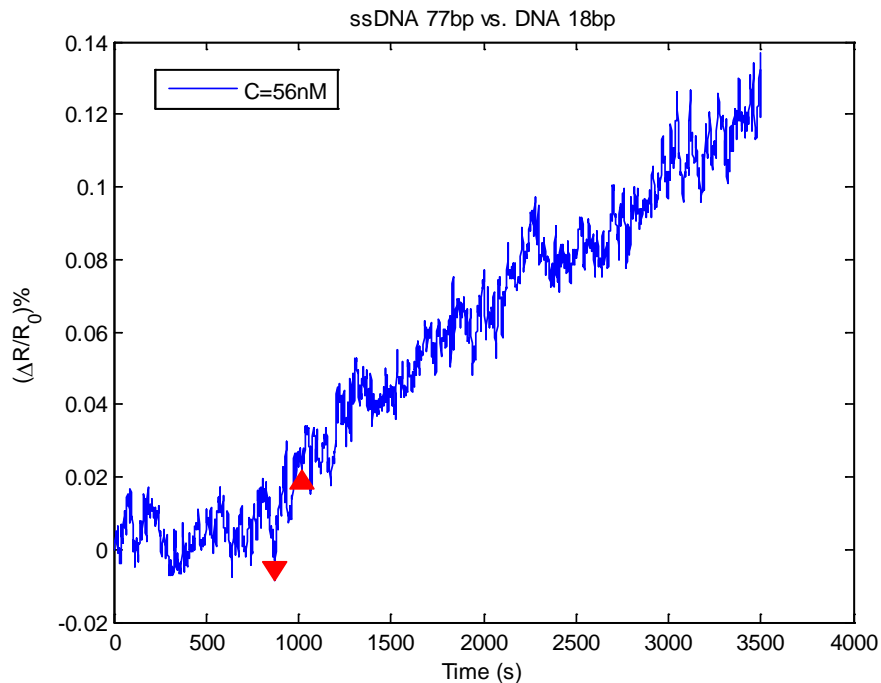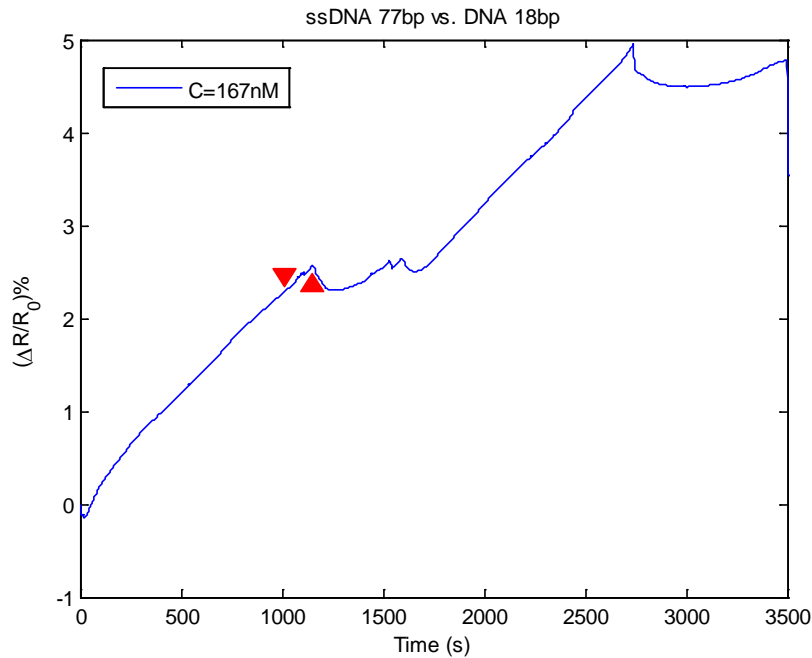
Figure 36: 77bp circuit versus 167nM 18bp target aptamer.

The 77bp aptamer sensor response to the degenerate 18bp target probe concentration was not significant enough to produce a useable response. These results show that the 77bp aptamer sensor is relatively insensitive to non-complimentary DNA binding.

4.2.3   ssDNA 77bp versus DNA 22bp

Figure 37 shows the ssDNA77bp aptamer sensor exposed to 300 µL of 55 nM, non-complimentary 22bp target aptamer. The reaction starts at 1338 seconds and decreases for 385 seconds. The percent change in resistance is approximately -2.2%. The second target was 300 µL of 337 nM, non-complimentary 22bp target aptamer. The reaction starts at 2242 seconds and decreases for 211 seconds. The percent change in resistance is approximately -2.28%.
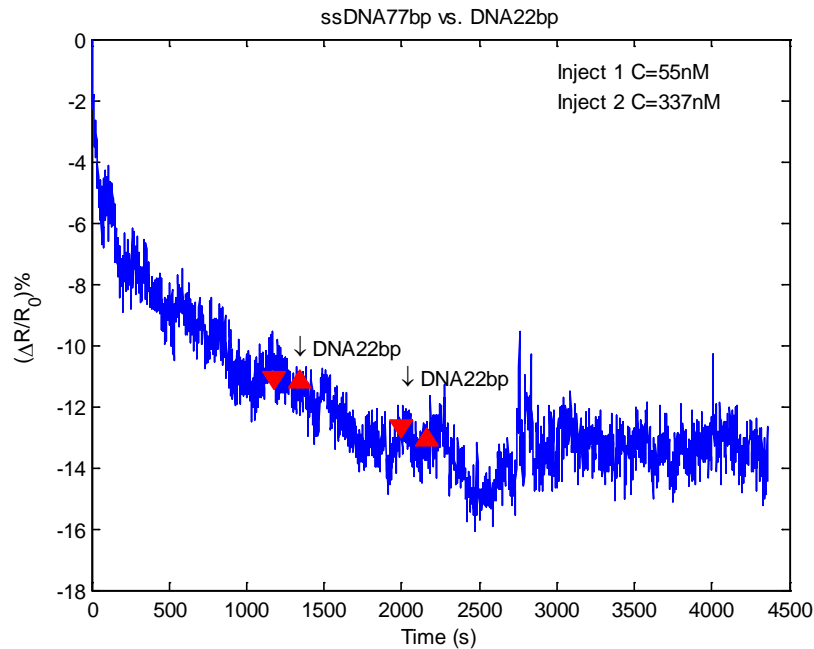
Figure 37: 77bp circuit versus 55nM and 337nM 22bp target aptamers.

The change in resistance is due to the converse ability of a 22bp target aptamer to attach to a 77bp functionalized surface aptamer. The signal response isn't as big because the 22bp aptamer is linear in solution and would have a hard time binding to the three dimensional 77bp sequence. Similar changes in resistance were found when the ssDNA77bp circuit was exposed to 1.1nM and 111nM concentrations of 22bp non-complimentary target aptamers.

Figure 38 shows the 77bp functionalized circuit exposed to a 300uL, 1.1nM, non-complimentary 22bp target aptamer. The reaction started at 1550 seconds and induces a percent resistance change of 0.4% for approximately 667seconds. The second exposure of 300uL, 111nM, non-complimentary 22bp target aptamer had a reaction that started at 3000 seconds and induced percent resistance change of 0.54% for approximately 650 seconds.

Figure 38: 77bp circuit against 1.1nM and 111nM 22bp aptamer solution.

The 77bp aptamer sensor had a mean 0.47% response to the 22bp non-complimentary

target aptamer.

Figure 39 shows the ssDNA77bp aptamer sensor exposed to 300 µL of 452 nM,

non-complimentary 22bp target aptamer. The reaction starts at 100 seconds at 3.551%

and decreases to 3.282% at 1347 seconds. The percent change in resistance is
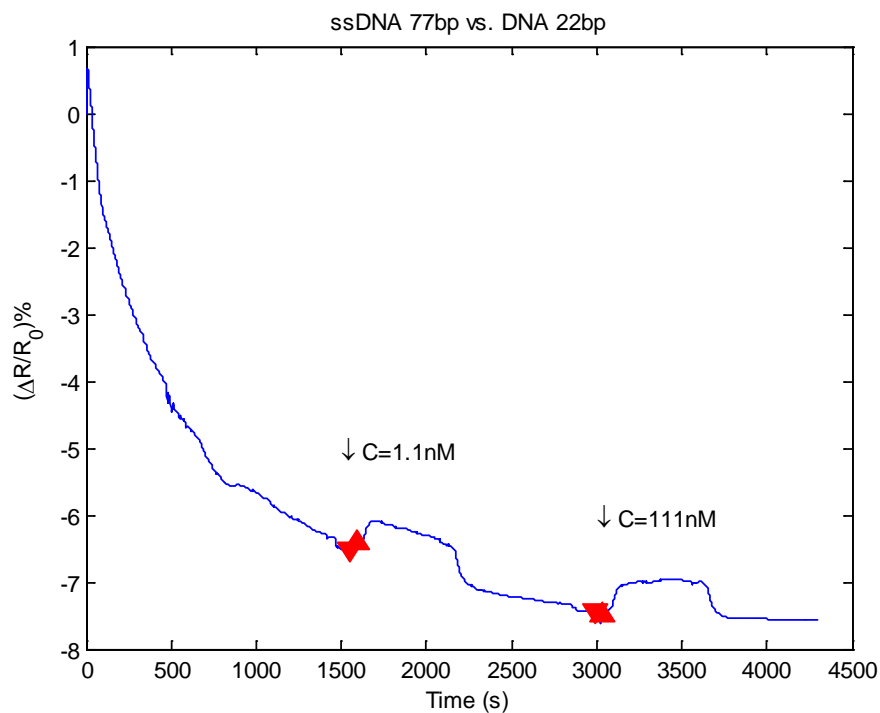
approximately 0.27%.
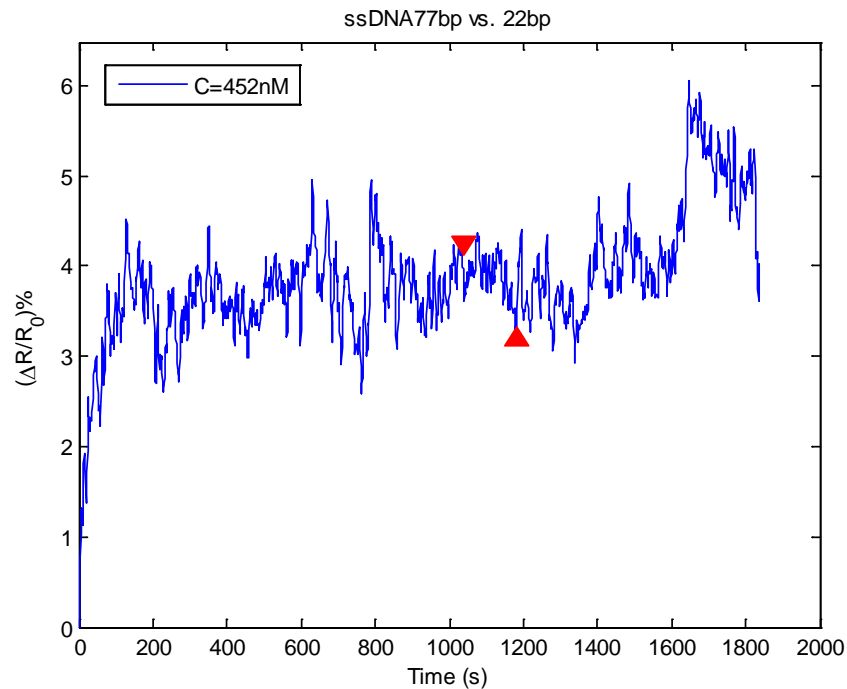
Figure 39: 77bp circuit versus 452nM, 22bp target aptamer solution.

The percent changes in resistance of the 77bp aptamer sensor versus the 22bp non-complimentary aptamer for the various configurations suggests that there may be certain concentrations of 22bp aptamer that allow for better binding than others due to less target aptamer competition.

4.2.4   ssDNA 77bp versus complimentary DNA 39bp

ssDNA 77bp was exposed to a 39bp complimentary half strand to determine the effect it would have on the recognition sequence of the 77bp. The data suggests that the 77bp sequence treats the 39 bp sequence much like the 22bp sequence.

The following data is from a sensor that used a direct graphene to gold thermal tape deposition. Unfortunately, the ssDNA77bp sensor had minimal responses to cDNA39bp in the following 300uL concentrations, 1.1nM, 55.6nM and 167nM.

91

Figure 40 shows the 77bp aptamer sensor exposed to 300uL of 55nM, complimentary one-half 39bp target aptamer and a 300uL, 167nM, complimentary one-half 39bp target aptamer. The first reaction starts at 1640 seconds and induces a percent change in resistance of approximately 0.4% for 667 seconds. The second reaction starts at 2630 seconds and induces a resistance change of approximately 0.54% for 650 seconds.
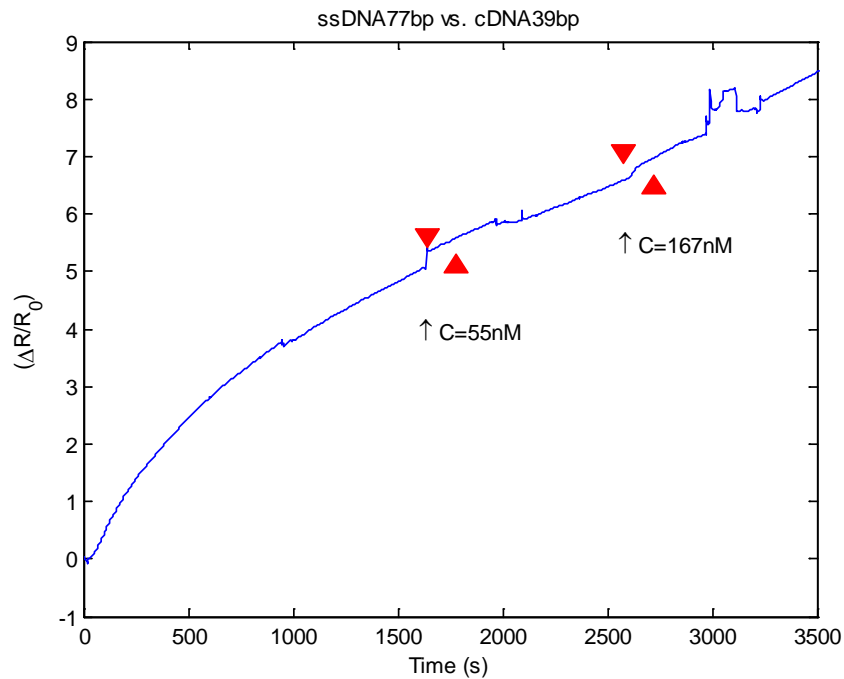
Figure 40: 77bp circuit versus 55nM and 167nM 39bp target aptamer solution.

The response for this particular sensor was startling weak. There were two issues noted on this particular sensor. It had been refunctionalized (which means the graphene was placed on top of the Au/Cr electrodes) which may have reduced its response

capability in solution. Or the fluorophores on the end of the 39bp target aptamer interfered with bonding to the surface aptamers.

Figure 41 shows the 77bp aptamer sensor exposed to 300uL of 167nM, complimentary one-half 39bp target aptamer. The reaction starts at 1135 seconds and rises from -0.629% to -0.4922% in less than 100 seconds and remains there for 639 seconds. The percent change in resistance is approximately 0.14%.
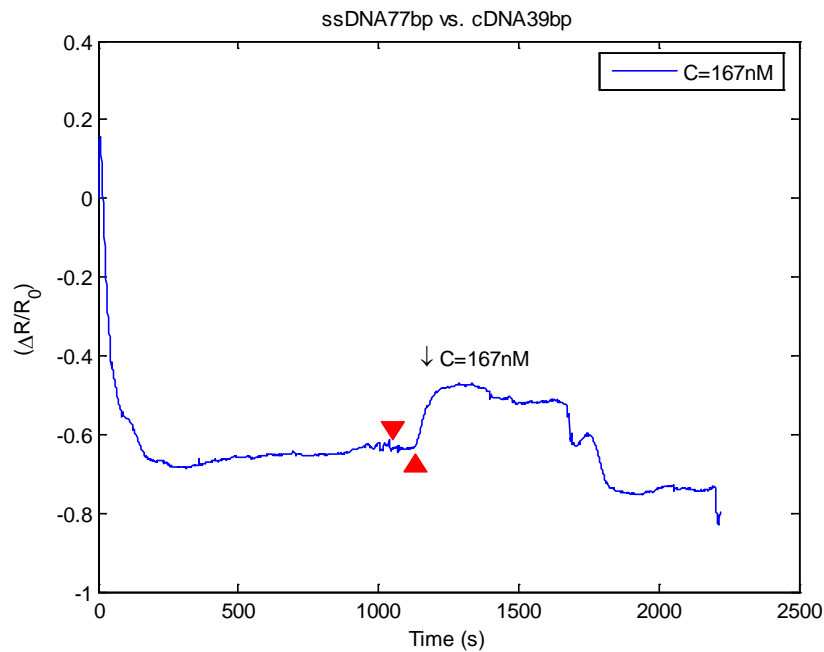
Figure 41: 77bp circuit versus 167nM 39bp target aptamer solution.

The change in magnitude was similar to Figure 40, which suggest that either the 39bp target aptamer has trouble binding to the ssDNA77bp functionalized aptamer or the refunctionalization of the circuit did not work as intended.

4.2.5   ssDNA 77bp versus complimentary DNA 77bp

Figure 42 shows the 77bp aptamer sensor response to a 300uL, 5.0 nM, complimentary 77bp target aptamer. The reaction starts at 1310 seconds. It does not look like there is a significant change in the rise of the overall signal. In this particular case, the response may be more than zero but it is hard to tell given the upward sensor drift and the lack of slope response seen in higher concentrations of target aptamers.
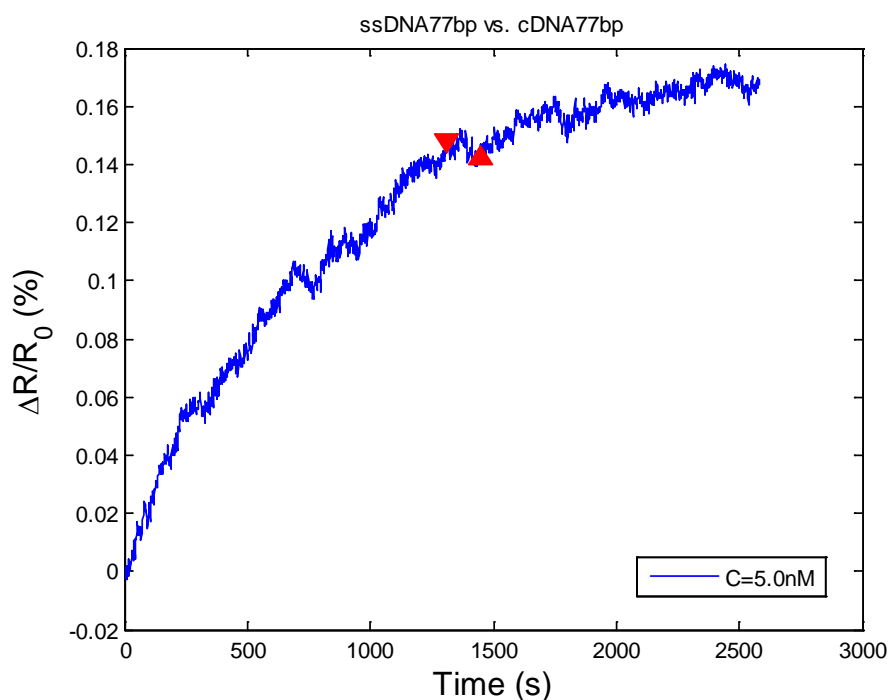
Figure 42: 77bp circuit versus 5.0nM 77bp target aptamer solution.

Figure 43 shows the 77bp aptamer sensor response to a 300uL, 50nM, complimentary 77bp target aptamer. The reaction starts at 1111 seconds and peaks at 1587 seconds with a resistance change of 5.38%.

94
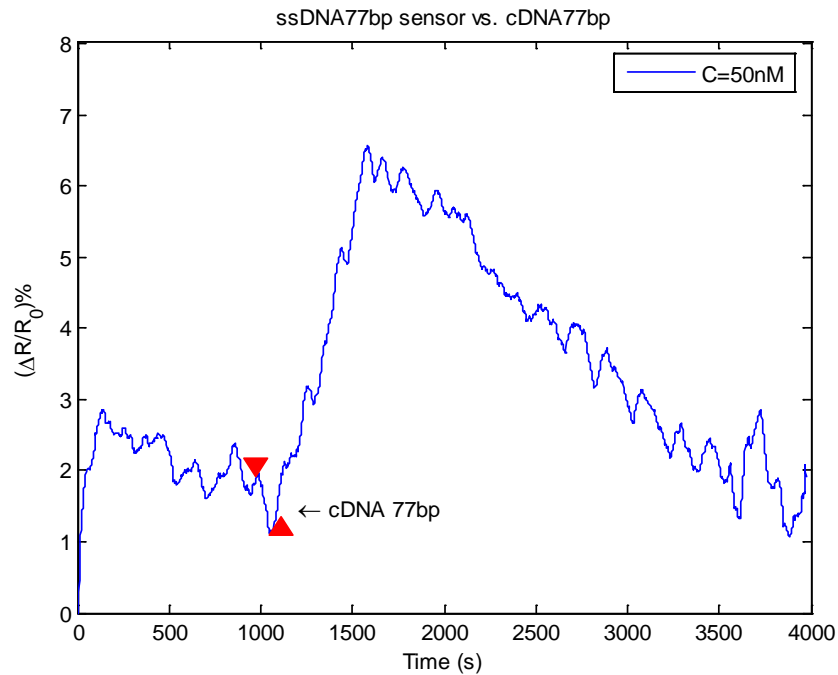
Figure 43: 77bp circuit versus 50nM 77bp target aptamer solution.

The change in resistance profile is markedly different than the previous exposure profiles. The circuit fell from 6.576% to a near initial resistance state at 1.22% after 2313 seconds. The extended tail may be indicative of a slow complimentary de-binding process from the 77bp aptamers.

Figure 44 shows a ssDNA77bp functionalized aptamer response to 300uL, 50nM, complimentary 77bp target aptamer. The circuit stabilized at 500 seconds with injection point at 520 seconds. The resistance increased from 2% to a maximum of 9% at 1132 seconds.
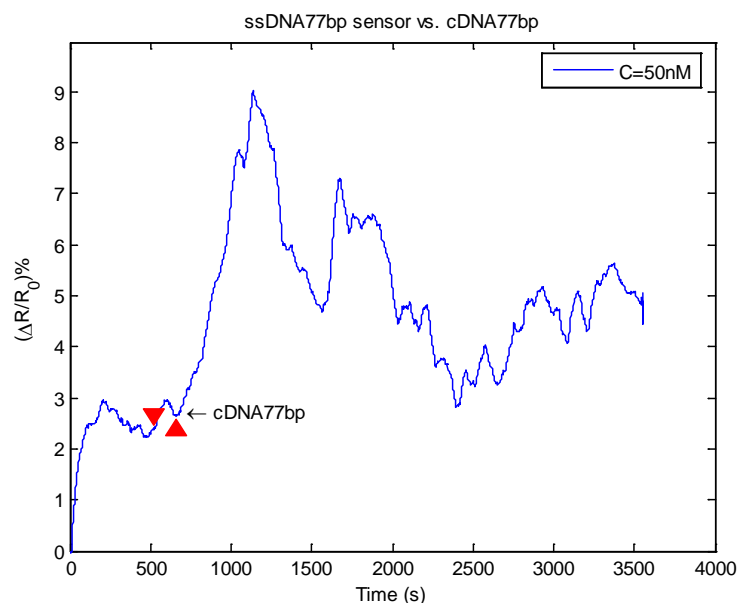
Figure 44: 77bp circuit versus 50nM 77bp target aptamer solution.

The circuit response fell from 9 % to approximately 2.9% after 1254 seconds. The tail drifted up to about 4% and seemed to stay there. The behavior of the extended tail may be indicative of a slow complimentary de-binding process from the 77bp aptamers. The upward drift should be explored as it was not expected.

The 77bp functionalized circuit had Raman spectroscopy performed before it was exposed to the complimentary 77bp target aptamer and after it was examined with an AFM. Figure 45 shows the Raman spectra from 600 cm^{-1} to 4000 cm^{-1} of the 77bp aptamer before it is imaged with the AFM. The 77bp aptamer Raman response is similar to Figure 15 as previously discussed. The major difference is the larger hump associated with the ssDNA77bp + cDNA77bp line. This is indicative of fluorescence and it is partially due to the natural fluorescence of DNA and partially due to the Texas-Red fluorophore attached to the cDNA 77bp target aptamer.
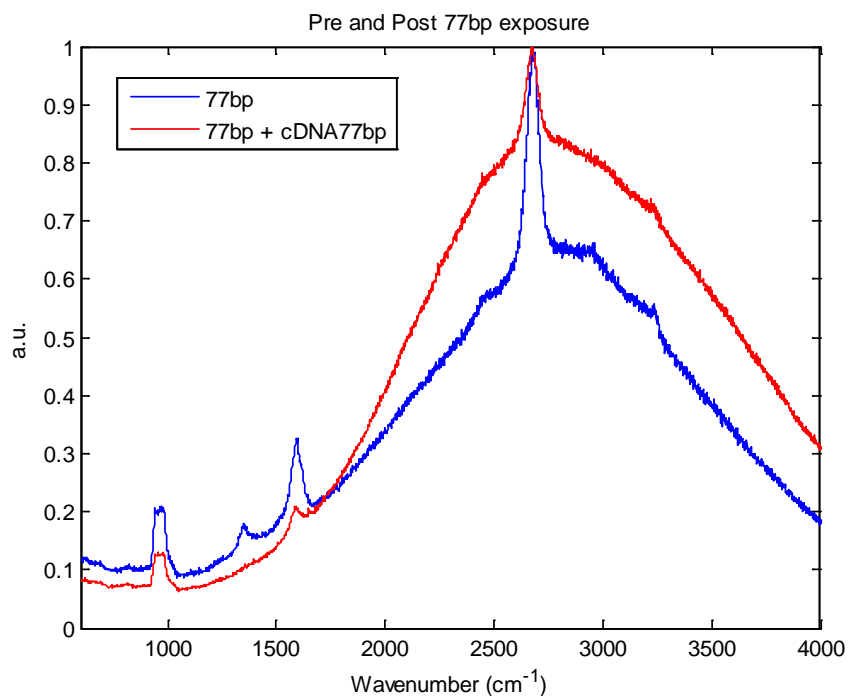
Figure 45: 77bp aptamer functionalized circuit pre and post 77bp complimentary target aptamer exposure.

The AFM results for the 77bp circuit versus the 77bp target aptamer are shown in Figure 46. The circuit was lightly rinsed with DI water to remove remaining 77bp target aptamers. It was sonicated for 5 minutes and then allowed to dry in order to reduce forces on the AFM. The concentration of 77bp target aptamer was 5.0 µM. The structures shown in Figure 46 are interesting in that they resemble three-dimensional spherical forms that could be associated with the binding of the 77bp aptamer to the cDNA 77bp target aptamer. All we have at this point is indirect evidence provided by the previous Raman spectrum in Figure 45.
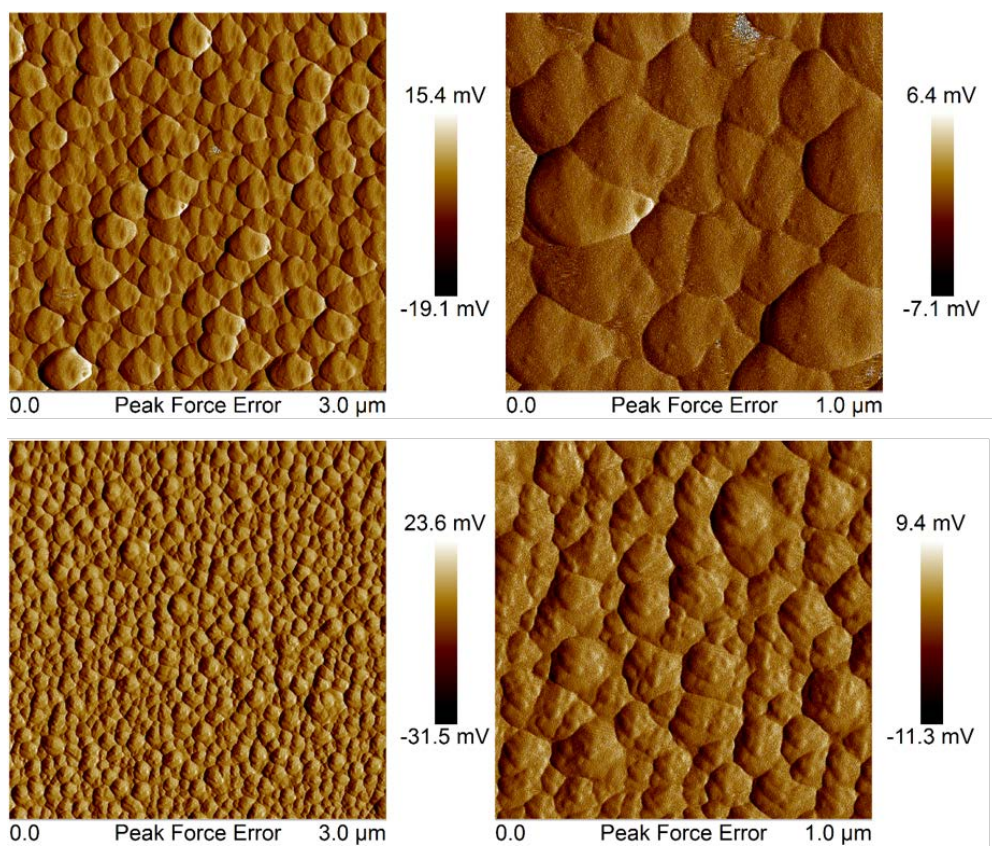
Figure 46: 77bp aptamer exposed to complimentary 77bp target aptamer under AFM. The top right inset is a magnification of the top left.

The lack of clearly defined DNA might lead one to speculate, why can other researchers see DNA on their devices and yet we cannot. Many researchers use DNA measured in kilobases to perform their research. The aptamers used in this research were approximately 6 nm to 30 nm and 22 to 77 base pairs in length.

4.2.6 ssDNA 77bp Aptamer Static Responses

The static responses inject points are indicated with red arrows. Figure 47 shows a 77bp functionalized graphene circuit exposed to multiple target DNA over a 2.5 hour time period. The interesting point to note is that the characteristics associated with the

slope of the rise times associated with the target DNA. The complimentary sequences have lengths between 6 and 30 nm.
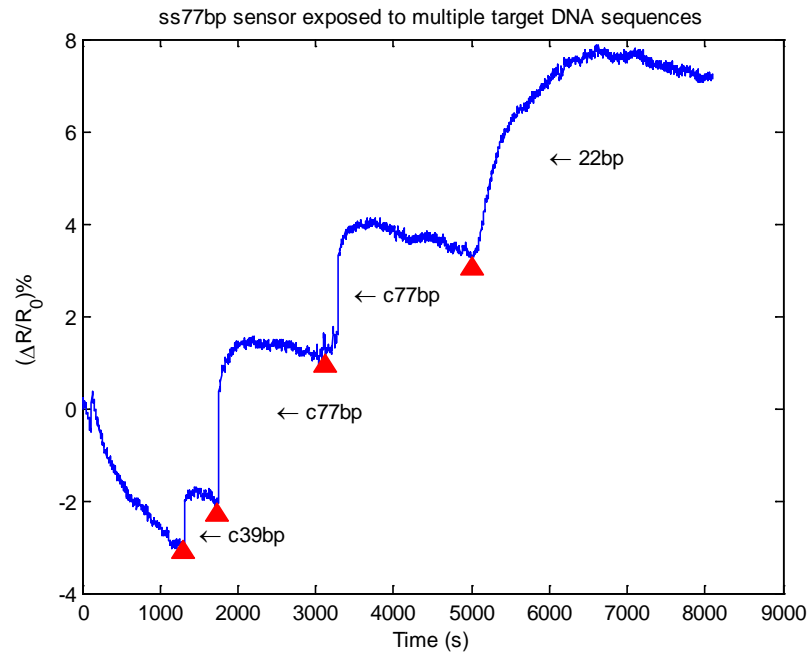
Figure 47: Static test of 77bp aptamer sensor versus multiple DNA targets.

The initial 120 seconds shows the resistance change of a dry circuit. The resistance change between 121 seconds to 1320 seconds was the circuit equilibriating to 10 µL of DI water. After equilibrating, the first exposure was a 10 µL complimentary half-sequence 39bp target aptamer for a 1% resistance change. The second exposure was to 10 µL of complimentary 77bp target aptamer for a 3.6% resistance change. The third exposure was to another 10 µL of complimentary 77bp target aptamer for another 3.6% resistance change. The last exposure was to a 10 µL noncomplimentary 22bp target aptamer for a 4.6% resistance change.

Figure 48 shows the ssDNA77bp sensor response to a 10 µL, 1.0 µM complimentary 77bp target aptamer in a static test configuration. The reaction time starts at 210 seconds at 1.016% and increases to 8.16% over 130 seconds. This represents a resistance increase of 7.14%.
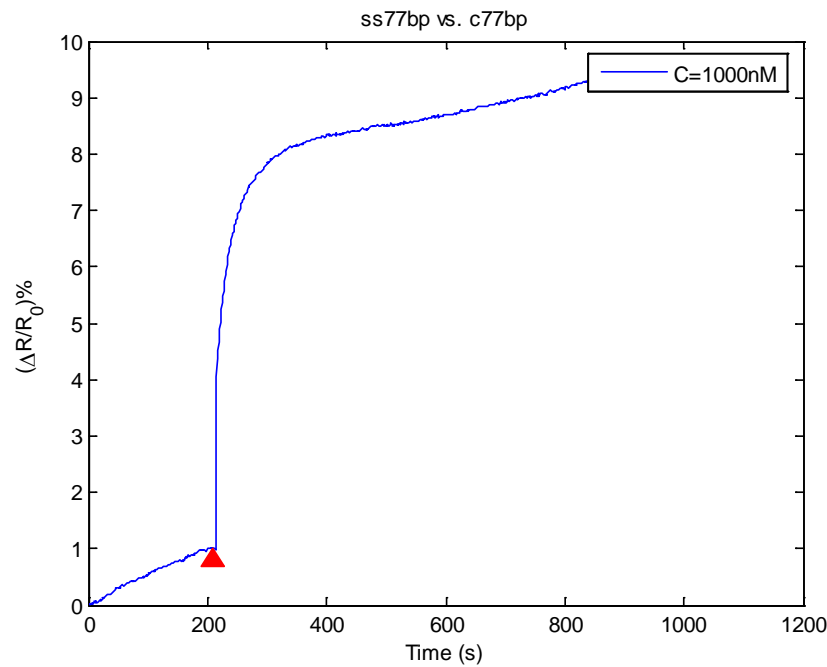
Figure 48: Static test of 77bp circuit versus 1000nM, 77bp target aptamer.

The response was rather large due to the amount of target aptamer used. The increase in sensor response after the exposure is expected to be from sensor drift.

4.2.7   ssDNA 77bp versus *B. anthracis* Sterne strain spores

Three static tests were conducted with *B. anthracis* Sterne strain spores against three different sensors. The spores were diluted into ratios; 1:10, 1:100, and 1:1000. The initial 1:10 diluted concentration started from a 50 µL, 7.35×10^5 spores/mL stock solution

of deionized water. The 1:100 diluted concentration was 7.35×10^4 spores/mL in 1 mL of deionized water. The final 1:1000 diluted concentration was 7.35×10^3 spores/mL in 1 mL of deionized water. The spores in the previous concentrations were exposed to an unfunctionalized graphene surface to determine the difference in sensor response. The experiment was carried out with an open probe station connected to the Keithley 4200 SCS. The Keithley was set to record the drain-current versus time at a set $V_{drain} = 0.2$ V DC. The first test shown in Figure 49 explored the drops against non-functionalized graphene surface to determine the circuit response.
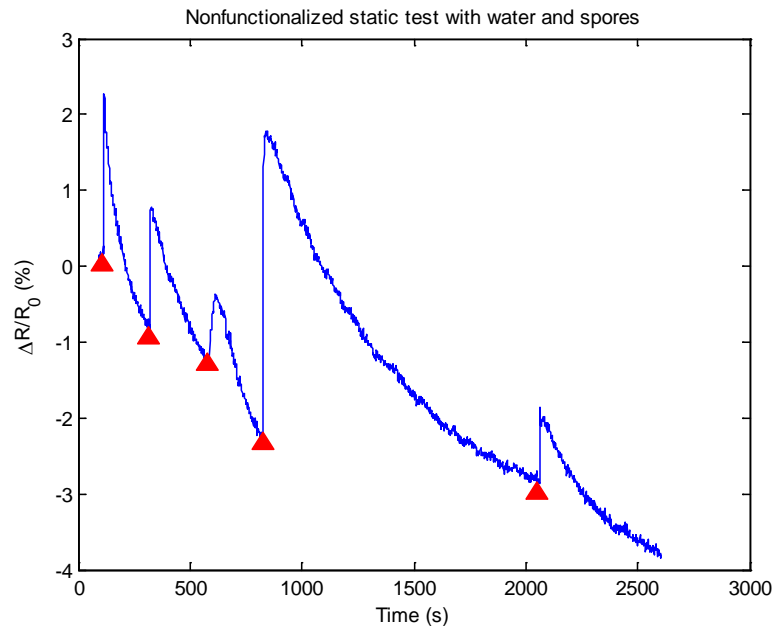
Figure 49: Static drop test of spores and DI water.

Spores dropped in 10 µL DI water increments at a starting concentration of 7.35×10^8 spores/L. The first 3 drops are spores, the fourth and fifth drops are DI water. The inject points were varied to determine if the drop order mattered or if there would be

101

a significant change in the signal slopes measurements. The slopes in Figure 49 look very similar. This can be interpreted as spores introduced to non-functionalized graphene do not have the same effect as spores on a functionalized graphene surface. This indicates a need for a functionalized graphene surface to determine if spores are present or not.

The next static test is shown in Figure 50 was performed as the 77bp functionalized circuit was exposed to two concentrations of 3675 spores/L of *B. anthracis*. The spore samples (3675 spores/L) were pipetted into a 10 µL volume from a 50 µL base stock of 7.35×10^{8} spores/L.
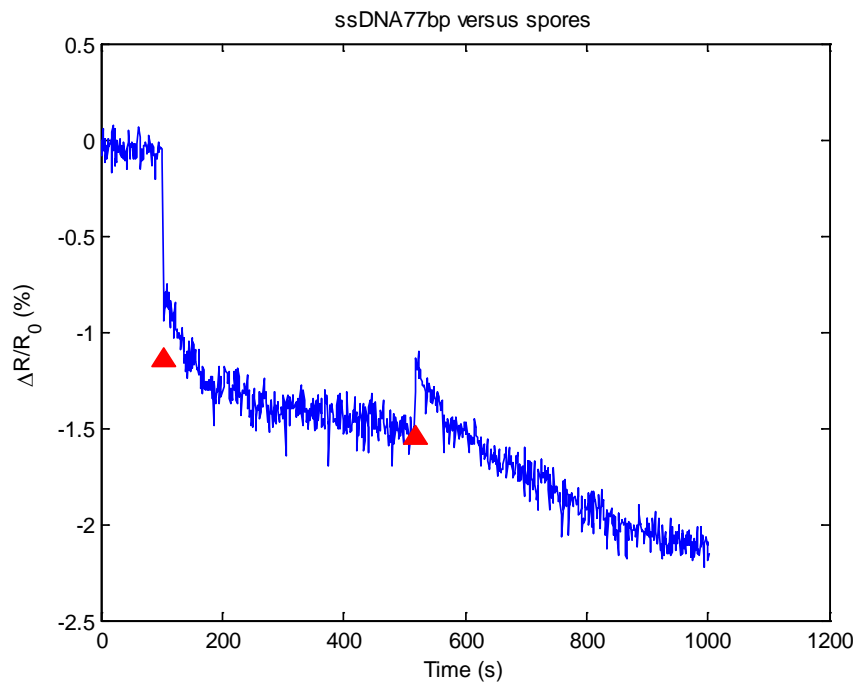
Figure 50: ssDNA77bp functionalized circuit exposed to *B. anthracis* Sterne strain.

The first 10 µL drop started at 100 seconds and resulted in a 0.75% decrease. The second drop started at 522 seconds and resulted in a 0.7% decrease in resistance. The decrease in circuit resistance is indicative of spore attachment to the surface of the circuit.

Figure 51 shows the percent resistance change as a function of the concentration of spores introduced to the 77bp circuit. The low percent resistance change could be due to the age of the sensor, the time required for the spores to disperse in the water or possibly the number of spores "competing" for sites on the ss77bp aptamers.
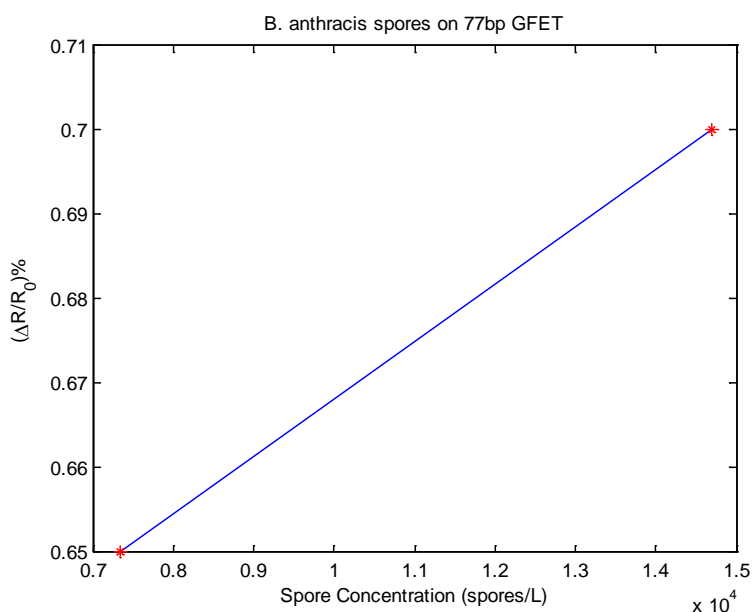
Figure 51: *B. anthracis* Sterne strain spores exposed to 77bp GFET sensor.
Spore concentration was between 7350 and 14700 spores per liter.

Figure 52 shows the ssDNA77bp sensor exposed to a 1 µL concentration of approximately 735 spores at 360 seconds. The sensor resistance seems to increase momentarily as the spores are absorbed onto the surface. It is not clear because the spores should have a negative charge associated with their surface structure, if it can be

assumed that the spores can be similarly modeled as *B. cereus* spores [93]. This trend

disappears with the addition of a 5 µL concentration of 3750 spores at 664 seconds and

the addition of a 5 µL concentration of 3750 spores at 990 seconds.
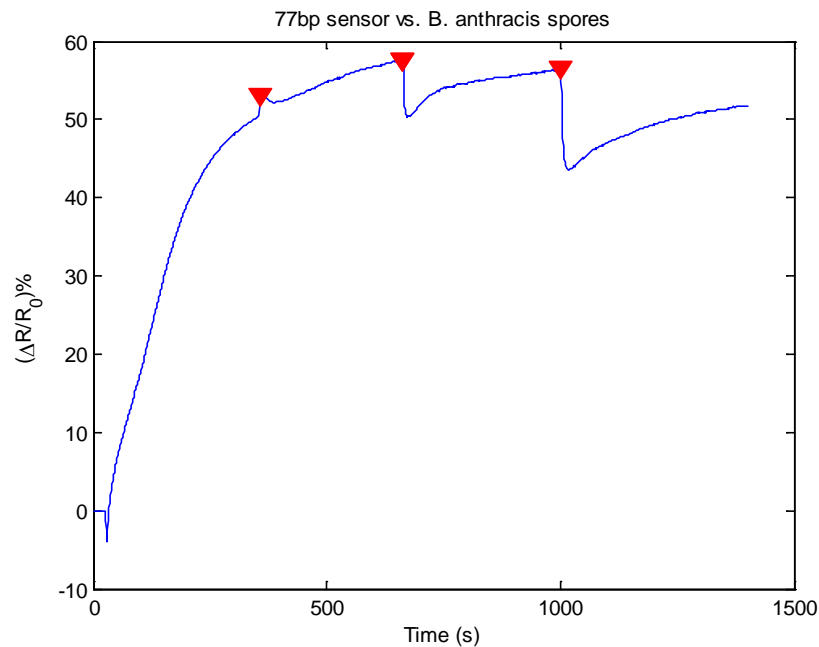
Figure 52: 77bp sensor response to *B. anthracis* Sterne strain spores.

The response in Figure 52 seems reasonable as the spores are expected to bind

into the ssDNA 77bp aptamer quickly and it is supposed to show a decrease in resistance.

Figure 53 was constructed to give an idea of the overall sensitivity of the 77bp

aptamer as a function of being exposed to certain spores/Liter concentrations of *B.*

anthracis. The sensitivity equation previously discussed could be used to determine what

the overall sensitivity is from the data but it would be more prudent to not calculate it

because there are only 3 data points to use. More replicates are needed before a decent

sensitivity can be determined.
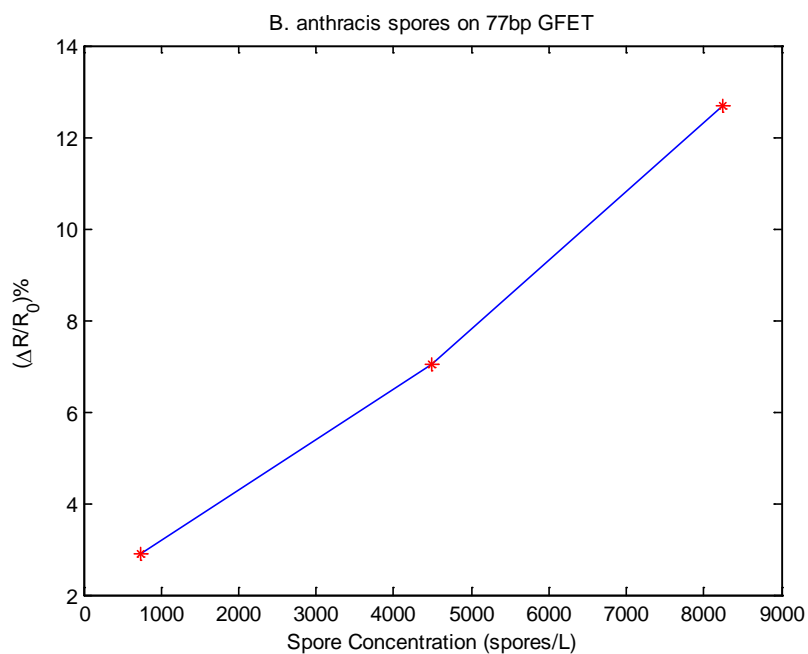
Figure 53: Percent resistance change to *B. anthracis* Sterne strain spores.

The ssDNA77bp aptamer sensor that had been exposed to *B. anthracis* spores was taken to a lab with an AFM for further analysis. The sensor was mildly sonicated for 5 minutes and washed with DI water. Figure 54 shows two areas that were explored with the AFM. Notice in the picture there is a lot of debris. The sensor may have picked it up during the testing or during the overall design as these sensors were not built in a clean room and were also tested to determine if a quick and cheap sensor could be constructed and used with relative ease.

Imaging region, scan size: 30 µm, 10 µm
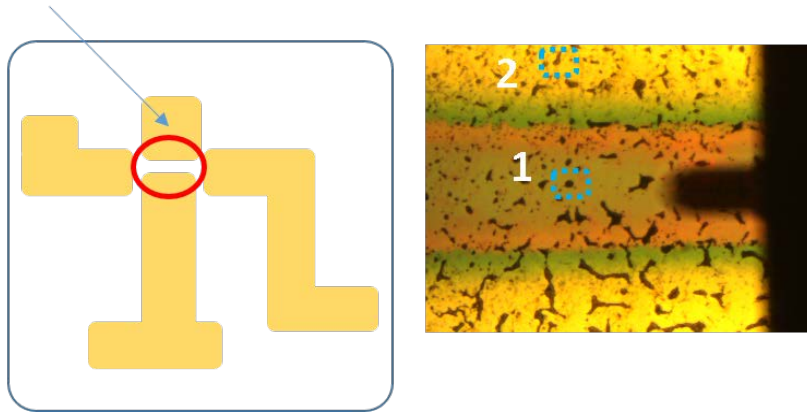
Figure 54: ssDNA77bp functionalized circuit exposed to *B. anthracis.*

Figure 55 shows *B. anthracis* Sterne strain spores present on the surface of the sensor. The spores are clearly indicated by the large white globules on the surface. It is unclear whether the spores are attached due to the 77bp strands on the functionalized surface or if they are there because it was a suitable spot to aggregate. The bottom images have been magnified to determine if ssDNA 77bp strands are present on the surface of the sensor. The lower left image shows large cable-like structures that could be indicative of ssDNA77bp strands forming homo-dimers on the surface. The red arrow indicates structures that are 150-700 nm wide and 35 nm in height. The yellow arrow indicates structures that are 200-400 nm and 35 nm in height. All in all, the most that can be said is that there are *B. anthracis* spores on the circuit.
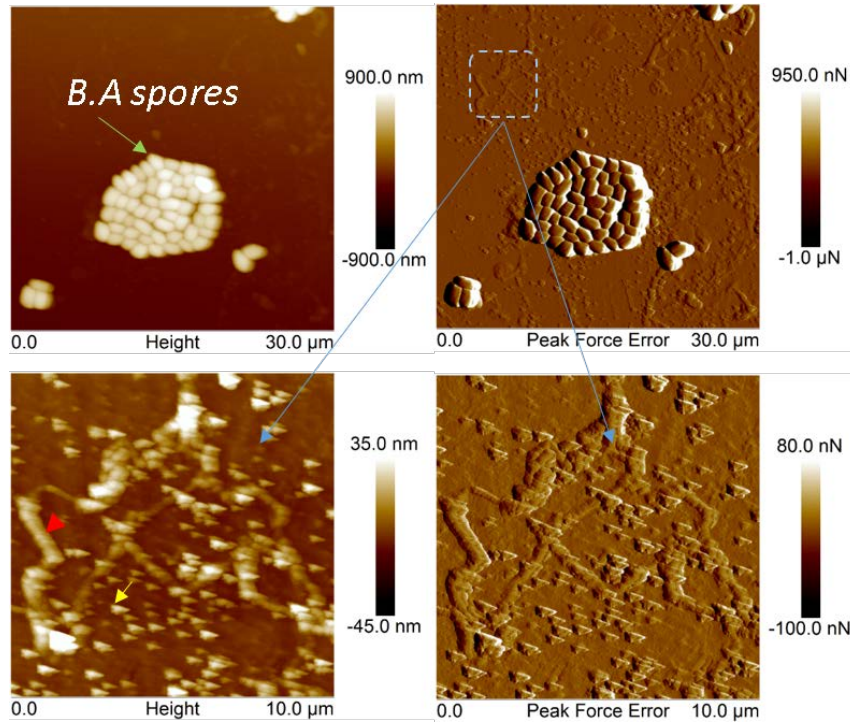
Figure 55: AFM images of *B. anthracis* Sterne strain spores on a ssDNA 77bp functionalized circuit.

The second test region (Figure 54) was taken on top of the gold probe. The data also has large clusters of *B. anthracis* Sterne strain spores and structures similar to Figure 55. It seems that the *B. anthracis* Sterne strain spores attached wherever they fell. It also seems that the chain-like structures and blob-like structures have coated and adhered to the area where the aptamer functionalization solution was deposited. The expanded pictures on the bottom show cable-like structures. The red arrow indicates the structures are between 150 nm to 700 nm wide and vary in height from 40 nm to 80 nm. The yellow arrow indicates structures that are 200x400nm in area and vary in height from 20nm to 60nm. These structures are too large to be 77bp aptamer used to construct this sensor. There is the possibility that the aptamers formed homodimers on themselves and formed much larger structures. Figure 56 shows more B. anthracis spores and focuses on a cleaner area

107

on the AFM. The structures show long chains which is surprising but unless the 77bp

aptamers formed homodimers and bound together there is not much that can be said with

certainty.
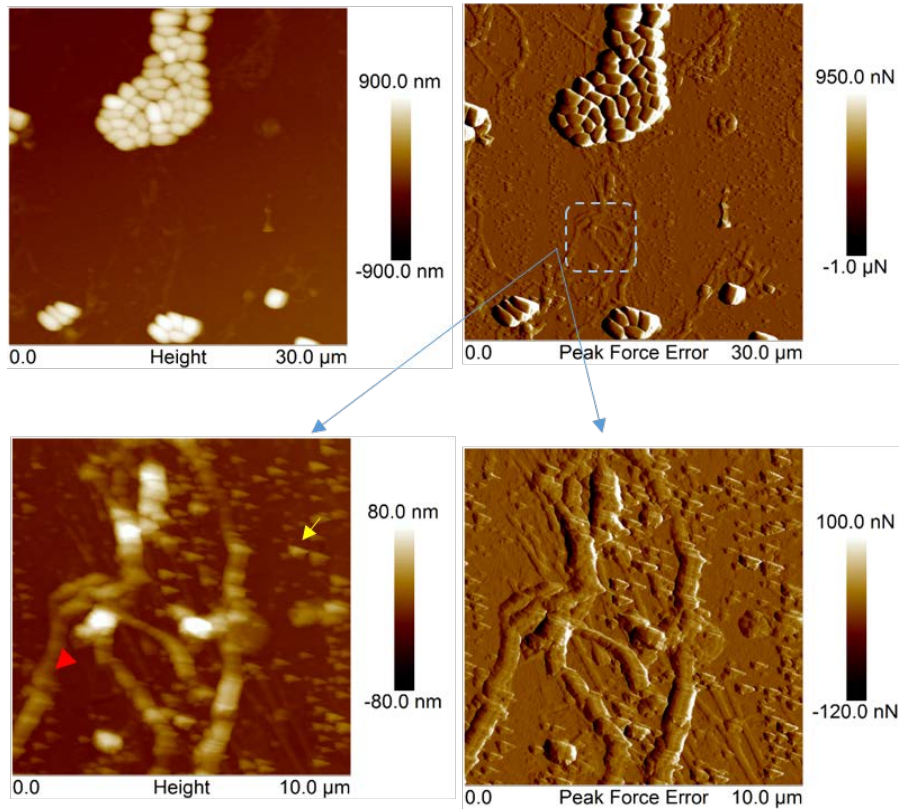
Figure 56: AFM of *B. anthracis* clumped on 77bp circuit.

The most that could be said from this picture is that there are *B. anthracis* spores on top

of the ssDNA 77bp aptamer functionalized circuit. There is little or no way to determine

if the spores are truly held down by the ssDNA 77bp aptamers.

V.   Discussion

5.1   Summary of Results

The primary goal of this research was to determine if it was possible to detect a signal from a complimentary binding event between ssDNA and cDNA aptamers derived from the *B. anthracis* Sterne strain genome on a graphene substrate. The change in resistance of the ssDNA22bp graphene sensor decreased upon exposure to cDNA22bp and increased upon exposure to cDNA39bp and cDNA77bp. The increase in current indicates ssDNA22bp underwent conformational binding with cDNA22bp and detached from the graphene surface. The change in resistance of the ssDNA77bp increased the most when exposed to cDNA77bp, cDNA39bp which was expected. It also changed when exposed to DNA22bp, and the degenerate DNA18bp but less. The magnitude of the resistance change for dissimilar base pair suggests the ability to discriminate between different types of DNA.

Figure 57 shows the relative first peak magnitude response of the 22bp functionalized sensor while it is exposed to the cDNA22bp target aptamer, 39bp target aptamer, and 77bp target aptamer as functions of their concentrations. The figure shows a very large magnitude response of the 22bp functionalized sensor to the 77bp target aptamer. This is likely due to the heterodimer configurations that the 77bp target aptamer can form with the 22bp aptamer.

The 22bp functionalized aptamer was a little less responsive to the 39bp target aptamer. This is also likely due to the heterodimer configurations that the 39bp sequence can form with the 22bp functionalized aptamer.
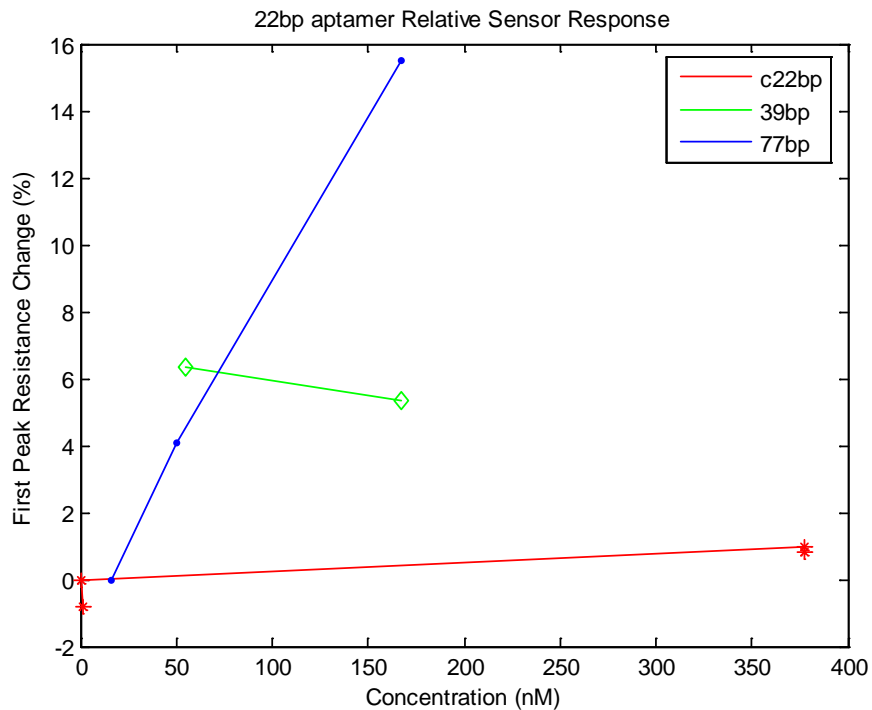
Figure 57: Relative first peak magnitude response for the 22bp functionalized
sensor versus multiple target aptamers.

The sensitivity equation given by DARPA could be used to report data. However, it
would still need to be translated into a format that could map the solution concentration
profiles directly to particles per air volume. It should also be stated that more data is
needed before a sensitivity determination is made.

Figure 58 shows a compilation of the relative first peak magnitude response of the
77bp aptamer functionalized sensor versus multiple target aptamers at various
concentrations. The 77bp aptamer functionalized circuit responded the most to the 77bp
target aptamer. The 22bp target aptamer response was a bit different. The outcome can
be attributed to either bad data or possibly some other electrical/conformational binding
effect that showed up one time and needs further review.
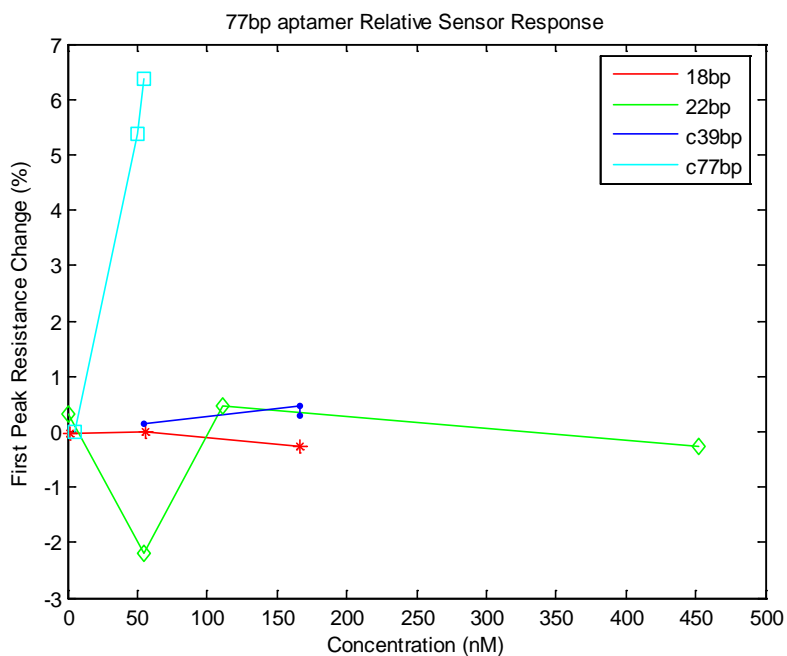
Figure 58: 77bp functionalized sensor response to multiple target aptamers.

The 22bp and 77bp sensor responses against *B. anthracis* Sterne strain spores are plotted in Figure 59 to give a side by side comparison. The data suggest that for a static test with small water droplets infused with spores, the 77bp sensor performed approximately 2 times better than the 22bp sensor based on the limited data available. The responses provided by the 22bp and 77bp functionalized graphene circuit suggest there may be a way to detect *B. anthracis* spores or other biological weapons very quickly, somewhat accurately and cheaply. If a number of these sensors were put out into an area of interest, some of them would pick up on the agent while others might miss it, but on the whole, if the sensors were netted together, the detection of a biological release would be picked up much quicker than one of these units by itself.
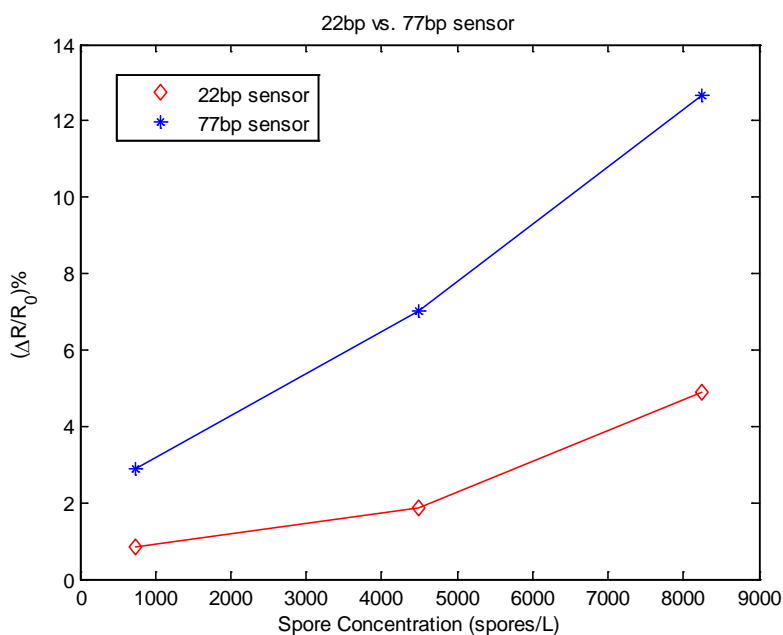
Figure 59: 22bp and 77bp sensor response to *B. anthracis* Sterne strain spores.

The aptamers and the sensor still need to be fully characterized to determine how they react when bacteria come in contact with them and how long they can survive in the field. Keep in mind from an aqueous solution perspective the 77bp aptamers were shown to discriminate between *B. anthracis* and *F. tularensis* the big question is can the aptamers and the sensor perform as well or better with an aerosolized agent? Also, some of the circuits used in this research were functionalized and sat on the shelf for weeks until needed. This indicates a shelf life for this particular setup but there may be ways to keep the aptamers on hand until they are needed to be put on a sensor. From an operational standpoint, the sensor has no serviceable parts. The only user support required would be getting them to an area of interest and waiting for the sensor to trigger on detection. That has to be a plus on the battlefield. The devices were tested at 0.2V

throughout the experiment, so scaling the circuit down to something that can be driven with a watch battery or less is within our capability.

5.2   Conclusion

After functionalizing two graphene circuits with ssDNA22bp and ssDNA77bp aptamers and exposing them to microfluidic environments with solutions of 18bp DNA, 22bp DNA, 39bp DNA, and 77bp DNA and reviewing the percent changes in resistance, we can conclude that there is a difference in percent resistance change and that it may be related to the DNA length, and base pair sequence. We also conclude that this may provide the ability to discriminate between different types of DNA in microfluidic environments. The static tests showed marked changes in the 22bp and 77bp aptamer responses against the previous target aptamers listed. The 22bp and 77bp also showed significant percent resistance changes when *B. anthracis* Sterne strain spores were used against them.

5.3   Future Research

The scope of this research was truly broad, and opportunities for future research exist along many different avenues. The most pressing portions of the next stage of this research should involve a full characterization of the electric double layer associated with the ssDNA77bp aptamer via AC voltammetry.

The target aptamers should be tried without the addition of fluorophores to determine if they have any effect on the ssDNA77bp aptamer complimentary binding signal. Furthermore, the original 40 base pair aptamer sequence with a 3 to 6 chain linker

should be tried in the microfluidic state and the static fluid to determine if that particular configuration allows for better detection and attachment.

A quick next step would be to continue the spore exposure with larger concentrations to make sure the responses are still going in the same direction. The follow on step would be to test the sensor against a spray bottle with DI water to better understand the sensor response to water spray instead of plain fluid. After that the same delivery mechanism could be used to spray spores onto the circuit and determine the response.

The sensor build process could be improved by investing in a stock metallic mask to standardize the circuit layout and reduce connection issues with the Dolomite resealable lab chip.

The graphene surface functionalization process could be improved by developing either a graphene growth process on the chip or a surface adhesion process that reduces the variability encountered with the thermal tape transfer process. A 3D printer process could be designed to place multiple aptamers side by side or in different patterns to enhance detection capabilities. Multiple variations of the *B. anthracis* ssDNA77bp aptamer and the *pagA* pXO1 and *capB* pX02 plasmids could be researched and tested with circuit designs used in this research [29].

Electromagnetic characterization and modeling of the ssDNA-cDNA binding events while dispersing in a "static" fluid and in dynamic flow fields could help determine what molecular species or DNA might affect the aptamer. It should also be

114

performed in the Au-Cr-graphene electrode interface to determine how the ssDNA aptamer or target DNA interact with those surfaces.

Computational fluid dynamics analysis should also be carried out near the Au-Cr-graphene interface to determine if 20 uL/min is considered laminar or turbulent at the 10nm length scale. Sensor characteristics such as the transfer function, calibration, repeatability, resolution, dynamic characteristics, environmental factors, accuracy, and output impedance should be studied if it is decided to stick with a silicon dioxide substrate or switch to a different substrate.

And sensor integration into a radio-frequency identification unit should be pursued as well.

Appendix A: Equipment and Settings

Appendix: A.1 – Dataplate Digital Hotplate

Appendix: A.2 – Tenma Multimeter

Appendix: A.3 - Keithley 4200 SCS & Probe Station

Appendix: A.4 – Syringe Pump / H_2O Properties

Appendix: A.5 – Dolomite Microfluidic Cell

Appendix: A.6 – Raman In-via Laser Spectrometer

Appendix: A.1 – Dataplate Digital Hotplate

General Operation:

Press right hand side on/off switch

Press ENT (Set) button

Press 1 (Plate Temp)

Press numbers needed in Celsius.

Press ENT (Set) button

This will set the Dataplate to the required Celsius temperature. The LCD will flash the current plate temperature versus the target plate temperature until the temperatures are equal. Be careful, the plate heats at approximately 1 °C every 3 seconds. Remember to shut the unit off and unplug it when finished.

Graphene temperature transfer: T = 125 °C.

DNA removal temperature: T = 30 °C to 50 °C.

Appendix: A.2 – Tenma Multimeter

Use:

1.) Twist knob from OFF position to Ω position.

2.) Take red probe and black probe and put them on opposite circuit leads

3.) Unit will display a resistance value or it will display 0L.

4.) If it displays 0L, it means the circuit does not conduct and you need to find a new

one.

Appendix: A.3 - Keithley 4200 SCS

To use the Keithley 4200 SCS:

1. Turn the system on
2. Start Keithley interactive Test Environment (KiTE)
3. Find I-V tester
4. Ensure triaxial SMU connectors are attached to the correct test circuit
5. Set Voltage bias to 0.2 volts
6. Set current compliance to 1.0 picoAmperes
7. Set sample buffer to 4000
8. Set sample rate to 1 sample per second
9. Test I-V curve, look for hysteresis or 2 to 3 order of magnitude jumps in response
    9.a. If either of these are found, make sure the DRU leads are in contact with the
    circuit electrical pads
10. Switch to Four Terminal vgs-id plot
11. Ensure SMUs are same as I-V curve configuration
12. Start test (a. Dynamic Microfluidic Test, b. Static Test)
    A.1   Hook inlet and outlet tube to Dolomite resealable unit
    A.2   Find 2mL Eppendorf vial – poke two holes in the top and fill w/ DI water
    A.3   Push inlet tube into the hole at the top of the Eppendorf vial, make sure
          the inlet tube touches vial bottom, fill vial with 500 µL DI water
    A.4   Hook Dolomite outlet tube to the Syringe Pump
    A.5   Turn Syringe Pump on, set to 20.00mL and begin pumping
    A.6   Watch inlet tube, DRU and outlet tube fill with DI water
    A.7   After steady state flow established,
    A.8   Go to the 4200SCS and select vgs-id under four terminal setup
    A.9   Check SMU set up ensure same as used in I-V curve test
    A.10 Drain voltage = 0.2V; Sample set to 4000; Sample rate 1/second
    A.11 Monitor sensor for 2% of the response envelope over 100 seconds
    A.12 Inject sample when DI water is within 10 µL of vial bottom
    A.13 Monitor to ensure proper test concentration remains in the Eppendorf vial
    A.14 Insert 500 µL to 1000 µL of DI water into the vial and let test
          run to 4000 seconds

    B.1 Monitor test for 2% envelope and the aptamer inject point
    B.2 Once the 2% envelope is there inject the aptamer onto the circuit
    B.3 Monitor to ensure good signal

Appendix: A.4 – Syringe Pump / H_2O Properties

Syringe Pump:

Volume: 12 mL syringe

Volumetric Flow Rate: 20 µL/min = 0.34 µL/s

Water:

μ (T = 25 ºC) = 8.90 × 10^{-4} Pa*s

ρ = 997 kg/m^3

Appendix: A.5 – Dolomite Microfluidics Chamber Information

Microfluidics Chamber:

Width: 11.00 mm = 0.011 m

Length: 20.4 mm = 0.0204 m

Depth: 100 μm = 0.0001 m

Volume: 16.73 mm^3 = 0.01673 mL = 16.73 μL

Microfluidics Chamber Tubes:

Front End Tube Length: 0.8084 m

Front End Tube Inner Diameter = 0.8 mm (per Dolomite manuals)

Area = $\pi*(d^2)/4 = \pi*(0.8 \text{ mm}^2)/4 = 5.026 \times 10^{-7} \text{ m}^2$

Approximate travel time from entrance to resealable circuit: 120 - 160 seconds

Backside Tube Length: 2 m

Approximate travel time from resealable circuit to syringe: 300 seconds

Appendix: A.6 – Raman In-via Laser Spectrometer

Raman inVia Spectroscopy Chamber: 532 nm laser

Range: 100 to 4000 cm^{-1}

Running conditions: ambient temperature, ambient pressure, ambient humidity

Use: Thin film surface changes, chemical identification

Limits: No lifeforms in chamber

Appendix B: Circuit Recipes

Appendix B.1 – Graphene Growth Recipe

Appendix B.2 – Circuit Metallization

Appendix B.3 – Graphene Functionalization

Appendix B.1: Graphene Growth

Credit for this section goes to Yen Ngoo (AFRL/RXAS) for both the writeup and the

processing and delivery of the graphene used on this project.

Growth:

The chemical vapor deposition technique to deposit gaseous reactants into a

substrate. A thin copper foil is used and placed into a high temperature tube furnace and

the sample is aged under 1000 °C for 30 minutes with hydrogen gas (125 mTorr pressure)

flowing into the chamber. Then both precursor gases (methane (1.25 Torr pressure) and

hydrogen (125 mTorr) gases) are used and undergo chemical reactions under a furnace at

same temperature. This is run for another 30 minutes. The chemical reaction from the

combined gases creates a material film of carbon onto the copper foil. Instrument used

for graphene growth is high temperature vacuum tube furnace OTF-1200X-S.

Preparation:

Thermal release tape is used to transfer copper foil grown graphene onto other

substrates. This type of heat release tape is unique because it behaves like normal

adhesive tape at room temperature but can be easily peeled off by adding heat to it. For

the specific thermal release tape we use, it peels off at 125 °C. Other tapes may have

varying temperatures that they peel off, it just depends on the kind of tape.

The copper foil is placed onto the tape and ready for the etching process.

The etching process consists of using ammonium persulfate as a solution and the tape

plus copper sample is submerged into the etchant solution. After 2 hours, the copper foil

dissolves away, leaving only the graphene attached to the tape. The tape is washed with distilled water and nitrogen dried. The sample is ready for transfer to the substrate. Transfer:

The tape (with graphene) is placed onto substrate and with no air bubbles present between the tape and the substrate. The substrate and tape can then be placed onto hotplate with temperature of about 125 °C and the tape will instantly come off. This leaves the graphene layer on the sample. This method can be done multiple times for multiple layers of graphene on a sample. The samples can then be annealed under a furnace at 345 degrees C for 4 hours (constant flow rate of Argon gas and hydrogen gas) – this step is needed in order to get rid of any tape residue left from the transfer process as well as removing any other biomolecules or contaminants from the sample.

Appendix B.2 – Circuit Metallization

Special thanks to Gerry Landis (AFRL/RXS, CTR) for metallizing the circuits used in this research. The circuit metallization is accomplished by sputter deposition under the following conditions. For further information concerning the circuit metallization process, please contact him.

Table 7: Sputter deposition chamber parameters

Sputter Deposition Chamber Parameters for Cr and Au		
Material	Cr	Au
Deposition Rate (m/s)	4.0×10^{-10}	3.0×10^{-10}
Voltage (V)	600	600
Current (A)	0.88	0.188
Chamber Gas (Argon)	5.0×10^{-6}	5.0×10^{-6}
Vacuum Pressure (Torr)	5.0×10^{-3}	6.0×10^{-6}

Appendix B.3 – Graphene Functionalization

Reference Chen's work [15] and modify 6mM pyrenebutanoic acid, succinimidyl ester

(PBASE) in N-N dimethylformamide (DMF) to 10mM PBASE in DMF.

1. Prepare a 10mM solution of PBASE in DMF.

2. Place graphene functionalized circuits in a 400mL glass beaker (see figure below)

3. Use a glass pipette to transfer 5.0 µL of PBASE onto the graphene functionalized area.

4. Cover beakers with Parasol M paper.

5. Let the graphene functionalize for 1 hour at room temperature (303K).

6. Rinse circuits with 1mL pure DMF

7. Dispose of waste products properly.

Figure 60: Circuits readied for PBASE functionalization. Recommend actions be performed under a working fumehood as DMF is toxic.
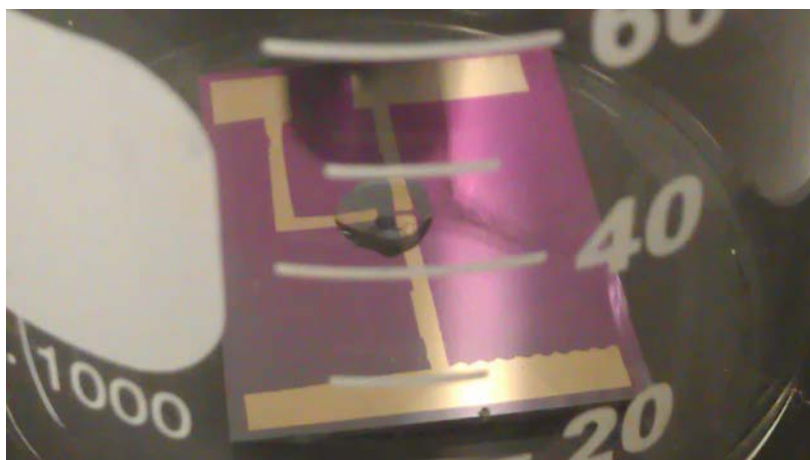
Figure 61: Graphene functionalized with 5uL of 10mM PBASE in DMF.

Protein immobilization:

1.) Place circuit in a petri-dish or somewhere it can be covered.
2.) Pipette a 5.0 µL solution of 50 µM ssDNA onto the graphene-PBASE functionalized area.
3.) Add 5.0 µL deionized H_2O to help disperse the ssDNA across the functionalized area.
4.) Add a small amount of deionized H_2O to the petri-dish to equalize vapor pressure and minimize evaporation.
5.) Cover circuits and wait for 18 hours at room temperature (303K)
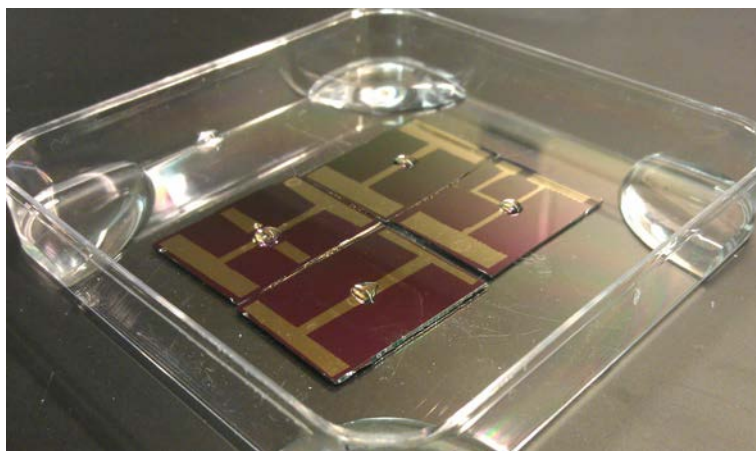
Figure 62: Four circuit ssDNA functionalization. The droplets are 10uL, 50uM concentrations of ssDNA in deionized water. The functionalization time is 18 hours. Deionized water is placed around the corners of the petri dish to slow down evaporation. The petri dish lid was put back on after this shot was taken.

References:

[1]   G. A. Office, "BIOSURVEILLANCE DHS Should Reevaluate Mission Need and
        Alternatives before Proceeding with BioWatch Acquisition," Government
        Accountability Office, United States of America, GAO-12-810, 2012.

[2]   "Defense Threat Reduction Agency Broad Agency Announcement HDTRA1-12-
        CHEM-BIO-BAA Chemical / Biological Technologies Directorate FY2012 –
        FY2013 Program Build," no. August. pp. 1–85, 2010.

[3]   P. Ashley, *The Complete Encyclopedia of Terrorist Organizations*. 2011, pp. 77–
        80.

[4]   R. Danzig, M. Sageman, T. Leighton, L. Hough, H. Yuki, R. Kotani, and Z. M.
        Hosford, "Aum Shinrikyo, Insights Into How Terrorists Develop Biological and
        Chemical Weapons," Washington D.C., 2011.

[5]   N. C. F. Biotechnology Information, "Bacillus anthracis genomes," 2004. [Online].
   Available: http://www.ncbi.nlm.nih.gov/genomes/MICROBES/anthracis.html.
        [Accessed: 03-Aug-2013].

[6]   C. B. Inc., "OpenPCR," 2013. [Online]. Available: http://www.openpcr.org.
        [Accessed: 05-Mar-2014].

[7]   "GenomeCompiler," 2014. [Online]. Available: http://www.genomecompiler.com.
        [Accessed: 05-Mar-2014].

[8]   K. Schmitt and N. Zacchia, "Total decontamination cost of the anthrax letter
        attacks," *Biosecur. Bioterror.*, vol. 10, no. 1, pp. 98–107, 2012.

[9]   J. P. Robinson, C.-G. Heden, and H. Von Schreeb, *The Problem of Chemical and
        Biological Warfare: CB Weapons Today, vol II.* New York: Stockholm Peace
        Research Institute, 1973, p. 135.

[10]   B. Findlay, "Don't Feed the Bioterrorism Threat," 2009. [Online]. Available:
        http://www.stimson.org/spotlight/dont-feed-the-bioterrorism-threat/. [Accessed:
        02-Feb-2014].

[11]   D. Ivnitski, D. Morrison, and D. J. O. Neil, "CRITICAL ELEMENTS OF
        BIOLOGICAL SENSOR TECHNOLOGY FOR DEPLOYMENT IN AN
        ENVIRONMENTAL NETWORK SYSTEM," in *Defense against Bioterror:
        Detection Technoloiges, Implementation Strategies and Commercial
        Opportunities*, D. Morrison, Ed. Springer, 2005, pp. 207–220.

[12]   H. Tao, J. D. Clayton, D. L. Kaplan, R. Rajesh, and G. Fiorenzo, "on tooth enamel," *Nat. Commun.*, vol. 3, pp. 763–768, 2012.

[13]   N. Mohanty and V. Berry, "Graphene-Based Single-Bacterium Resolution Biodevice and DNA Transistor : Interfacing Graphene Derivatives with Nanoscale and Microscale Biocomponents," *Nanoletters*, vol. 8, no. 12, pp. 4469–4476, 2008.

[14]   Y. Hu, K. Wang, Q. Zhang, F. Li, T. Wu, and L. Niu, "Biomaterials Decorated graphene sheets for label-free DNA impedance biosensing," *Biomaterials*, vol. 33, no. 4, pp. 1097–1106, 2012.

[15]   R. J. Chen, Y. Zhang, D. Wang, and H. Dai, "Noncovalent Sidewall Functionalization of Carbon Nanotubes for Protein Immobilization," *J. Am. Chem. Soc.*, vol. 123, no. 16, pp. 3838–3839, 2001.

[16]   M. Fan, S. R. Mcburnett, C. J. Andrews, A. M. Allman, J. G. Bruno, and J. L. Kiel, "Aptamer Selection Express : A Novel Method for Rapid Single-Step Selection and Sensing of Aptamers," *J. Biomol. Tech.*, no. 19, pp. 311–321, 2008.

[17]   Y. Zhu, S. Murali, W. Cai, X. Li, J. W. Suk, J. R. Potts, and R. S. Ruoff, "Graphene and Graphene Oxide: Synthesis, Properties and Applications," *Adv. Mater.*, vol. 22, no. 35, pp. 3906–3924, 2010.

[18]   Y. Cui, S. N. Kim, S. E. Jones, L. L. Wissler, R. R. Naik, and M. C. McAlpine, "Chemical functionalization of graphene enabled by phage displayed peptides.," *Nano Lett.*, vol. 10, no. 11, pp. 4559–65, Nov. 2010.

[19]   G. Saltzgaber, P. Wojcik, T. Sharf, M. R. Leyden, J. L. Wardini, C. a Heist, A. a Adenuga, V. T. Remcho, and E. D. Minot, "Scalable graphene field-effect sensors for specific protein detection.," *Nanotechnology*, vol. 24, no. 35, p. 355502, Sep. 2013.

[20]   Y. Ohno, K. Maehashi, and K. Matsumoto, "Label-Free Biosensors Based on Aptamer-Modified Graphene Field-Effect," *J. Am. Chem. Soc.*, vol. 132, no. 50, pp. 18012–18013, 2010.

[21]   Z. F. Dembek, Ed., *Medical Aspects of Biological Warfare*. Washington D.C.: Office of the Surgeon General at TMM Publications, 2007, p. 607.

[22]   T. De Siano, S. Padhi, D. W. Schaffner, and T. J. Montville, "Growth Characteristics of Virulent Bacillus anthracis and Potential Surrogate Strains," *J. Food Prot.*, vol. 69, no. 7, pp. 1720–1723, 2006.

[23] S. R. Klee, M. Ozel, B. Appel, C. Boesch, H. Ellerbrok, D. Jacob, G. Holland, F. H. Leendertz, G. Pauli, R. Grunow, and H. Nattermann, "Characterization of Bacillus anthracis-like bacteria isolated from wild great apes from Cote d'Ivoire and Cameroon.," *J. Bacteriol.*, vol. 188, no. 15, pp. 5333–44, Aug. 2006.

[24] "Anthrax: Bacteriology, Clinical Presentation and Management," 2012. [Online]. Available: http://www.siumed.edu/medicine/id/anthrax.htm#micro.

[25] J. Carrano, T. Jeys, J. Eversole, J. Gillespie, N. Licata, W. Loerop, M. Munley, M. O'Keefe, J. Roos, A. Samuels, J. Schultz, M. Shatz, N. Wong, F. D'Amico, A. M. Casale, S. E. Holster, J. F. McGrath, A. Metrovich, C. Murphy, K. Nelson-Patel, E. Reich, and T. Riisager, "Chemical and Biological Sensor Standards Study II, October 2010," 2010.

[26] D. Ivnitski, D. Morrision, and D. J. O'neill, *Defense Against Bioterror NATO Security through Science Series*. Springer, 2005, pp. 207–220.

[27] I. Chen and D. Dubnau, "DNA uptake during bacterial transformation," *Nat. Rev.*, vol. 2, pp. 241–249, 2004.

[28] B. K. Purcell, P. L. Worsham, and A. M. Friedlander, "Anthrax," in *Medical Aspects of Biological Warfare*, Department of the Army, 2008, pp. 69–90.

[29] M. Emanuel, Peter and Caples, "Chemical, Biological, Radiological Technology Survey," 2011.

[30] C. I. L. Justino, T. a. Rocha-Santos, and A. C. Duarte, "Review of analytical figures of merit of sensors and biosensors in clinical applications," *TrAC Trends Anal. Chem.*, vol. 29, no. 10, pp. 1172–1183, Nov. 2010.

[31] D. Spiegleman, G. Whissell, and C. W. Greer, "A survey of methods for the characterization of microbial consortia and communities," *Can. J. Microbiol.*, vol. 51, pp. 355–386, 2005.

[32] F. V. Wintzingerode, U. B. Gobel, and E. Stackebrandt, "Determination of microbial diversity in environmental samples: Pitfalls of PCR-based rRNA analysis," *FEMS Microbiol. Rev.*, vol. 21, pp. 213–229, 1997.

[33] Y. Ohno, K. Maehashi, and K. Matsumoto, "Graphene field-effect transistors for label-free biological sensors," *2010 IEEE Sensors*, pp. 903–906, Nov. 2010.

[34] T. Kuila, S. Bose, P. Khanra, A. K. Mishra, N. H. Kim, and J. H. Lee, "Recent advances in graphene-based biosensors.," *Biosens. Bioelectron.*, vol. 26, no. 12, pp. 4637–48, Aug. 2011.

[35] M. Pumera, "Graphene in biosensing," *Mater. Today*, vol. 14, no. 7–8, pp. 308–315, Jul. 2011.

[36] T.-Y. Chen, P. T. K. Loan, C.-L. Hsu, Y.-H. Lee, J. Tse-Wei Wang, K.-H. Wei, C.-T. Lin, and L.-J. Li, "Label-free detection of DNA hybridization using transistors based on CVD grown graphene.," *Biosens. Bioelectron.*, vol. 41, pp. 103–9, Mar. 2013.

[37] R. Koch, "The etiology of anthrax, based on the life history of Bacillus anthracis. Beitrage zer Biologie der Ppanzen 1876," *Am. Soc. Microbiol.*, vol. 2, no. 2, pp. 277–310, 1876.

[38] P. Keim, a M. Klevytska, L. B. Price, J. M. Schupp, G. Zinser, K. L. Smith, M. E. Hugh-Jones, R. Okinaka, K. K. Hill, and P. J. Jackson, "Molecular diversity in Bacillus anthracis.," *J. Appl. Microbiol.*, vol. 87, no. 2, pp. 215–7, Aug. 1999.

[39] M. C. Trull, T. V. du Lane, and M. D. Dibner, "Turning biodefense dollars into products," *Nat. Biotechnol.*, vol. 25, pp. 179 – 184, 2007.

[40] A. H. Gaspar, L. A. Marraffini, M. Elizabeth, K. L. Debord, H. Ton-that, and E. M. Glass, "Bacillus anthracis Sortase A (SrtA) Anchors LPXTG Motif-Containing Surface Proteins to the Cell Wall Envelope Bacillus anthracis Sortase A (SrtA) Anchors LPXTG Motif-Containing Surface Proteins to the Cell Wall Envelope," *J. Bacteriol.*, vol. 187, no. 13, pp. 4646–4655, 2005.

[41] M. Moayeri and S. H. Leppla, "Cellular and Systemic Effects of Anthrax Lethal Toxin and Edema Toxin," *Mol. Aspects Med.*, vol. 30, no. 6, pp. 439–455, 2010.

[42] P. Setlow, "I will survive: DNA protection in bacterial spores.," *Trends Microbiol.*, vol. 15, no. 4, pp. 172–80, Apr. 2007.

[43] E. P. Sunde, P. Setlow, L. Hederstedt, and B. Halle, "The physical state of water in bacterial spores.," *Proc. Natl. Acad. Sci. U. S. A.*, vol. 106, no. 46, pp. 19334–9, Nov. 2009.

[44] "Anthrax National Response Team Quick Reference Guide," 2006. [Online]. Available: www.nrt.org/production/nrt/nrtweb.nsf/AllAttachmentsByTitle/A-566ESAnthraxQRG/$File/Anthrax_al.pdf?OpenElement/Anthrax_12_20.indd. [Accessed: 03-Mar-2014].

[45] USAMRIID, *Medical Management of Biological Casualties Handbook*, 7th ed. Fort Dietrick: U.S. Government Printing Office, 2011, pp. 1–270.

[46]   R. J. Doyle and R. E. Marquis, "Elastic, flexible peptidoglycan and bacterial cell wall properties," *Trends Microbiol.*, vol. 2, no. 2, pp. 57–60, 1994.

[47]   D. L. Nelson and M. M. Cox, *Lehninger, Principles of Biochemistry*, 5th ed. New York: W.H. Freeman and Company, 2009, p. 1058.

[48]   J. Atherton, N. Boley, B. Brown, N. Ogawa, S. M. Davidson, M. B. Eisen, M. Biggin, and P. Bickel, "A MODEL FOR SEQUENTIAL EVOLUTION OF LIGANDS," *Ann. Appl. Stat.*, vol. 6, no. 3, pp. 928–949, 2012.

[49]   A. Ellington and J. Szostak, "In vitro Selection of RNA Molecules that Bind Specific Ligands," *Nature*, vol. 346, pp. 818–822, 1990.

[50]   S. Neidle, *Principles of Nucleic Acid Structure*, 1st ed. London: Elsevier Inc., 2008, pp. 1–289.

[51]   K. Denniston, J. Topping, and R. Caret, *General, Organic and Biochemistry*, 6th ed. McGraw-Hill Companies Inc., 2007, pp. 1–928.

[52]   C. Wu, Y. Zhou, X. Miao, and L. Ling, "A novel fluorescent biosensor for sequence-specific recognition of double- stranded DNA with the platform of graphene oxide," *Analyst*, vol. 136, pp. 2106–2110, 2011.

[53]   R. G. Endres, D. L. Cox, and R. R. P. Singh, "Colloquium : The quest for high-conductance DNA," *Rev. Mod. Phys.*, vol. 76, no. January, pp. 195–214, 2004.

[54]   C. M. Bartsch, G. Subramanyam, J. G. Grote, K. M. Singh, R. R. Naik, B. Singh, and N. S. Sariciftci, "Bio-Organic Field Effect T," *Nanobiotronics, SPIE*, vol. 6646, p. 66460K–66460K–12, Sep. 2007.

[55]   K. J. Meiser and J. H. Laidler, *Physical Chemistry*, 3rd ed. Houghton Mifflin Harcourt, 1999.

[56]   I. Integrated DNA Technologies, "OligoAnalyzer 3.1 Toolkit," 2014. [Online]. Available: https://www.idtdna.com/analyzer/Applications/OligoAnalyzer/. [Accessed: 05-Mar-2014].

[57]   R. S. of Chemistry, "Pyrenebutanoic acid, succinimidyl ester: CSID: 115656." [Online]. Available: http://www.chemspider.com/Chemical-Structure.115656.html. [Accessed: 14-Feb-2014].

[58]   R. S. of Chemistry, "Dimethylformamide: CSID: 5993." [Online]. Available: http://www.chemspider.com/Chemical-Structure.5993.html. [Accessed: 01-Jun-2013].

[59]   P. W. Atkins, *Quanta, A handbook of concepts*. Oxford: Clarendon Press, 1974, pp. 75–77.

[60]   T. Hermanson, Greg, *Bioconjugation Techniques*, 2nd ed. San Diego: Academic Press, 2008, pp. 424–900.

[61]   P.-J. J. Huang and J. Liu, "DNA-length-dependent fluorescence signaling on graphene oxide surface.," *Small*, vol. 8, no. 7, pp. 977–83, Apr. 2012.

[62]   R. S. of Chemistry, "Texas-Red: CSID: 398742." [Online]. Available: http://www.chemspider.com/Chemical-Structure.398742.html. [Accessed: 14-Feb-2014].

[63]   S. Kochmann, T. Hirsch, and O. S. Wolfbeis, "Graphenes in chemical sensors and biosensors," *TrAC Trends Anal. Chem.*, vol. 39, pp. 87–113, Oct. 2012.

[64]   H. Chang and H. Wu, "Graphene-Based Nanomaterials: Synthesis, Properties, and Optical and Optoelectronic Applications," *Adv. Funct. Mater.*, p. n/a–n/a, Nov. 2012.

[65]   R. Waser, Ed., *Nanoelectronics and Information Technology*, 3rd ed. Weinheim: Wiley-VCH, 2012, pp. 1–1048.

[66]   C. Kittel, *Introduction to Solid State Physics*, 8th ed. John Wiley and Sons, Inc., 2005, p. 680.

[67]   W. Choi and J. Lee, *Graphene Synthesis and Applications*, 1st ed. Boca Raton: Taylor & Francis Group, 2012.

[68]   E. T. Ando, *Physics and Chemistry of Graphene, Graphene to Nanographene*. Singapore: Pan Stanford Publishing, 2013.

[69]   V. C. Sanchez, A. Jachak, R. H. Hurt, and A. B. Kane, "Biological Interactions of Graphene-Family Nanomaterials : An Interdisciplinary Review," *Chem. Res. Toxicol.*, vol. 25, pp. 15–34, 2012.

[70]   B. Song, G. Cuniberti, S. Sanvito, and H. Fang, "Nucleobase adsorbed at graphene devices: Enhance biosensorics," *Appl. Phys. Lett.*, vol. 100, 2012.

[71]   C. J. Baker, "University Wafer," 2014. [Online]. Available: http://www.universitywafer.com. [Accessed: 27-Aug-2013].

[72] J. Borysiuk, J. Sołtys, and J. Piechota, "Stacking sequence dependence of graphene layers on SiC (0001)—Experimental and theoretical investigation," *J. Appl. Phys.*, vol. 109, no. 9, p. 093523, 2011.

[73] F. Tao and S. Bernasek, *Functionalization of Semiconductor Surfaces*, 1st ed. Hoboken: John Wiley and Sons, Inc., 2012, pp. 1–454.

[74] T. Alava, J. a Mann, C. Théodore, J. J. Benitez, W. R. Dichtel, J. M. Parpia, and H. G. Craighead, "Control of the graphene-protein interface is required to preserve adsorbed protein function.," *Anal. Chem.*, vol. 85, no. 5, pp. 2754–9, Mar. 2013.

[75] H. Pei, J. Li, M. Lv, J. Wang, J. Gao, J. Lu, Y. Li, Q. Huang, J. Hu, and C. Fan, "A Graphene-Based Sensor Array for High-Precision and Adaptive Target Identification with Ensemble Aptamers," *J. Am. Chem. Soc.*, vol. 134, pp. 13843–13849, 2012.

[76] A. K. H. Cheng, D. Sen, and H.-Z. Yu, "Design and testing of aptamer-based electrochemical biosensors for proteins and small molecules.," *Bioelectrochemistry*, vol. 77, no. 1, pp. 1–12, Nov. 2009.

[77] E. Riché, A. Carrié, N. Andin, and S. Mabic, "High-Purity Water and pH," no. July, pp. 1–3, 2006.

[78] J. McMurry, *Organic Chemistry*, 7th ed. Belmont: Brooks/Cole, 2008, p. 521.

[79] D. Skoog, *Fundamentals of Analytical Chemistry*, 8th ed. Cengage Learning, 2003, p. 1176.

[80] A. S. Morris, *Measurement and Instrumentation Principles*, 3rd ed. Butterworth-Hienemann, 2001, p. 512.

[81] P. Blake, E. W. Hill, A. H. Castro Neto, K. S. Novoselov, D. Jiang, R. Yang, T. J. Booth, and A. K. Giem, "Making graphene visible," *Appl. Phys. Lett.*, vol. 91, 2007.

[82] I. Jung, M. Pelton, R. Piner, D. A. Dikin, S. Stankovich, S. Watcharotone, M. Hauser, and R. S. Ruoff, "Simple approach for high-contrast optical imaging and characterization of graphene-based sheets," *Nano Lett.*, vol. 7, pp. 3539–3575, 2007.

[83] T. Thompson, D. Yang, and R. Chimenti, "Raman Analysis of Si Crystallinity," *Spectroscopy*, 2011. [Online]. Available: http://www.spectroscopyonline.com/spectroscopy/Articles/Raman-Analysis-of-Si-Crystallinity/ArticleStandard/Article/detail/739857#. [Accessed: 10-Oct-2013].

[84] W. Cai, J. R. Peck, D. W. van der Weide, and R. J. Hamers, "Direct electrical detection of hybridization at DNA-modified silicon surfaces," *Biosens. Bioelectron.2*, vol. 19, no. 9, pp. 1013–1019, 2004.

[85] *Fundamentals of Engineering Reference Handbook*, 8th ed. National Council of Examiners for Engineering and Surveying, 2008, p. 264.

[86] H. Peng, L. B. Alemany, J. L. Margrave, and V. N. Khabashesku, "Sidewall Carboxylic Acid Functionalization of Single-Walled Carbon Nanotubes," *J. Am. Chem. Soc.*, no. 10, pp. 15174–15182, 2003.

[87] D. Lin-Vien, N. B. Colthup, W. B. Fateley, and J. . Graselli, *The Handbook of Infrared and Raman Characteristic Frequencies of Organic Molecules*. Boston, 1991.

[88] W. Li, C. Tan, M. A. Lowe, H. D. Abruna, and D. C. Ralph, "Electrochemistry of Individual Monolayer Graphene Sheets," *Am. Chem. Soc. NANO*, no. 3, pp. 2264–2270, 2011.

[89] A. C. Ferrari and D. M. Basko, "Raman Spectroscopy as a versatile tool for studying the properties of graphene," *Nat. Nanotechology*, vol. 8, pp. 235–246, 2013.

[90] G. Binning, H. Rohrer, C. Gerber, and E. Weibel, "Surface Studies by Scanning Tunneling Microscopy," *Am. Phys. Soc.*, vol. 49, no. 1, pp. 51–60, 1982.

[91] Y. Leng, *Materials Characterization: Microscopic and Spectroscopic Methods*. Wiley, 2008, pp. 1–384.

[92] G. H. Keller and M. M. Manak, *DNA Probes*, 2nd ed. Nature Publishing Group, 1993, p. 688.

[93] R. E. Marquis and E. L. Carstensen, "Electric conductivity and internal osmolality of intact bacterial cells.," *J. Bacteriol.*, vol. 113, no. 3, pp. 1198–206, Mar. 1973.

SF298

REPORT DOCUMENTATION PAGE		Form Approved OMB No. 074-0188

The public reporting burden for this collection of information is estimated to average 1 hour per response, including the time for reviewing instructions, searching existing data sources, gathering and maintaining the data needed, and completing and reviewing the collection of information. Send comments regarding this burden estimate or any other aspect of the collection of information, including suggestions for reducing this burden to Department of Defense, Washington Headquarters Services, Directorate for Information Operations and Reports (0704-0188), 1215 Jefferson Davis Highway, Suite 1204, Arlington, VA 22202-4302. Respondents should be aware that notwithstanding any other provision of law, no person shall be subject to an penalty for failing to comply with a collection of information if it does not display a currently valid OMB control number. **PLEASE DO NOT RETURN YOUR FORM TO THE ABOVE ADDRESS.**

1. REPORT DATE (DD-MM-YYYY) 27-03-2014	2. REPORT TYPE Master's Thesis	3. DATES COVERED (From – To) Sep 2012 - Mar 2014
4. TITLE AND SUBTITLE Optimization of Graphene Sensors to Detect Biological Warfare Agents		**5a. CONTRACT NUMBER**
		5b. GRANT NUMBER
		5c. PROGRAM ELEMENT NUMBER
6. AUTHOR(S) - Quinton, Matthew J., Major, USAF		**5d. PROJECT NUMBER** JON 14P239Z
		5e. TASK NUMBER
		5f. WORK UNIT NUMBER
7. PERFORMING ORGANIZATION NAMES(S) AND ADDRESS(S) Air Force Institute of Technology Graduate School of Engineering and Management (AFIT/EN) 2950 Hobson Way WPAFB OH 45433-7765		**8. PERFORMING ORGANIZATION REPORT NUMBER**
9. SPONSORING/MONITORING AGENCY NAME(S) AND ADDRESS(ES) Air Force Office of Scientific Research Attn: Mr. Andrew Kreeger 875 N. Randolph Street Suite 325, Room 3-112 Arlington, VA 22203-1768		**10. SPONSOR/MONITOR'S ACRONYM(S)** AFOSR
		11. SPONSOR/MONITOR'S REPORT NUMBER(S)

12. DISTRIBUTION/AVAILABILITY STATEMENT
DISTRIBUTION STATEMENT A: APPROVED FOR PUBLIC RELEASE; DISTRIBUTION UNLIMITED.

13. SUPPLEMENTARY NOTES
This material is declared a work of the U.S. Government and is not subject to copyright protection in the United States.

14. ABSTRACT
The Defense Threat Reduction Agency and the Air Force Office of Scientific Research want sensors to detect biological agents better, faster, and cheaper. This research explores the use of graphene functionalized with single strand deoxyribonucleic acid (ssDNA) aptamers as a detection method for the Sterne strain of *Bacillus anthracis*. This research is interesting because of the unique electrical and chemical binding properties of graphene and its interaction with ssDNA and DNA. The interactions of graphene functionalized with ssDNA in response to *B. anthracis* spores, non-complimentary and complimentary DNA were explored in static and dynamic aqueous environments with indirect complimentary binding confirmation via Raman spectroscopy and atomic force microscopy. The results suggest aptamer functionalized graphene can be used to detect *B. anthracis* spores, non-complimentary and complimentary DNA sequences.

15. SUBJECT TERMS
Biosensor, Graphene, GFET, ssDNA aptamers, aptamers, Bacillus anthracis

16. SECURITY CLASSIFICATION OF:			17. LIMITATION OF ABSTRACT	18. NUMBER OF PAGES	19a. NAME OF RESPONSIBLE PERSON LTC Douglas Lewis (ENP)
REPORT U	**ABSTRACT** U	**c. THIS PAGE** U	UU	149	**19b. TELEPHONE NUMBER** (Include area code) (937) 255-3636, x4579 douglas.lewis@afit.edu

Standard Form 298 (Rev: 8-98)
Prescribed by ANSI Std. Z39-18